NTNU

Norwegian University of
Science and Technology

Development of a Dynamic Positioning System for Merlin WR200 ROV

Øyvind Løberg Aakre

Master of Science in Cybernetics and Robotics
Submission date: January 2016
Supervisor: Thor Inge Fossen, ITK
Co-supervisor: Martin Ludvigsen, IMT
Ments Tore Møller, IKM Subsea Solutions AS
Roger Eriksen, IKM Subsea Solutions AS

Norwegian University of Science and Technology
Department of Engineering Cybernetics

NTNU
Norwegian University of Science and Technology

Faculty of Information Technology, Mathematics and Electrical Engineering
Department of Engineering Cybernetics

MSC THESIS DESCRIPTION SHEET

Name:	Øyvind Løberg Aakre
Department:	Engineering Cybernetics
Thesis title (Norwegian):	Utvikling av et dynamisk posisjoneringssystem for Merlin WR200 ROV
Thesis title (English):	Development of a Dynamic Positioning System for Merlin WR200 ROV

Thesis Description:

Control of unmanned vehicle-manipulator systems (UVMS) including both ROVs and Autonomous Underwater Vehicles (AUVs) with manipulator arms, require full-DOF control of the vehicle. In particular, it is necessary to be able to keep the vehicle at a constant position and orientation, in order for the manipulator to efficiently perform its task. The vehicles considered in this project are therefore fully actuated ROVs and/or AUVs. Survey AUVs with torpedo shape and no sway actuation are thus not considered.

In particular, the project will consider the Merlin WR200, which is a Class 3 work class-ROV with fully electric propulsion. Today it only has auto functions for altitude, depth and direction. In order to increase the precision and make marine operations close to the sea floor more efficient (depth < 100 meters), it is desirable to equip the vehicle with local dynamic positioning capabilities (station keeping). Local in the sence that there are no available global reference systems, and the station keeping will thus be relative to the sea floor.

This project is part of addressing the main challenge of increasing the level of autonomy and robustness for automatic mapping, monitoring and intervention, high-level planning/re-planning and reconfiguration of single and multiple vehicles subject to the particular mission, environmental condition, available energy, communication constraints, and any failure conditions.

The MSc project is coordinated with ongoing research prrojetcs at the Centre of Autonomous Marine Operations and Systems (AMOS), which offer cutting edge expertise and experimental facilities.

The following subtasks should be addressed:

1. Verify and improve the station-keeping controller developed in Ohrem (2015), by including the tether and thruster dynamics in the control loop. Extend the control objectives to also control the roll and pitch angles and redesign the controller to compensate for tether-induced motions.
2. Extend the line-of-sight (LOS) steering law proposed in Ohrem (2015) to fully actuated vehicles and verify the design by waypoint tracking.
3. Implement a joystick reference model for low-speed maneuvering under automatic control.
4. Implement and verify the developed system using Matlab and the Merlin WR200 simulator at IKM Subsea, Bryne.
5. Implement the control system on exisiting hardware and verify the dynamic positioning functionality through hardware-in-the-loop (HIL) simulations.
6. Based on the results from HIL simulations, perform full-scale experiments to verify the functionality of the proposed controller on Merlin WR200 using the navigation system developed in Knausgård (2013).
7. Conclude your results.

The goal of this project is to have a “ready to implement” algorithm for station keeping based on Ohrem (2015) using the Merlin WR200 simulator. With a functional and robust station keeping controller running on the Merlin WR200 simulator, path following algorithm/control by Ohrem (2015) may be explored.

Starting date:	17.08.2015
Submission date:	21.01.2016
Supervisor:	Professor Thor I. Fossen, Dept. of Eng. Cybernetics, NTNU.
Co-supervisor:	Professor Martin Ludvigsen, Dept. of Marine Technology, NTNU.
	Ments Tore Møller/Roger Eriksen, IKM Subsea Solutions AS.
Thesis performed at:	Department of Engineering Cybernetics, NTNU

To my dear Marie, to my parents Helen and Paul, for always being there for me.

Abstract

Control of Remotely Operated Vehicles (ROV) with manipulator arms, require control of all Degrees of Freedom (DOF) of the vehicle. Merlin WR200 is a work-class ROV currently equipped with automatic depth and heading control, which is the industry standard. It is of interest to equip Merlin WR200 with local Dynamic Positioning (DP) capabilities to allow for more efficient operations close to the sea floor. This includes systems for station keeping, trajectory tracking, path following and low-speed maneuvering. The system is local in the sense that there are no global reference systems, and the position is thus found relative to the sea floor. Robustness is essential to account for uncertain modeling and suppression of disturbances from ocean currents and tether-induced motions.

Previous work on DP for Merlin WR200 lays the foundation for this thesis. The previously proposed control system has been extended for full-DOF control, including compensation of the actuator dynamics and tether disturbances in the control loop. The proposed changes have been documented in a simulation study using the high-fidelity Merlin WR200 simulator at the headquarters of IKM Subsea Solutions AS. Using the simulator, it was possible to develop a controller that was further verified in full-scale experiments. As such, the simulator proved to be a highly valuable tool for verification of control design.

Systems for station keeping, trajectory tracking, path following and low-speed maneuvering was implemented in Matlab and verified using the simulator. The proposed controller was able to meet the control objective in all scenarios considered in this thesis, even when disturbed by ocean current. Successful station keeping was possible with current speed up to 2.5 knots, at which point two thrusters were running at full speed. The modules for low-speed maneuvering and station keeping was implemented on a PLC, and used in successful positioning and stabilization of a Merlin WR200 ROV in a full-scale experiment.

The robustness of the system can be credited to the disturbance observer, which allows for fast and effective integral action by balancing the equations of motion. The extension to compensate for actuator dynamics, although effective, does not pull its weight in terms of the additional implementation complexity. It is suggested to replace the parameter adaptation scheme with the proposed disturbance observer, and consider omitting compensation of actuator dynamics for a simpler implementation.

Sammendrag

Regulering av fjernstyrte undervannsfartøy (ROV) med manipulatorarmer, krever regulering av alle frihetsgradene (DOF) til fartøyet. Merlin WR200 er en arbeidsklasse ROV, utstyrt med automatisk dybde- og retningsregulering, som er standarden i industrien. Det er ønskelig å utstyre Merin WR200 med et lokalt dynamisk posisjoneringssystem (DP) for å effektivisere arbeidsoppgaver nær havbunnen. Dette innebærer systemer for posisjons- og orientasjonsregulering, tidsavhengig og tidsuavhengig banefølging, og manøvrering ved lave hastigheter. Systemet er lokalt i den forstand at det ikke eksisterer et tilgjengelig globalt referansesystem, slik at posisjonen er gitt i forhold til havbunnen i operasjonsområdet. En robust løsning etterstrebes for å ta høyde for modellfeil, og for å motvirke forstyrrelser fra havstrømmer og fra kommunikasjonskabel/tjor.

Denne avhandlingen baserer seg på tidligere arbeid på DP for Merlin WR200. Den allerede foreslåtte regulatoren har blitt utvidet til å gjelde alle frihetsgradene. I tillegg kompenserer den for dynamikken i thrusterne og for forstyrrelser som måtte virke på farkosten. De foreslåtte endringene har blitt verifisert ved bruk av den avanserte Merlin WR200-simulatoren ved hovedkvarteret til IKM Subsea Solutions AS på Bryne. Ved hjelp av simulatoren var det mulig å utvikle et reguleringssystem som ble verifisert i fullskalatester. Til dette formålet har simulatoren vist seg å være et særdeles nyttig verktøy for regulatordesign.

Systemer for posisjonsregulering, tidsavhengig og tidsuavhengig banefølging samt manøvreringssystem, ble implementert i Matlab og verifisert ved hjelp av simulatoren. Den foreslåtte regulatoren bestod alle tester som denne oppgaven tar for seg, selv med havstrøm. Det var mulig å stabilisere posisjon og orientasjon med opptil 2.5 knop strøm, hvorpå to av de horisontale thrusterne kjørte på maksimalt turtall. En vellykket fullskala sjøtest ble gjennomført med modulene for manøvrering og posisjonsregulering implementert på en PLS. Systemene ble brukt til å posisjonere og stabilisere ROVen på en hensiktsmessig måte.

Den robuste oppførselen som systemet utviser, tillegges avviksestimatoren, som sørger for rask og effektiv integralvirkning ved å balansere bevegelsesligningene. Den foreslåtte løsningen for kompensasjon av thrusterdynamikk, yter ikke i en slik grad at den rettferdiggjør den ekstra implementasjonskostnaden. Det foreslås å erstatte parameteradapsjon med avviksestimatoren, og å vurdere om man skal utelate kompensasjon av thrusterdynamikk for å få en enklere implementasjon.

Preface

This thesis is written as a compulsory part of the Master's degree in Engineering Cybernetics at the Department of Engineering Cybernetics at the Norwegian University of Science and Technology (NTNU). The project was carried out from August 2015 to January 2016 in collaboration with IKM Subsea Solutions AS.

Acknowledgements

I would like to thank IKM Subsea Solutions AS for this unique opportunity and for welcoming me at their offices. A special thanks goes to Roger Eriksen for fruitful discussions and guidance, Ments Tore Møller for your enthusiasm and for arranging everything, Vidar Eriksen for technical support, Peder Holm Østmoe for help with CAD drawings, and Erlend Apeland for daring to test the newly developed system in the field. I would also like to thank Martin Ludvigsen and Thor Inge Fossen, for guidance and support from NTNU.

A sincere thanks goes to my parents Helen and Paul, for their support throughout this project. I'm forever grateful to Marie, for her endless support and for enduring this time apart.

Øyvind Løberg Aakre,
Stavanger, January 2016

Contents

List of Figures

List of Tables

List of Acronyms

CG Center of Gravity

CO Center of Origin

CURV Cable-Controlled Underwater Recovery Vehicles

DOF Degrees of Freedom

DP Dynamic Positioning

DVL Doppler Velocity Log

EKF Extended Kalman Filter

FOG Fibre Optic Gyro

GNSS Global Navigation Satellite System

HIL Hardware-in-the-loop

IAE Integrated Absolute value of Error

IMU Inertial Measurement Unit

LOS Line-of-sight

MADU Mean of absolute value of rate of change of the input

MIMO Multiple Input Multiple Output

MMADU Mean of MADU

NCS New Control System

NED North, East, Down

PCABS Parameter and Current Backstepping Controller

RMS Root Mean Square

ROV Remotely Operated Vehicle

TMS Tether Management System

Notation

$\boldsymbol{\eta}$	Position and attitude vector
$\boldsymbol{\nu}$	Velocity vector
$\mathbf{v}$	Linear velocity vector
$\boldsymbol{\omega}$	Angular velocity vector
$\mathbf{M}$	Mass matrix
$\mathbf{C}(\boldsymbol{\nu})$	Coriolis and centripetal matrix
$\mathbf{D}(\boldsymbol{\nu})$	Damping matrix
$\mathbf{g}(\boldsymbol{\eta})$	Restoring forces matrix
$\boldsymbol{\tau}$	Vector of generalized forces
$\mathbf{B}$	Thrust configuration matrix
$\mathbf{u}$	Vector of thruster inputs
$\mathbf{T}$	Matrix of thruster time constants
θ	Pitch angle
$\boldsymbol{\theta}$	Parameter vector (**bold**)
$\boldsymbol{\Theta}$	Attitude vector
ϕ	Roll angle
$\boldsymbol{\phi}$	Regressor matrix (**bold**)
$\boldsymbol{\Gamma}$	Adaptation gain matrix
$\mathbf{K}_1$	Gain matrix penalizing position errors
$\mathbf{K}_2$	Gain matrix penalizing virtual velocity errors
K_3	Scalar gain penalizing virtual input errors

Accent	Usage	Description
Tilde	$\tilde{\boldsymbol{\eta}} = \boldsymbol{\eta} - \boldsymbol{\eta}_d$	Error between measured and desired value
Hat	$\hat{\mathbf{M}}$	Estimated mass matrix
Dot	$\dot{\boldsymbol{\nu}}$	Time derivative of the variable

Chapter 1

Introduction

Merlin WR200 is a Class 3 work-class Remotely Operated Vehicle (ROV) with fully electric propulsion, developed by IKM Subsea Solutions AS in Bryne, Norway. Today, the ROV only feature automatic systems for controlling depth and heading, which is the industry standard (Christ and Wernli 2014). To make subsea operations more efficient, it is desirable with a Dynamic Positioning (DP) system that automatically maintains the position and orientation of the ROV. Such a system would simplify working with the manipulators and conducting inspections close to the sea floor, by relieving pilots of positioning the ROV manually. Development of a dynamic positioning system for Merlin WR200 started with Knausgård (2012) and Knausgård (2013) and was continued by Ohrem (2015). To present day, none of the developed systems have been fully integrated with the existing systems of Merlin WR200. Thus, the motivation for this thesis is to build upon the results of Knausgård (2013) and Ohrem (2015) and provide a robust, proven system, verified at sea trials and ready for integration with the ROV fleet of IKM.

1.1 What is a ROV?

A ROV is a tethered underwater robot being operated by a pilot which is typically situated in a control room on board a ship (Fig. 1.1). An umbilical cable connects the ROV to the host ship, providing power and control signals. Class 3 work class-ROVs are typically equipped with manipulator arms and cameras, enabling the pilots to do work underwater. In the case of Merlin WR200, a separate assembly

called tophat Tether Management System (TMS) sits on top of the ROV as a garage-like device when deploying and retrieving the ROV. It is connected to the ship with an armored umbilical cable, and to the ROV with a neutrally buoyant tether. When underwater, the TMS act as a clump weight, minimizing drift due to current (Poissonnet 2013). The purpose of the TMS is to allow the pilot to lengthen and shorten the tether to minimize cable drag as the ROV moves through the ocean space.

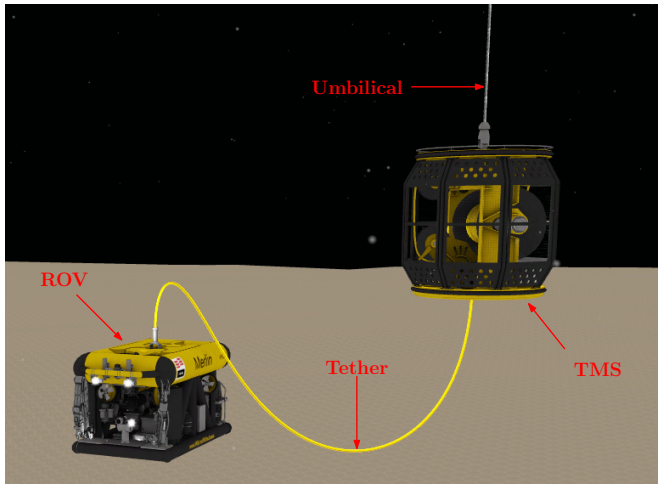

Figure 1.1: Merlin WR200 is shown together with the TMS. Merlin is connected to the TMS by the tether. An armored umbilical cable connects TMS to the ship.

The Marine Technology Society (2015) credits the first tethered, underwater vehicle to Dimitri Rebikoff. In 1953, Rebikoff invented the POODLE based on surplus parts from German V1 and V2 missiles from the second world war (Rebikoff 1985). In the 1960s, the underwater vehicle technology was advanced by the US Navy into what was called Cable-Controlled Underwater Recovery Vehicles (CURV). They were used to recover bombs from the ocean floor, most notably nuclear bombs lost in the Mediterranean Sea after the 1966 Palomares B-52 crash (Marine Technology Society 2015; Hadden 2012). The oil and gas industry further developed the technology in the 1980s to assist in developing offshore oil fields, exceeding the reach of human divers. Today, ROVs appear in academic and commercial applications world wide.

1.2 Problem description

The following subtasks should be addressed:

1. Verify and improve the station-keeping controller developed in Ohrem (2015), by including the tether and thruster dynamics in the control loop. Extend the control objectives to also control the roll and pitch angles and redesign the controller to compensate for tether-induced motions.
2. Extend the line-of-sight (LOS) steering law proposed in Ohrem (2015) to fully actuated vehicles and verify the design by waypoint tracking.
3. Implement a joystick reference model for low-speed maneuvering under automatic control.
4. Implement and verify the developed system using Matlab and the Merlin WR200 simulator at IKM Subsea Solutions AS, Bryne.
5. Implement the control system on exisiting hardware and verify the dynamic positioning functionality through hardware-in-the-loop (HIL) simulations.
6. Based on the results from HIL simulations, perform full-scale experiments to verify the functionality of the proposed controller on Merlin WR200 using the navigation system developed in Knausgård (2013).
7. Conclude your results.

The goal of this project is to present a "ready to implement" algorithm for station keeping, based on Ohrem (2015) and using the Merlin WR200 simulator. With a functional and robust station keeping controller running on the simulator, path following may be explored.

1.3 Contributions

This thesis makes the following contributions

- The control objective is extended to 6 Degrees of Freedom (DOF) including compensation of actuator dynamics.
- A disturbance observer is formulated for robust disturbance rejection.
- A simplified joystick velocity reference model with state machine is implemented for low-speed maneuvering.

- The developed system is verified using a high-fidelity simulator and in full-scale experiments.

1.4 Thesis outline

A literature survey covering relevant guidance and control topics is given in Chapter 2. Chapter 3 provides the necessary background material, including notation, reference frames and mathematical modeling of Merlin WR200. The developed control system is treated in Chapter 4. Guidance, including joystick reference model and waypoint tracking is found in Chapter 5. The simulator and simulation setup along with some implementation details are given Chapter 6. Simulations and sea trials, including results and discussion, are treated in Chapters 7 and 8. Finally, a conclusion and further recommendations are found in Chapter 9.

Chapter 2

Literature Survey

2.1 Motivation

In the development of a dynamic positioning system for the Merlin WR200 ROV, several challenges has to be overcome. In particular, the problem is to design a control system that can cope with uncertain modeling of the vehicle, time-varying disturbances and significant actuator dynamics. The problem can be further extended to include a guidance system being able to create reference trajectories for A to B moves, and path following. The following sections aim to review how said challenges are met in systems similar to Merlin WR200.

2.2 Vectorial backstepping and Actuator dynamics

Integrator backstepping is a recursive method for simultaneous control design and stability analysis. The idea is to recursively construct a (control) Lyapunov function and step back through the integrators of the system until one has reached the input. A virtual control is assigned at each step to stabilize a state variable. This allows for flexible control design where one can exploit good characteristics of the system, for instance dissipative damping, yielding a more robust control system (Thor I. Fossen 2011). T. Fossen and Berge (1997) introduced the concept of vectorial backstepping alongside a methodology for designing model based controllers for Multiple Input Multiple Output (MIMO) systems. In this framework, actuator dynamics can be included in a systematic manner by means of an additional "step back" through the integrators of the propulsion system. Zhu and Gu

(2011), Patompak and Nilkhamhang (2012), and Srisamosorn, Patompak, and Nilkhamhang (2013), formulate control laws for ROVs using vectorial backstepping. However, actuator dynamics are not considered, even though Patompak and Nilkhamhang (2012) report that the thrusters cannot produce the output fast enough for proper control.

2.3 Uncertain model and time-varying disturbances

Underwater vehicles are subject to hydrodynamic and hydrostatic forces and moments of complex nature. It is possible to perform experimental tests such as drag tests, or computational fluid dynamics analysis, that can reveal some of the dynamic properties of the system. However, as the system is nonlinear, these properties will depend on the load condition, and in the case of industrial ROVs, also equipped tools and skids. This means that an accurate model is not always trivial to obtain. In addition to modeling uncertainties, underwater vehicles are subject to disturbances from ocean currents and the tether. From a control point of view, there are tools to cope with these issues, such as adaptive control, which has been successfully applied in numerous publications.

2.3.1 Adaptive control

The objective of adaptive control is to structure the system equations into known and unknown parts. The known part is often referred to as the regressor with symbol $\boldsymbol{\phi}(\cdot)$, being a matrix of known signals. Unknown parameters are typically collected in a vector $\hat{\boldsymbol{\theta}}$, which is updated by a differential equation often referred to as the parameter update law. If adaptive systems are not persistently excited, which can be described as an input signal of sufficiently rich content, one cannot guarantee that the parameters will converge to their true values. In most cases the control objective can still be achieved despite non-converging parameters (Ioannou and Sun 2012). Also note that in this thesis the true parameters are, in view of control, not of interest.

Antonelli et al. (2003) consider an underwater vehicle subject to ocean currents that are assumed to be constant and irrotational in the Earth-fixed reference frame. This assumption is exploited in the adaptive control law by projecting the current disturbance to the vehicle frame. In other words, the integral action of the adaptive controller is rotated with the vehicle, yielding better performance than controllers considering the disturbances in the body-fixed frame alone (Antonelli et al. 2003). The proposed system considers only the restoring force in heave and

horizontal current in the adaptive law. Thus, the other model parameters such as mass, inertia and damping coefficients, are not adapted.

An underwater vehicle with uncertain parameters is also considered by Zhu and Gu (2011). The authors assume bounded disturbances and constant or slowly varying parameters. This is justified by assuming that the craft is operating in deep seas. A control law is formulated using vectorial backstepping, where the parameters of the craft are adapted. Disturbances are rejected using a discontinuous, high-frequency switching term, known from sliding-mode controllers. The disturbances are lumped into one term and expressed in the vehicle frame, in contrast to Antonelli et al. (2003) in which disturbances were assumed to be constant in the inertial frame. Perfect control cannot be achieved for this system due to the slow dynamic response of the thrusters. However, the tracking error can be controlled within an acceptable range by modifying the switching term (Zhu and Gu 2011). The control law is formulated in 4 DOF, but proportional control is applied to roll and pitch, yielding undesirable oscillatory behavior.

Patompak and Nilkhamhang (2012) extend the ideas of Zhu and Gu (2011) by also assuming bounded disturbances. A modification is proposed where an adaptive law is formulated for the sliding-mode gain to lift the requirement of prior knowledge of the upper bound of the disturbances. However, the proposed solution introduce parameter drift. Srisamosorn, Patompak, and Nilkhamhang (2013) propose a modification to the adaptation law by means of a new switching method. Both controllers perform well in numerical simulations. Roll and pitch are left uncontrolled by assuming a large enough distance to the center of buoyancy, such that these states are assumed to be naturally stable.

In total, the control laws proposed above adhere to the same ideas of using adaptation and/or backstepping. However, full-DOF control is not considered.

2.3.2 Disturbance Observer

An alternative approach to disturbance rejection is to use an observer, which appear in various forms in the literature. For example, by using strain gauge-measurements mounted on the ROV to measure disturbing forces (Selvakumar and Asokan 2015), and modelling the disturbances as nonlinear, marginally stable wave-like systems (Mukherjee, Kar, and Bhatt 2015).

More progress have been made in the field of robotics. Recent research includes Sariyildiz and Ohnishi (2015), where the authors provide an in-depth analysis of the stability and robustness of a disturbance observer in a motion control system. The theorems and theoretical results are demonstrated on an experimental small-

scale, planar, two-link robot with excellent results. However, design and analysis is undertaken using linear theory and frequency-domain techniques, which may not be adequate to capture the nonlinearities in underwater robotic systems.

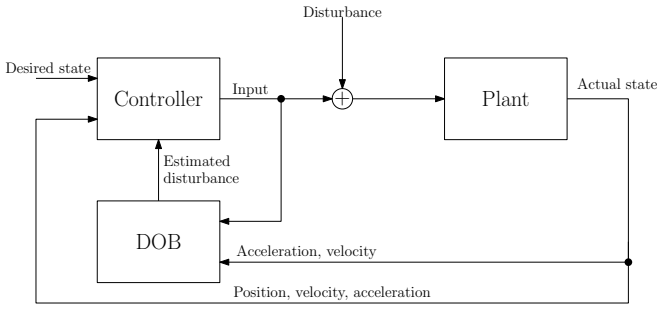

Figure 2.1: Disturbance observer in feedback control as in Chen et al. (2000)

A more general approach is presented in Chen et al. (2000), where external forces, moments and unmodelled dynamics, are collected into one term for each degree of freedom. The basic principle is to estimate the disturbances from Newton's second law:

$$\Sigma F = f_{input} + f_{dyn} + f_{ext} = ma \tag{2.1}$$

$$\Downarrow \tag{2.2}$$

$$f_{ext} = ma - f_{dyn} - f_{input} \tag{2.3}$$

in which f_{ext} is an external force, m and a are mass and acceleration, f_{input} is the input force, and f_{dyn} describes a known force, e.g. friction. Based on this principle, a nonlinear disturbance observer was developed, overcoming the limitations of linear techniques at that time (Mohammadi et al. 2013). A general approach for the observer design was given, but the authors could only determine the observer gain matrix for a two-link robotic manipulator.

Mohammadi et al. (2013) build upon the results from Chen et al. (2000) and provide a method to determine the observer gain matrix for any n-DOF serial robotic manipulator - with equations of motion similar to marine crafts. Both numerical simulations and practical experiments indicate excellent results. The technique proposed by Chen et al. (2000) does not require a priori information about the disturbances to reject them, but for perfect *estimation*, some information is needed about the system dynamics. This typically involves the dissipative terms or restoring forces and moments. However, exact knowledge about the dynamics is not needed in view of control (Mohammadi et al. 2013). The disturbance estimation error can be shown to be exponentially convergent if the

disturbances are constant, and globally uniformly ultimately bounded if the rate of change of the disturbances are bounded (Mohammadi et al. 2013).

The concepts developed in Chen et al. (2000) and Mohammadi et al. (2013), are applied in Wei et al. (2015) for heading control of a ROV. The authors assume the observer cannot perfectly cancel the disturbances, and use adaptation to remove remaining residuals. This method is verified in numerical simulations showing excellent results.

2.3.3 Tether cable modelling

The literature presents many ways for modelling tether cables. Catenary equations are frequently used in mooring analysis (Asgeir J Sørensen 2013), which considers the tangential and normal forces of infinitely small elements. These can be described by ordinary differential equations to be applied in simulations or in the system model. Similarly, Prabhakar and B. Buckham (2005) apply Newton's laws on a variable mass system in order to obtain an accurate, spatially-discrete model suited for high-fidelity simulations. Other methods include modelling the impact of the cable as a disturbance, e.g. as quadratic drag (Thor Inge Fossen 1991) or as a linear spring (Svendby 2007).

2.4 Guidance

Guidance can be considered as the means of finding a direction of travel that will take a vehicle towards a target. In path following settings, the Line-of-sight (LOS) guidance principle (T. Fossen, M Breivik, and Skjetne 2003; Morten Breivik and Thor I. Fossen 2005; Thor I. Fossen 2011) is often applied to underactuated vehicles having no control in sway. Such vehicles are considered by Børhaug, Pavlov, and Pettersen (2008) and Caharija et al. (2012), where the LOS steering law include integral action to cope with ocean currents. The objective of traditional LOS guidance is to align the vehicle along the straight-line path between a reference point and a target, by means of directing the heading angle towards a line-of-sight point $(x_{los},\ y_{los})$ (Figure 2.2). Dukan (2014) applies the LOS guidance principles to the velocity vector of a fully actuated ROV, leaving heading to be controlled independently of direction of travel. This allows for several operating modes and full flexibility.

For trajectory tracking, Thor I. Fossen (2011) suggest using filter-based reference models with dynamics similar to the vehicle. Common issues with this approach

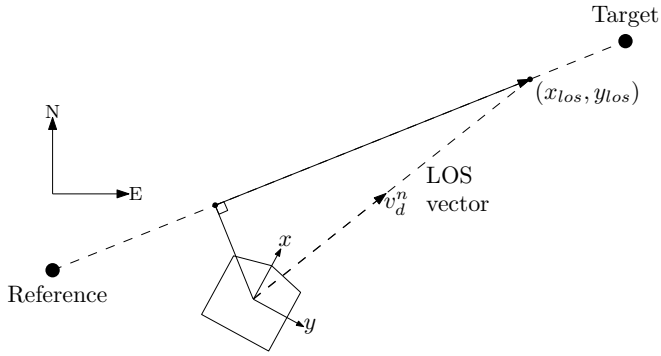

Figure 2.2: LOS guidance principle applied to a fully actuated vehicle. The vehicle should be aligned with the straight line in between the reference and the target. In this case the velocity vector is directed toward the the line of sight intersection point $(x_{los},\ y_{los})$.

is the need to introduce saturating elements and gain scheduling to ensure trajectories within the capabilities of the vehicle (Thor I. Fossen 2011). Dukan (2014) suggest a constant jerk reference model for A to B moves. The proposed model is valid for any distance and constrained by maximum cruise speed, acceleration and jerk, all of which can be provided by an operator. The principle is to switch a constant jerk on and off in continuous time. Thus, desired trajectories for acceleration, velocity and position are found through integration. Dukan (2014) suggest to use the analytical solution to the integrals to avoid numerical round-off errors. In general, the time instances for switching the jerk will not coincide with the sampling period of the system. As such, the implementation complexity exceeds that of filter-based reference models.

2.5 Previous work on Merlin WR200

Work on dynamic positioning for Merlin WR200 started with Knausgård (2013). The work included a navigation system based on an Extended Kalman Filter (EKF) which estimates a local position. The controller and navigation system was implemented alongside the existing control system and verified at sea trials, showing good results. A method for maneuvering the ROV using direct force control was received well by the pilots, whereas using the joystick in a velocity control setting, proved more difficult. However, IKM Subsea Solutions reported issues regarding repeatability and inconsistency in performance of the station

keeping system. Whether the navigation system or the controller was at fault, was not clear. For the continuation of the project, IKM desired a controller that could be made independent of the system parameters, which was undertaken by Ohrem (2015). Robustness is ensured using adaptive control inspired by Antonelli et al. (2003) and Patompak and Nilkhamhang (2012), which is also designed to compensate for ocean currents. The developed dynamic positioning system included path-following, enabling the ROV to follow paths based on the already driven route, or paths defined in advance. Where Knausgård (2013) worked close to hardware and the physical ROV, Ohrem (2015) worked mainly with a Simulink simulation model. Some tests were performed on the high-fidelity simulator recently acquired by IKM to train ROV pilots. The developed control law showed promising results in these simulations, and hence forms the basis for this thesis.

Chapter 3

Theoretical Background

The mathematical modeling of Merlin WR200 is given in this chapter, including reference frames, equations of motion and an improved thrust model.

3.1 Frames of reference

This thesis will consider two frames of reference; a North, East, Down (NED) or $\{n\}$ coordinate system, and a body-fixed coordinate system $\{b\} = (x_b, y_b, z_b)$ attached to the ROV. The NED-frame defines a plane tangential to Earth's surface where the x-axis points toward true North, y-axis toward East and the z-axis points down toward Earth's center (Fig. 3.1). The NED-frame is a moving frame, but for a vehicle operating in a local area at approximately constant longitude and latitude, the frame can be assumed inertial and hence Newton's laws still apply (Thor I. Fossen 2011). The body-fixed frame has its origin in the ROV's Center of Origin (CO) with axes coinciding with the principle axes of inertia. The axes x_b, y_b and z_b are defined positive forward, starboard and downward seen from the CO of the ROV, as shown in Figure 3.2.

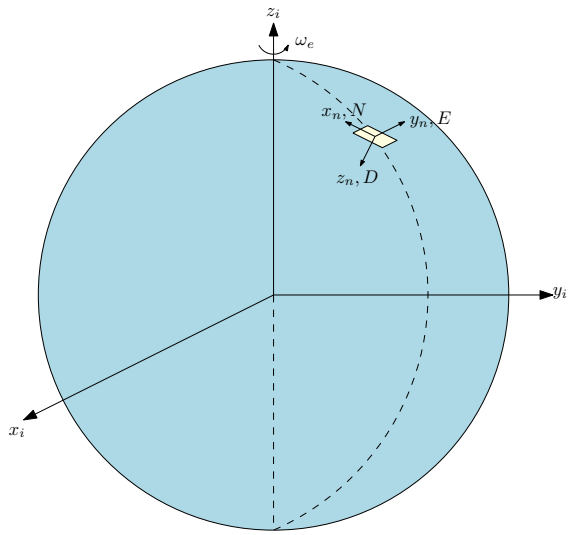

Figure 3.1: The Earth centered inertial frame $\{i\}$ shown together with the NED $\{n\}$ frame. Note that the NED frame is tangential to the surface.

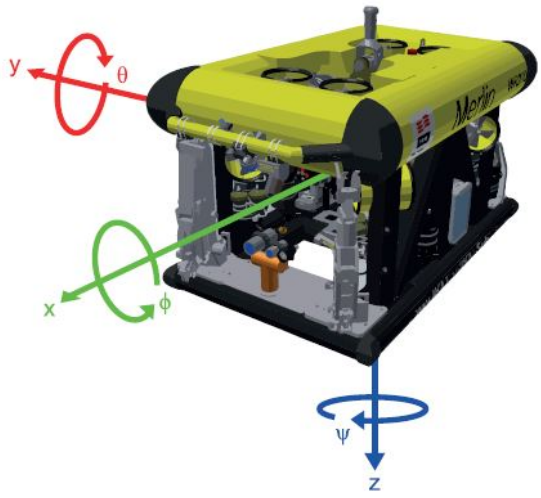

Figure 3.2: Body fixed coordinate system with Euler angles roll, pitch and yaw (ϕ, θ, ψ). Image courtesy of Knausgård (2013).

3.2 Notation

Merlin WR200 is an underwater vehicle operating in 6 Degrees of Freedom (DOF). The naming convention for describing the axis system follow from The Society of Naval Architects and Marine Engineers (1950) (Table 3.1).

Table 3.1: SNAME naming convention for a body operating in 6 degrees of freedom.

no.	DOF	Position & attitude	Linear & angular velocity	Forces & moments
1	motions in the x direction (surge)	x	u	X
2	motions in the y direction (sway)	y	v	Y
3	motions in the z direction (heave)	z	w	Z
4	rotation about the x axis (roll)	ϕ	p	K
5	rotation about the y axis (pitch)	θ	q	M
6	rotation about the z axis (yaw)	ψ	r	N

Adopting the notion of Thor I. Fossen (2011), the generalized position, velocity and force vectors are

$$\boldsymbol{\eta} = \begin{bmatrix} \mathbf{p}^n_{b/n} \\ \boldsymbol{\Theta}_{nb} \end{bmatrix}, \quad \boldsymbol{\nu} = \begin{bmatrix} \mathbf{v}^b_{b/n} \\ \boldsymbol{\omega}^b_{b/n} \end{bmatrix}, \quad \boldsymbol{\tau} = \begin{bmatrix} \mathbf{f}^b_b \\ \mathbf{m}^b_b \end{bmatrix}$$

where

$$\mathbf{p}^n_{b/n} = (N, E, D)^\top \in \mathbb{R}^3 \qquad \boldsymbol{\Theta}_{nb} = (\phi, \theta, \psi)^\top \in \mathbb{R}^3$$
$$\mathbf{v}^b_{b/n} = (u, v, w)^\top \in \mathbb{R}^3 \qquad \boldsymbol{\omega}^b_{b/n} = (p, q, r) \in \mathbb{R}^3$$
$$\mathbf{f}^b_b = (X, Y, Z)^\top \in \mathbb{R}^3 \qquad \mathbf{m}^b_b = (K, M, N)^\top \in \mathbb{R}^3$$

A superscript denotes the coordinate frame where a vector is expressed, and the subscript provide additional information. The sub- and superscript are in the case of the velocity vector $\boldsymbol{\nu}^p_{b/n}$ read as *The velocity of* $\{b\}$ *with respect to* $\{n\}$ *expressed in frame* $\{p\}$.

Ambiguity of symbols

In this thesis, the symbols used for roll ϕ and pitch θ, are also used in the context of adaptive control describing the regressor matrix $\boldsymbol{\phi}$ and parameter vector $\boldsymbol{\theta}$. Note that the latter are written in **bold** throughout this thesis.

3.2.1 Kinematics

Kinematics captures the geometry of motion and describes how a point moves relative to other points. The body-frame is a moving frame, and is related to the assumed inertial NED-frame using the transformation matrices $\boldsymbol{R}_b^n(\boldsymbol{\Theta}_{nb})$ and $\boldsymbol{T}_{\boldsymbol{\Theta}}(\boldsymbol{\Theta}_{nb})$ for transforming linear and angular velocities, respectively. Thus, the kinematics are given by

$$\begin{bmatrix} \dot{\boldsymbol{p}}_{b/n}^n \\ \dot{\boldsymbol{\Theta}}_{nb} \end{bmatrix} = \begin{bmatrix} \boldsymbol{R}_b^n(\boldsymbol{\Theta}_{nb}) & \mathbf{0}_{3x3} \\ \mathbf{0}_{3x3} & \boldsymbol{T}_{\boldsymbol{\Theta}}(\boldsymbol{\Theta}_{nb}) \end{bmatrix} \begin{bmatrix} \boldsymbol{v}_{b/n}^b \\ \boldsymbol{\omega}_{b/n}^b \end{bmatrix} \tag{3.1}$$

$$\Updownarrow \tag{3.2}$$

$$\dot{\boldsymbol{\eta}} = \mathbf{J}(\boldsymbol{\Theta}_{nb})\boldsymbol{\nu} \tag{3.3}$$

where

$$\boldsymbol{R}_b^n(\boldsymbol{\Theta}_{nb}) = \boldsymbol{R}_{z,\psi}\boldsymbol{R}_{y,\theta}\boldsymbol{R}_{x,\phi} \tag{3.4}$$

$$= \begin{bmatrix} \mathrm{c}\psi\mathrm{c}\theta & -\mathrm{s}\psi\mathrm{c}\phi + \mathrm{c}\psi\mathrm{s}\theta\mathrm{s}\phi & \mathrm{s}\psi\mathrm{s}\phi + \mathrm{c}\psi\mathrm{c}\phi\mathrm{s}\theta \\ \mathrm{s}\psi\mathrm{c}\theta & \mathrm{c}\psi\mathrm{c}\phi + \mathrm{s}\phi\mathrm{s}\theta\mathrm{s}\psi & -\mathrm{c}\psi\mathrm{s}\phi + \mathrm{s}\theta\mathrm{s}\psi\mathrm{c}\phi \\ -\mathrm{s}\theta & \mathrm{c}\theta\mathrm{s}\phi & \mathrm{c}\theta\mathrm{c}\phi \end{bmatrix} \tag{3.5}$$

and

$$\boldsymbol{R}_{x,\phi} = \begin{bmatrix} 1 & 0 & 0 \\ 0 & \mathrm{c}\phi & -\mathrm{s}\phi \\ 0 & \mathrm{s}\phi & \mathrm{c}\phi \end{bmatrix} \quad \boldsymbol{R}_{y,\theta} = \begin{bmatrix} \mathrm{c}\theta & 0 & \mathrm{s}\theta \\ 0 & 1 & 0 \\ -\mathrm{s}\theta & 0 & \mathrm{c}\theta \end{bmatrix} \quad \boldsymbol{R}_{z,\psi} = \begin{bmatrix} \mathrm{c}\psi & -\mathrm{s}\psi & 0 \\ \mathrm{s}\psi & \mathrm{c}\psi & 0 \\ 0 & 0 & 1 \end{bmatrix} \tag{3.6}$$

The rotation matrices in Equation (3.6) belong to the *Special Orthogonal group or order 3 SO(3)* and have the properties $\mathbf{R}^\top\mathbf{R} = \mathbf{R}\mathbf{R}^\top = \mathbf{I}$, where $\mathbf{I}$ is the identity matrix, and $\mathbf{R}^{-1} = \mathbf{R}^\top$ (Egeland and Gravdahl 2002).

The angular velocity transformation matrix is

$$\boldsymbol{T}_{\boldsymbol{\Theta}}(\boldsymbol{\Theta}_{nb}) = \begin{bmatrix} 1 & \mathrm{s}\phi\mathrm{t}\theta & \mathrm{c}\phi\mathrm{t}\theta \\ 0 & \mathrm{c}\phi & -\mathrm{s}\phi \\ 0 & \mathrm{s}\phi/\mathrm{c}\theta & \mathrm{c}\phi/\mathrm{c}\theta \end{bmatrix} \tag{3.7}$$

and has a singularity at $\theta = 90$ degrees, but should not be a problem for Merlin WR200 as the pitch angle is limited to ± 20 degrees.

3.2.2 Vessel Parallel Coordinate System

A Vessel Parallel Coordinate System $\{VP\}$ or $\{p\}$ is used in the derivation of the controller. It is a simplified form of Equation (3.1) where roll and pitch angles are assumed to be close to zero (Thor I. Fossen 2011) (Equation (3.8)).

$$\begin{bmatrix} \dot{\boldsymbol{p}}^n_{b/n} \\ \dot{\boldsymbol{\Theta}}_{nb} \end{bmatrix} = \begin{bmatrix} \boldsymbol{R}_z(\psi) & \mathbf{0}_{3x3} \\ \mathbf{0}_{3x3} & \boldsymbol{I}_{3x3} \end{bmatrix} \begin{bmatrix} \boldsymbol{v}^b_{b/n} \\ \boldsymbol{\omega}^b_{b/n} \end{bmatrix} \tag{3.8}$$

$$\Updownarrow$$

$$\dot{\boldsymbol{\eta}} = \mathbf{P}(\psi)\boldsymbol{\nu} \tag{3.9}$$

The position of the ROV in $\{p\}$ is given by

$$\boldsymbol{\eta}_p = \mathbf{P}^\top(\psi)\boldsymbol{\eta} \tag{3.10}$$

The following result will be useful in the derivation of the control system. Taking the time derivative of (3.10) gives

$$\dot{\boldsymbol{\eta}}_{\boldsymbol{p}} = \dot{\mathbf{P}}^\top(\psi)\boldsymbol{\eta} + \mathbf{P}^\top(\psi)\dot{\boldsymbol{\eta}} \tag{3.11}$$

$$= r\mathbf{S}^\top\mathbf{P}^\top(\psi)\boldsymbol{\eta} + \mathbf{P}^\top(\psi)\mathbf{P}(\psi)\boldsymbol{\nu} \tag{3.12}$$

$$= r\mathbf{S}^\top\boldsymbol{\eta}_p + \boldsymbol{\nu} \tag{3.13}$$

where $r = \dot{\psi}$ is the yaw rate and

$$\mathbf{S} = \begin{bmatrix} 0 & -1 & 0 & 0 & 0 & 0 \\ 1 & 0 & 0 & 0 & 0 & 0 \\ 0 & 0 & 0 & 0 & 0 & 0 \\ 0 & 0 & 0 & 0 & 0 & 0 \\ 0 & 0 & 0 & 0 & 0 & 0 \\ 0 & 0 & 0 & 0 & 0 & 0 \end{bmatrix} \tag{3.14}$$

is a skew-symmetric matrix with property $\mathbf{x}^\top\mathbf{S}\mathbf{x} = 0 \quad \forall\mathbf{x} \geq 0$. The skew-symmetry of $\mathbf{S}$ in Equation (3.13) will be exploited in the control design.

3.3 Guidance, navigation and control for Merlin WR200

A typical guidance, navigation and control system is shown in Figure 3.3. The components and their relevance to this thesis is explained below.

Guidance includes the modules that continuously compute the desired position, velocity and acceleration of the vehicle and are used in the motion control system. These modules include setpoint regulation, trajectory tracking

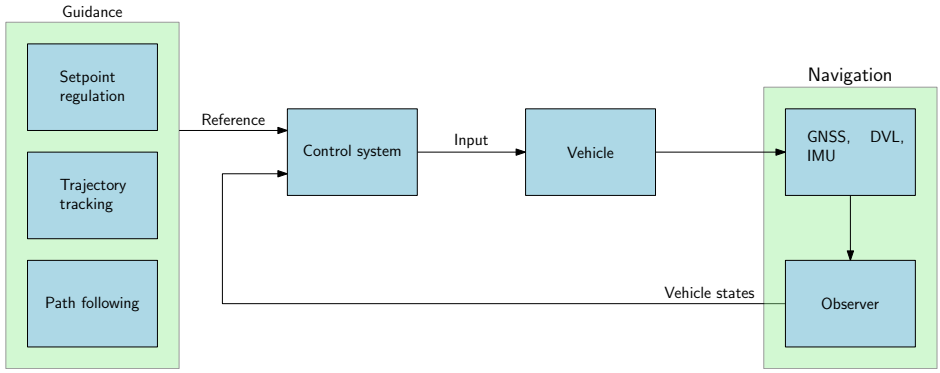

Figure 3.3: A typical guidance, navigation and control system

and path following. Reference models are used to compute feasible time-varying trajectories based on setpoints. They may also take inputs from a joystick and compute trajectories based on how far the stick is pushed in a given direction. Path following concerns tracking of a predefined path independent of time, such as tracking waypoints. Guidance is treated in Chapter 5.

Navigation systems are used to determine the position and velocity of the vehicle. Surface vessels typically use Global Navigation Satellite System (GNSS) to determine its position, while underwater vehicles may use a hydro-acoustic positioning system. Velocity, acceleration and attitude are typically measured with a Doppler Velocity Log (DVL), gyroscopes and accelerometers. Raw measurement signals are processed in order to check for validity and consistency, and filtered by observers such as an EKF. The observer must continue estimation even if sensors fail to provide measurements. This is commonly referred to as *dead reckoning*. The navigation system of Merlin WR200 does not include position measurements, but use measurements of velocity and attitude together with an EKF developed in Knausgård (2013) to determine a local position.

Control systems computes an input based on the error between the desired state and the actual state. In the context of guidance, navigation and control, the desired state is taken from the guidance system and the actual state from the navigation system. The controller developed in Knausgård (2013) was based on exact feedback linearization, which require good knowledge of the vehicle model. The approach taken in Ohrem (2015) and also in this thesis, is vectorial backstepping, which allow for more robust and flexible

control design.

3.4 Equations of motion

This section will present two dynamic models of the Merlin WR200. The first is a high-fidelity model that aims to describe the dynamics as accurately as possible, while the second model simplifies the dynamics resulting in a model more suited for control design.

3.4.1 Process plant model

Using the vectorial notation of Thor I. Fossen (2011) a process plant model can be given as

$$\dot{\boldsymbol{\eta}} = \boldsymbol{J}_{\boldsymbol{\Theta}}(\boldsymbol{\eta})\boldsymbol{\nu} \tag{3.15}$$

$$\boldsymbol{M}_{\mathrm{RB}}\dot{\boldsymbol{\nu}} + \boldsymbol{C}_{\mathrm{RB}}(\boldsymbol{\nu})\boldsymbol{\nu} + \boldsymbol{M}_{\mathrm{A}}\dot{\boldsymbol{\nu}}_{\boldsymbol{r}} + \boldsymbol{C}_{\mathrm{A}}(\boldsymbol{\nu}_{\boldsymbol{r}})\boldsymbol{\nu}_{\boldsymbol{r}} + \boldsymbol{D}(\boldsymbol{\nu}_{\boldsymbol{r}})\boldsymbol{\nu}_{\boldsymbol{r}} + \boldsymbol{g}(\boldsymbol{\eta}) = \boldsymbol{B}\boldsymbol{u} + \boldsymbol{\tau}_{\mathrm{env}} \tag{3.16}$$

$$\boldsymbol{T}\dot{\boldsymbol{u}} = -\boldsymbol{u} + \boldsymbol{u}_c \tag{3.17}$$

in which $\boldsymbol{M}_{\mathrm{RB}} \in \mathbb{R}^{6\times6}$ is the rigid-body inertia matrix and $\boldsymbol{C}_{\mathrm{RB}}(\boldsymbol{\nu}) \in \mathbb{R}^{6\times6}$ is the rigid-body Coriolis and centripetal matrix. $\boldsymbol{M}_{\mathrm{A}} \in \mathbb{R}^{6\times6}$ is the added mass matrix, $\boldsymbol{C}_{\mathrm{A}}(\boldsymbol{\nu}_{\boldsymbol{r}}) \in \mathbb{R}^{6\times6}$ is the added mass Coriolis and centripetal matrix, $\boldsymbol{D}(\boldsymbol{\nu}_{\boldsymbol{r}}) \in \mathbb{R}^{6\times6}$ is the damping matrix and $\boldsymbol{g}(\boldsymbol{\eta}) \in \mathbb{R}^{6\times1}$ is the restoring forces matrix. $\boldsymbol{B} \in \mathbb{R}^{6\times8}$ is the input matrix, $\boldsymbol{u} \in \mathbb{R}^{8\times1}$ is the thrust vector, $\boldsymbol{T} > 0 \in \mathbb{R}^{8\times8}$ is a diagonal matrix of time-constants and $\boldsymbol{u}_c \in \mathbb{R}^{8\times1}$ is the commanded thrust vector. The relative velocity vector is defined as $\boldsymbol{\nu}_r = \boldsymbol{\nu} - \boldsymbol{\nu}_c \in \mathbb{R}^{6\times1}$ where $\boldsymbol{\nu}_c$ is the ocean current velocity vector.

The mathematical modeling of Merlin WR200 follow from Knausgård (2012) and Knausgård (2013) which is based on notations from Thor I. Fossen (2011). The nominal parameters of Merlin in a neutral configuration are given in Table 3.2 and in Appendix E.

Table 3.2: Merlin WR200 parameters

Parameter	Value	Unit
Mass	3000	kg
Length	2.8	m
Width	1.8	m
Height	1.7	m
Volume	3.22	m^3
Dist. CG	$[-0.002341, 0.003014, -0.021193]$	m
Dist. CB	$[0, 0, -0.2]$	m

Inertia matrix and added mass

The rigid body mass matrix is presented as

$$\mathbf{M}_{RB} = \begin{bmatrix} m & 0 & 0 & 0 & mz_g & -my_g \\ 0 & m & 0 & -mz_g & 0 & mx_g \\ 0 & 0 & m & my_g & -mx_g & 0 \\ 0 & -mz_g & my_g & I_{xx} & -I_{xy} & I_{xz} \\ mz_g & 0 & -mx_g & -I_{yx} & I_{yy} & -I_{yz} \\ -my_g & mx_g & 0 & -I_{zx} & -I_{zy} & I_{zz} \end{bmatrix} \tag{3.18}$$

where m is the mass and r_g is the distance from Center of Origin (CO) to Center of Gravity (CG). For a neutral configuration, the inertia about CG is given as (Appendix E):

$$\mathbf{I}_{RB} = \begin{bmatrix} 1819 & 0 & -120 \\ 0 & 3064 & 7 \\ -120 & 7 & 2887 \end{bmatrix} \tag{3.19}$$

The added mass matrix $\mathbf{M}_A$ consist of 36 elements, which is approximated with 6 diagonal elements based on assumptions in Knausgård (2013). It is assumed that the added mass in surge, sway and heave is 10 % of the mass, and 5% of the inertia in roll, pitch and yaw. Knausgård (2013) suggest to tune these values upon implementation if necessary. The approximated added mass matrix

becomes

$$\mathbf{M}_A = -\begin{bmatrix} -300 & 0 & 0 & 0 & 0 & 0 \\ 0 & -300 & 0 & 0 & 0 & 0 \\ 0 & 0 & -300 & 0 & 0 & 0 \\ 0 & 0 & 0 & -159.2 & 0 & 0 \\ 0 & 0 & 0 & 0 & -159.2 & 0 \\ 0 & 0 & 0 & 0 & 0 & -159.2 \end{bmatrix} \tag{3.20}$$

The total mass matrix is given by

$$\mathbf{M} = \mathbf{M}_{RB} + \mathbf{M}_A \tag{3.21}$$

$$= \begin{bmatrix} 3300 & 0 & 0 & 0 & -67.5 & -9.6 \\ 0 & 3300 & 0 & 67.5 & 0 & -7.5 \\ 0 & 0 & 3300 & 9.6 & 7.5 & 0 \\ 0 & 67.5 & 9.6 & 1978.2 & 0 & -120 \\ -67.5 & 0 & 7.5 & 0 & 3223.2 & 7 \\ -9.6 & -7.5 & 0 & -120 & 7 & 3046.2 \end{bmatrix} \tag{3.22}$$

Coriolis and centripetal matrix

The rigid body Coriolis and centripetal matrix is

$$\mathbf{C}_{RB} = \begin{bmatrix} m\mathbf{S}(\boldsymbol{\omega}^b_{b/n}) & -m\mathbf{S}(\boldsymbol{\omega}^b_{b/n})\mathbf{S}(\mathbf{r}^b_g) \\ m\mathbf{S}(\boldsymbol{\omega}^b_{b/n})\mathbf{S}(\mathbf{r}^b_g) & -\mathbf{S}(\boldsymbol{I}_b\boldsymbol{\omega}^b_{b/n}) \end{bmatrix} \tag{3.23}$$

where $\mathbf{S}(\lambda)\mathbf{a} = \lambda \times \mathbf{a}$ is the cross-product operator, and $\mathbf{I}_b = \mathbf{I}_{RB} - m\mathbf{S}^2(\mathbf{r}^b_g)$ is the inertia matrix about an arbitrary CO. The added mass Coriolis and centripetal matrix is

$$\mathbf{C}_A = \begin{bmatrix} \mathbf{0}_{3x3} & -\mathbf{S}(\mathbf{A}_{11}\boldsymbol{\nu} + \mathbf{A}_{12}\boldsymbol{\omega}) \\ -\mathbf{S}(\mathbf{A}_{11}\boldsymbol{\nu} + \mathbf{A}_{12}\boldsymbol{\omega}) & -\mathbf{S}(\mathbf{A}_{21}\boldsymbol{\nu} + \mathbf{A}_{22}\boldsymbol{\omega}) \end{bmatrix} \tag{3.24}$$

where $\mathbf{A}_{ij}$ are taken from the added mass matrix

$$\mathbf{M}_A = \begin{bmatrix} \mathbf{A}_{11} & \mathbf{A}_{12} \\ \mathbf{A}_{21} & \mathbf{A}_{22} \end{bmatrix} \tag{3.25}$$

The Coriolis and centripetal matrices are not given further attention in this thesis as they are not used in the developed control system.

Hydrodynamical damping matrix

The damping of an underwater vehicle performing DP or motions at higher speed, will in general be dominated by nonlinear terms (Thor I. Fossen 2011, p. 138 and p.182). To avoid oscillatory behavior in low-speed applications such as station keeping, Thor I. Fossen (2011, p. 137) suggest to include a linear damping term according to

$$\mathbf{D}(\boldsymbol{\nu}) = \mathbf{D}_L + \mathbf{D}_{NL}(\boldsymbol{\nu}) \tag{3.26}$$

However, drag tests performed in Knausgård (2012) showed clear quadratic damping in surge and sway. Due to plane symmetry, the damping in heave is assumed to be equal to damping in sway. The damping coefficients for roll, pitch and yaw are approximated as the 10 % of the average of the damping in surge and sway (Knausgård 2013). They may be tuned upon implementation. No data exist for linear damping leading to the assumption $\mathbf{D}_L \approx \mathbf{0}$. Furthermore, assuming Merlin WR200 will for the most part perform decoupled motions, the structure of the damping matrix is assumed to be diagonal (Thor I. Fossen 2011, p. 137). Thus, the damping matrix is presented as

$$\mathbf{D}(\boldsymbol{\nu}) = \begin{bmatrix} X_{|u|u}|u| & 0 & 0 & 0 & 0 & 0 \\ 0 & Y_{|v|v}|v| & 0 & 0 & 0 & 0 \\ 0 & 0 & Z_{|w|w}|w| & 0 & 0 & 0 \\ 0 & 0 & 0 & K_{|p|p}|p| & 0 & 0 \\ 0 & 0 & 0 & 0 & M_{|q|q}|q| & 0 \\ 0 & 0 & 0 & 0 & 0 & N_{|r|r}|r| \end{bmatrix} \tag{3.27}$$

$$= \mathrm{diag}\{1321|u|, 2525|v|, 2525|w|, 192|p|, 192|q|, 192|r|\} \tag{3.28}$$

Hydrostatic restoring forces

The restoring forces matrix is given as

$$\mathbf{g}(\boldsymbol{\eta}) = \begin{bmatrix} & (W-B)\sin\theta & & \\ - & (W-B)\cos\theta\sin\phi & & \\ - & (W-B)\cos\theta\cos\phi & & \\ - & (y_gW - y_bB)\cos\theta\cos\phi & + & (z_gW - z_bB)\cos\theta\sin\phi \\ & (z_gW - z_bB)\sin\theta & + & (x_gW - x_bB)\cos\theta\cos\phi \\ - & (x_gW - x_bB)\cos\theta\sin\phi & - & (y_gW - y_bB)\sin\theta \end{bmatrix} \tag{3.29}$$

in which r_b is the distance from CO to CB, $W = m\mathrm{g}$ and $B = \rho \mathrm{g} V$. Gravitational acceleration is $\mathrm{g} = 9.81$ m/s^2, density of sea water is $\rho = 1024$ kg/m^3 and the volume of Merlin is $V = 3.22\mathrm{m}^3$.

One may approximate the natural periods of heave, roll and pitch by considering linear, decoupled equations of motion (Thor I. Fossen 2011, p.68) based on (3.16). This gives the following expression for the natural periods:

$$\omega_i = \sqrt{\frac{C_{ii}}{\mathbf{M}_{ii}}} \tag{3.30}$$

where C_{ii} are the linear spring stiffness coefficients resulting from linearizing $\mathbf{g}(\boldsymbol{\eta})$ about zero roll and pitch angles, and $\mathbf{M} = \mathbf{M}_{RB} + \mathbf{M}_A$ as in Equation (3.21). Assuming CB lies directly above CG, one arrives at $C_{44} = C_{55} = |z_b|B$ and $C_{33} = -(W - B)$. The estimated roll and pitch angles are sensitive to variations in z_b, which should be known with some certainty. The expected natural periods for Merlin WR200 in a neutral configuration are given in Table 3.3.

Table 3.3: Expected natural periods in heave, roll and pitch

DOF	Period	Unit
Heave	6.7	s
Roll	4.5	s
Pitch	5.7	s

Ocean currents

The generalized ocean current velocity of an irrotational fluid is expressed in the body-frame as (Thor I. Fossen 2011)

$$\boldsymbol{\nu}_c^b = [\underbrace{u_c, v_c, w_c}_{v_c^b}, 0, 0, 0]^\top \tag{3.31}$$

The current is described in the NED-frame with velocity V_c, horizontal bearing β_c and vertical bearing α_c, which may be modeled as slowly varying processes for computer simulations. In the NED-frame, the ocean current is modeled as

$$\mathbf{v}_c^n = \mathbf{R}_{y,\alpha_c}^\top \mathbf{R}_{z,-\beta_c}^\top \begin{bmatrix} V_c \\ 0 \\ 0 \end{bmatrix} \tag{3.32}$$

This is modeled in the body-frame as

$$\mathbf{v}_c^b = \mathbf{R}_b^n(\boldsymbol{\Theta}_{nb})^\top \mathbf{v}_c^n \tag{3.33}$$

3.4.2 Control Plant Model

The following assumptions are made in the development of the control plant model

Assumption 3.1. *The roll and pitch angles are small such that $\phi = \theta \approx 0$. This leads to a simplified transformation matrix between $\{n\}$ and $\{b\}$:*

$$\boldsymbol{P}(\psi) = \begin{bmatrix} \boldsymbol{R}_z(\psi) & \boldsymbol{0}_{3x3} \\ \boldsymbol{0}_{3x3} & \boldsymbol{I}_{3x3} \end{bmatrix} \tag{3.34}$$

Assumption 3.2. *The ROV operates at small velocities such that the Coriolis and centripetal matrix can be neglected.*

Assumption 3.3. *CO coincides with CG and CB is located directly above CG such that $x_g = y_g = z_g = x_b = y_b = 0$.*

Assumption 3.4. *The restoring forces matrix $\boldsymbol{g}(\boldsymbol{\eta})$ is known but is modeled as a disturbance.*

Assumption 3.5. *The ocean current $\boldsymbol{\nu}_c^b$ cannot be measured and the effect of current is modeled as a disturbance.*

Assumption 3.6. *Despite the TMS it is assumed that some disturbance is caused by the tether.*

Applying the above assumptions results in the simplified model of the equations of motion

$$\dot{\boldsymbol{\eta}} = \boldsymbol{P}(\psi)\boldsymbol{\nu} \tag{3.35}$$

$$\boldsymbol{M}\dot{\boldsymbol{\nu}} + \boldsymbol{D}(\boldsymbol{\nu})\boldsymbol{\nu} = \boldsymbol{B}\boldsymbol{u} + \boldsymbol{\tau}_d \tag{3.36}$$

$$\boldsymbol{T}\dot{\boldsymbol{u}} = -\boldsymbol{u} + \boldsymbol{u}_c \tag{3.37}$$

where $\boldsymbol{M} = \boldsymbol{M}_{\mathrm{RB}}^{\mathrm{CG}} + \boldsymbol{M}_{\mathrm{A}}$ and $\boldsymbol{\tau}_d = \boldsymbol{\tau}_c + \boldsymbol{\tau}_{\mathrm{umb}} - \Delta\boldsymbol{M}\dot{\boldsymbol{\nu}} - \Delta\boldsymbol{D}(\boldsymbol{\nu})\boldsymbol{\nu} - \boldsymbol{g}(\boldsymbol{\eta})$ is a lumped disturbance vector accounting for disturbances caused by current, tether cable and unmodelled dynamics. Note that no assumptions are made regarding the nature of the current or the disturbance caused by the tether other than potentially being present.

3.5 Thrusters

Merlin WR200 is equipped with 8 thrusters; 4 in the horizontal plane and 4 in the vertical plane. Thus Merlin WR200 is an *over-actuated* system. Due to a mechanical restriction in the gearbox, the rise-time from zero to maximum thrust is configured to be 1.2 seconds by applying a ramp-filter in the frequency converters. The resulting rise-time is considered large enough for the actuator dynamics to be included in the dynamic model of Merlin, where a first order model is used as an approximation in Equation (3.37). There is no feedback from the applied thrust, but using an accurate model, one may calculate an approximation based on the frequency output from the ramp-filter. The thrust allocation procedure consist of allocation, normalization and mapping from force to frequency (Fig. 3.4), which will be explained below.

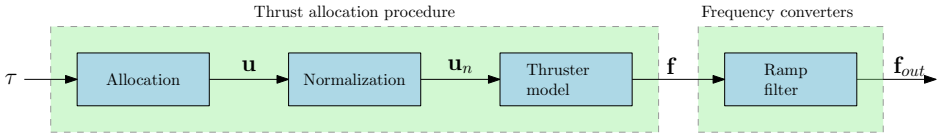

Figure 3.4: Thrust allocation deals with distributing the control force to the actuators. Normalization is applied to maintain the ratio of the desired input in case of saturation. A model of the thrusters is used to map the desired force to a frequency that is input to the frequency transformers, which control the power to the thrusters. The transformers use a ramp filter to limit wear and tear on the thrusters, which introduce a delay in the control loop.

3.5.1 Thrust allocation

The thrust allocation problem deals with producing the generalized input vector $\boldsymbol{\tau} = [X\ Y\ Z\ K\ M\ N]^\top$ using the 8 thrusters $\mathbf{u}$. This is done by first defining the thrust configuration matrix $\boldsymbol{B}$ such that

$$\boldsymbol{\tau} = \boldsymbol{B}\boldsymbol{u} \tag{3.38}$$

where $\boldsymbol{B}$ describes how each thruster is affecting the 6 degrees of freedom. The control system will calculate the generalized input vector $\boldsymbol{\tau}$ and the individual thruster commands are found by inverting (3.38). Since $\boldsymbol{B}$ is not square, the inverse is found by taking the *Moore-Penrose pseudoinverse*. This gives

$$\boldsymbol{u} = \mathbf{B}^\top(\mathbf{B}\mathbf{B}^\top)^{-1} = \boldsymbol{B}^\dagger\boldsymbol{\tau} \tag{3.39}$$

The matrix $\boldsymbol{B}$ is defined to fit the simulator at IKM Subsea Solutions and contains some differences from Knausgård (2013) and Ohrem (2015).

$$\boldsymbol{B} = \begin{bmatrix} \mathrm{s}\alpha & \mathrm{s}\alpha & -\mathrm{s}\alpha & -\mathrm{s}\alpha & 0 & 0 & 0 & 0 \\ \mathrm{c}\alpha & -\mathrm{c}\alpha & \mathrm{c}\alpha & -\mathrm{c}\alpha & 0 & 0 & 0 & 0 \\ 0 & 0 & 0 & 0 & -1 & -1 & -1 & -1 \\ l_5\mathrm{c}\alpha & -l_5\mathrm{c}\alpha & l_5\mathrm{c}\alpha & -l_5\mathrm{c}\alpha & l_2 & -l_2 & l_2 & -l_2 \\ -l_5\mathrm{s}\alpha & -l_5\mathrm{s}\alpha & l_5\mathrm{s}\alpha & l_5\mathrm{s}\alpha & l_3 & l_3 & -l_1 & -l_1 \\ l_4 & -l_4 & -l_6 & l_6 & 0 & 0 & 0 & 0 \end{bmatrix} \tag{3.40}$$

in which $\alpha = 45°$ is the angle of the thruster in the xy-plane and $\mathrm{s}\alpha = \sin(\alpha)$ and $\mathrm{c}\alpha = \cos(\alpha)$. The moment arms l_i are as defined in Knausgård (2013) (Table 3.4, Fig. 3.5a, 3.5b and 3.6). It should be noted that the moment arms are only valid for Merlin in a neutral configuration, as the COG shifts when equipping the ROV with additional tools and skids.

Table 3.4: The moment arms from the CO of Merlin to the thrusters.

Arm	Length	Unit
l_1	0.73	m
l_2	0.24	m
l_3	0.73	m
l_4	0.84	m
l_5	0.10	m
l_6	0.84	m

3.5.2 Normalization

Knausgård (2013) suggest to normalize the commanded thrust to maintain the ratio if the desired force exceeds the limitations of the thrusters. The normalization scheme is presented as

$$u_{max} = \max\left(|u_1|, \ldots, |u_8|\right) \tag{3.41}$$

$$u_i = \begin{cases} u_i, & u_{max} < u_{sat} \\ \frac{u_i}{u_{max}} u_{sat}, & \text{otherwise} \end{cases} \tag{3.42}$$

where u_{sat} is a predefined saturation limit. Measures are also taken at higher levels in the control system to prevent saturation. The scheme presented here acts as an additional precaution.

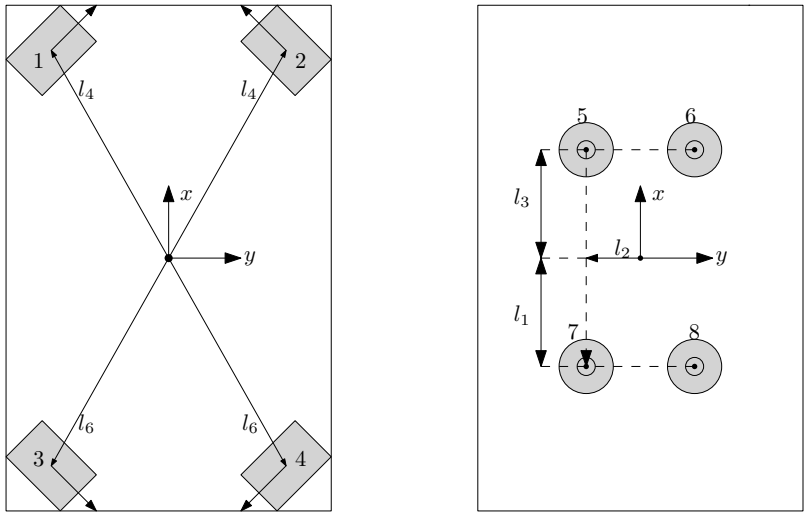

(a) Horizontal thrusters **(b)** Vertical thrusters

Figure 3.5: Sketch of Merlin WR200 in the XY-plane with horizontal thrusters (left) vertical thrusters (right). The arrow out of the thrusters indicate positive direction of thrust

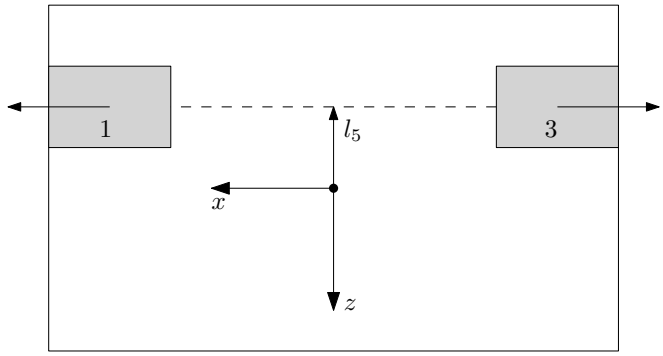

Figure 3.6: Sketch of Merlin WR200 in the XZ-plane. The arrow out of the thrusters indicate positive direction of thrust.

3.5.3 Thruster model

The next step is to make each thruster produce the amount of thrust determined by Equation (3.39). The electrical thrusters are controlled by frequency con-

verters such that there is need for a mapping between thrust and frequency. A bollard pull test was reported in Knausgård (2012) giving rise to experimental data relating these quantities. A basic thruster model is given by (Carlton 1994)

$$u_i = K_T(J)\rho D^4 |f_i| f_i \tag{3.43}$$

where $K_T(J)$ is the thrust coefficient, ρ is the density of water, D is the propeller diameter, f is the frequency, $J = V_a/fD$ is the advance ratio and V_a is the inflow water velocity to the propeller. The experiment did only consider stationary water, such that $J = 0$ in the model. This is an good approximation for calm seas and low velocities. See eg. Dukan (2014) and Ludvigsen and Ødegaard (2005) for the case where $K_T(J)$ can be determined in experiments.

Based on the experimental data provided in Knausgård (2013), the following mapping is found

$$u_i = k|f_i|f_i \tag{3.44}$$

with $k = 0.2974$. The new model shows a closer fit with the experimental data (Fig. 3.7a and 3.7b) than the model presented in Knausgård (2013). The input to the frequency converters is calculated according to

$$f_i = \text{sign}(u_i)\sqrt{\frac{|u_i|}{k}} \tag{3.45}$$

It should be noted that while the maximum theoretical thrust is about 2800 N at 75 Hz, the experimental data indicate about 1700 N at the same frequency. Loss of thrust due to thruster-thruster interaction (Asgeir J Sørensen 2013, p. 308) is expected for Merlin WR200 due to the orientation of the thrusters in the horizontal plane. In ideal conditions, the gain k in Equation (3.44) would be $k = 0.4978$. The gain may be tuned in the interval $\langle 0.3, 0.5 \rangle$ upon implementation.

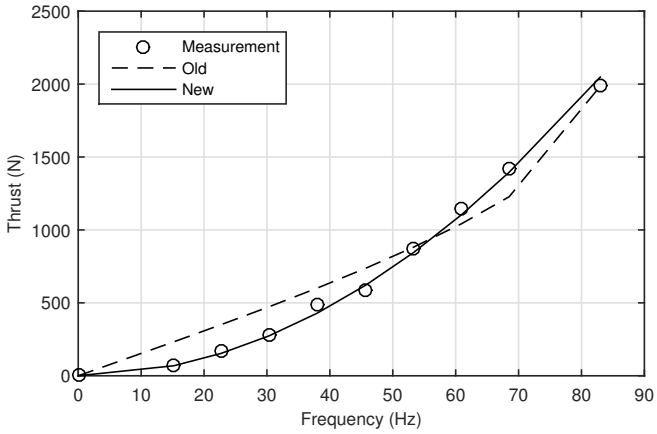

(a) Frequency to thrust mapping.

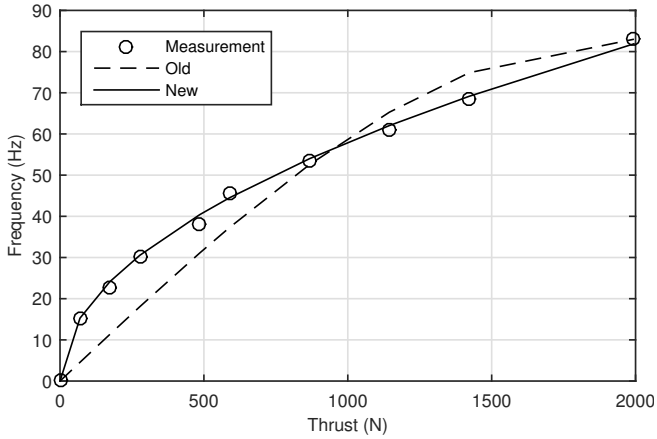

(b) Thrust to frequency mapping.

Figure 3.7: The new thruster model use a quadratic mapping whereas the former used a sine function. The new mapping show a closer fit with the experimental data.

Chapter 4

Motion Control System

This chapter presents the development of a dynamic positioning system for Merlin WR200. The objective of this thesis has been to add compensation for tether disturbances and include the actuator dynamics in the control loop. In an iterative process, the Parameter and Current Backstepping Controller (PCABS) from Ohrem (2015) was improved by redefining the adaptive term to exploit the natural damping in the system. Additional disturbance suppression was achieved with a disturbance observer, and the controller was further designed to compensate for the slow dynamic response in the thrusters. In order to arrive at the final control law, PCABS was first extended to 6 DOF by modifying the regressor matrix to include roll and pitch. PCABS adopts an idea from Antonelli et al. (2001) that parameterizes the current in an elegant way in the regressor. However, to also compensate for tether and other disturbances, a disturbance observer was introduced and put in parallel with parameter adaptation. This intermediate control system is referred to as PCABS-D in the rest of this thesis. The New Control System (NCS) makes minor structural changes based on PCABS-D and also add compensation of actuator dynamics to the loop (Fig 4.1). Both adaptation and disturbance observer provide integral action to the controller, thus both are collectively referred to as *integral action* or *integral terms* in the rest of this thesis. The following sections gives the derivation of the final controller including modified parameter adaptation and disturbance observer. Chapter 7 compares the controllers in a simulation study in order to document the effect of the proposed changes.

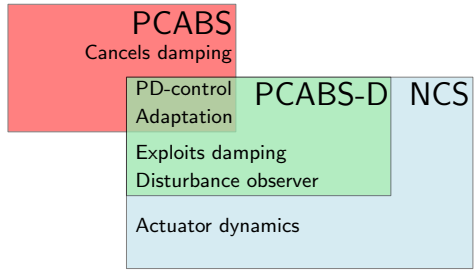

Figure 4.1: The PCABS controller forms the basis for the control system developed in this thesis, for which the intermediate controller PCABS-D and final controller NCS builds upon.

4.1 Basic disturbance observer structure

The principle of the disturbance observer is to balance Newton's second law. Using the equations of motion from Equation (3.36) and $\boldsymbol{\tau} = \mathbf{Bu}$, the disturbances can be calculated as

$$\boldsymbol{\tau}_d = \boldsymbol{M}\dot{\boldsymbol{\nu}} + \boldsymbol{D}(\boldsymbol{\nu})\boldsymbol{\nu} - \boldsymbol{\tau} \tag{4.1}$$

If measurements of the acceleration $\dot{\boldsymbol{\nu}}$ exist, a basic observer model as in Chen et al. (2000) is suggested for Merlin:

$$\dot{\hat{\boldsymbol{\tau}}}_d = -\mathbf{L}\hat{\boldsymbol{\tau}}_d + \mathbf{L}\big(\mathbf{M}\dot{\boldsymbol{\nu}} + \mathbf{D}(\boldsymbol{\nu})\boldsymbol{\nu} - \boldsymbol{\tau}\big) \tag{4.2}$$

4.1.1 Modified disturbance observer

A modification can be made to avoid using measurements of the acceleration $\dot{\boldsymbol{\nu}}$ (Fig. 4.2). This is beneficial since these measurements may not be accurate or contaminated with noise. As in Chen et al. (2000), the modification is done by introducing the auxiliary variable $\mathbf{x}_{dob}$ defined as

$$\mathbf{x}_{dob} = \hat{\boldsymbol{\tau}}_d - \mathbf{p}(\boldsymbol{\nu}) \tag{4.3}$$

where $\mathbf{p}(\boldsymbol{\nu})$ can be determined from the modified observer gain $\mathbf{L}$:

$$\dot{\mathbf{p}}(\boldsymbol{\nu}) = \mathbf{LM}\dot{\boldsymbol{\nu}} \tag{4.4}$$

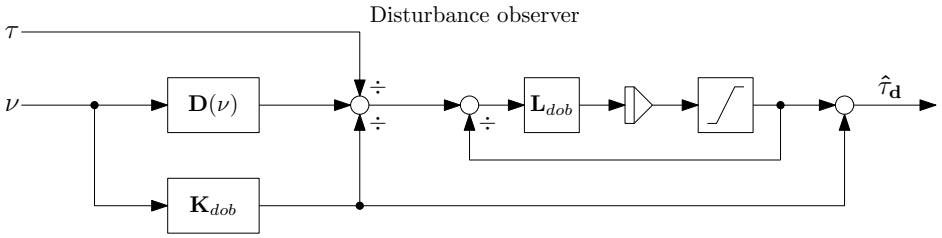

Figure 4.2: Disturbance observer based on Chen et al. (2000) that avoids using the measured acceleration of the vehicle. An estimate of the disturbance is made by balancing the equations of motion. A saturating element is used to keep the estimate within an acceptable range.

Taking the time derivative of (4.3) gives

$$\dot{\mathbf{x}}_{dob} = -\mathbf{L}\hat{\boldsymbol{\tau}}_d + \mathbf{L}\big(\mathbf{M}\dot{\boldsymbol{\nu}} + \mathbf{D}(\boldsymbol{\nu})\boldsymbol{\nu} - \boldsymbol{\tau}\big) - \mathbf{L}\mathbf{M}\dot{\boldsymbol{\nu}} \tag{4.5}$$

$$= -\mathbf{L}\big(\mathbf{x}_{dob} + \mathbf{p}(\boldsymbol{\nu})\big) + \mathbf{L}\big(\mathbf{M}\dot{\boldsymbol{\nu}} + \mathbf{D}(\boldsymbol{\nu})\boldsymbol{\nu} - \boldsymbol{\tau}\big) - \mathbf{L}\mathbf{M}\dot{\boldsymbol{\nu}} \tag{4.6}$$

$$= -\mathbf{L}\mathbf{x}_{dob} + \mathbf{L}\big(\mathbf{D}(\boldsymbol{\nu})\boldsymbol{\nu} - \mathbf{p}(\boldsymbol{\nu}) + \boldsymbol{\tau}\big) \tag{4.7}$$

The estimate of the disturbances are then found from rearranging (4.3)

$$\hat{\boldsymbol{\tau}}_d = \mathbf{x}_{dob} + \mathbf{p}(\boldsymbol{\nu}) \tag{4.8}$$

Based on the results from Mohammadi et al. (2013) the observer gain matrix is chosen as the constant matrix

$$\mathbf{L} = \mathbf{K}_{dob}\hat{\mathbf{M}}^{-1} \tag{4.9}$$

where $\mathbf{K}_{dob}$ is a positive definite and symmetric matrix, and $\hat{\mathbf{M}}$ is an estimate of the mass matrix. With this choice of observer gain it is seen from (4.4) that

$$\mathbf{p}(\boldsymbol{\nu}) = \mathbf{K}_{dob}\boldsymbol{\nu} \tag{4.10}$$

4.1.2 Stability analysis of the disturbance observer

The error dynamics of the modified disturbance observer becomes

$$\begin{aligned}
\Delta\dot{\boldsymbol{\tau}}_d &= \dot{\boldsymbol{\tau}}_d - \dot{\hat{\boldsymbol{\tau}}}_d && (4.11)\\
&= \dot{\boldsymbol{\tau}}_d - \dot{\boldsymbol{x}}_{dob} - \dot{\mathbf{p}}(\boldsymbol{\nu}) && (4.12)\\
&= \dot{\boldsymbol{\tau}}_d + \mathbf{L}\mathbf{x}_{dob} - \mathbf{L}\big(\mathbf{D}(\boldsymbol{\nu})\boldsymbol{\nu} - \mathbf{p}(\boldsymbol{\nu}) + \boldsymbol{\tau}\big) - \mathbf{L}\hat{\mathbf{M}}\dot{\boldsymbol{\nu}} && (4.13)\\
&= \dot{\boldsymbol{\tau}}_d + \mathbf{L}\big(\hat{\boldsymbol{\tau}}_d - \mathbf{p}(\boldsymbol{\nu})\big) - \mathbf{L}\big(\boldsymbol{\tau}_d - \mathbf{M}\dot{\boldsymbol{\nu}} - \mathbf{p}(\boldsymbol{\nu})\big) - \mathbf{L}\hat{\mathbf{M}}\dot{\boldsymbol{\nu}} && (4.14)\\
&= \dot{\boldsymbol{\tau}}_d - \mathbf{L}\Delta\boldsymbol{\tau}_d && (4.15)
\end{aligned}$$

Consider the following Lyapunov function candidate and assume $\|\dot{\boldsymbol{\tau}}_{\boldsymbol{d}}\| \leq \kappa$

$$V(\Delta\boldsymbol{\tau}_d, t) = \frac{1}{2}\Delta\boldsymbol{\tau}_d^\top \mathbf{Q}\Delta\boldsymbol{\tau}_d \tag{4.16}$$

where $\mathbf{Q} = \mathbf{K}_{dob}^{-\top}\mathbf{M}\mathbf{K}_{dob}^{-1}$ is positive definite since $\mathbf{M}$ is symmetric and positive definite and $\mathbf{K}_{dob}$ is invertible. The time derivative results in

$$\begin{aligned}
\dot{V} &= \Delta\boldsymbol{\tau}_d^\top \mathbf{Q}(\dot{\boldsymbol{\tau}}_d - \mathbf{L}\Delta\boldsymbol{\tau}_d) && (4.17)\\
&= -\Delta\boldsymbol{\tau}_d^\top \mathbf{Q}\mathbf{L}\boldsymbol{\tau}_d + \Delta\boldsymbol{\tau}_d^\top \mathbf{Q}\dot{\boldsymbol{\tau}}_d && (4.18)\\
&\leq -\lambda_1 \|\Delta\boldsymbol{\tau}_d\|^2 + \lambda_2\kappa \|\Delta\boldsymbol{\tau}_d\| && (4.19)\\
&\leq -(1-\gamma)\lambda_1 \|\Delta\boldsymbol{\tau}_d\|^2 - \gamma\lambda_1 \|\Delta\boldsymbol{\tau}_d\|^2 + \lambda_2\kappa \|\Delta\boldsymbol{\tau}_d\| && (4.20)\\
&\leq -(1-\gamma)\lambda_1 \|\Delta\boldsymbol{\tau}_d\|^2, \quad \forall \|\Delta\boldsymbol{\tau}_d\| \geq \frac{\kappa\lambda_2}{\gamma\lambda_1} = \mu && (4.21)
\end{aligned}$$

where λ_1 is the smallest eigenvalue of $\mathbf{QL} = \mathbf{K}_{dob}^{-\top}$, λ_2 is the smallest eigenvalue of $\mathbf{Q}$ and $\gamma \in (0, 1)$.

Constant disturbance

If the disturbances are constant, then the estimation error is globally asymptotically stable. Furthermore, the bounds of V can be written $\lambda_{min}(\mathbf{Q}) \|\Delta\boldsymbol{\tau}_d\|^2 \leq V \leq \lambda_{max}(\mathbf{Q}) \|\Delta\boldsymbol{\tau}_d\|^2$ and rearranged to give $\|\Delta\boldsymbol{\tau}_d\|^2 \geq V/\lambda_{max}(\mathbf{Q})$. Thus

$$\dot{V} = -\lambda_1 \|\Delta\boldsymbol{\tau}_d\|^2 \leq -\frac{\lambda_1}{\lambda_{max}(\mathbf{Q})} V \tag{4.22}$$

which is a stable, linear, ordinary differential equation, meaning that the estimation error is globally exponentially stable if the disturbances are assumed constant (Khalil 2000, Theorem 4.10). This can also be seen directly in Equation (4.15) which is also an ordinary differential equation when $\dot{\boldsymbol{\tau}}_d = \mathbf{0}$.

Bounded disturbance

If the disturbances are slowly varying with the upper bound κ, then the disturbance tracking error $\Delta\boldsymbol{\tau}_d$ is globally uniformly ultimately bounded (Khalil 2000, Theorem 4.18). Moreover, the ultimate bound is given by

$$b = \sqrt{\frac{\lambda_{max}(\mathbf{Q})\mu^2}{\lambda_{min}(\mathbf{Q})}} \tag{4.23}$$

$$= \sqrt{\frac{\lambda_{max}(\mathbf{Q})\lambda_{min}(\mathbf{Q})\kappa^2}{\lambda_1^2\gamma^2}} \tag{4.24}$$

The reader is referred to Mohammadi et al. (2013) for the general proof.

4.2 Dynamic Positioning Control Law

The control is law formulated in the framework of vectorial backstepping carried out in 3 successive steps. Position and orientation are stabilized in the first step, and velocity in the second. Compensation of actuator dynamics are designed in the third step along with a law for parameter adaptation. Figure 4.4 gives a block diagram of the developed controller.

4.2.1 Step 1 - Stabilize position and attitude

Let the actual and desired position of the ROV be denoted by $\boldsymbol{\eta}$ and $\boldsymbol{\eta}_d$, and further let the position error in Vessel Parallel coordinates be defined as $\tilde{\boldsymbol{\eta}}_p = \mathbf{P}^T(\psi)\big(\boldsymbol{\eta} - \boldsymbol{\eta}_d\big)$. Moreover, the velocity error is denoted $\tilde{\boldsymbol{\nu}} = \boldsymbol{\nu} - \boldsymbol{\nu}_d$.

Consider the positive definite candidate Lyapunov function

$$V_1(\tilde{\boldsymbol{\eta}}_p, t) = \frac{1}{2}\tilde{\boldsymbol{\eta}}_p^T\tilde{\boldsymbol{\eta}}_p, \qquad \forall\tilde{\boldsymbol{\eta}}_p \geq \mathbf{0} \tag{4.25}$$

Taking the time derivative and using Equation (3.13)

$$\dot{V}_1 = \tilde{\boldsymbol{\eta}}_p^T \big(r\mathbf{S}^\top \tilde{\boldsymbol{\eta}}_p + \tilde{\boldsymbol{\nu}} \big) \tag{4.26}$$

$$= r \underbrace{\tilde{\boldsymbol{\eta}}_p^T \mathbf{S}^\top \tilde{\boldsymbol{\eta}}_p}_{=0} + \tilde{\boldsymbol{\eta}}_p^\top \tilde{\boldsymbol{\nu}} \tag{4.27}$$

$$= \tilde{\boldsymbol{\eta}}_p^T \tilde{\boldsymbol{\nu}} \tag{4.28}$$

$$= \tilde{\boldsymbol{\eta}}_p^T \big(-\mathbf{K}_1 \tilde{\boldsymbol{\eta}}_p + \mathbf{s} \big) \tag{4.29}$$

$$= -\tilde{\boldsymbol{\eta}}_p^T \mathbf{K}_1 \tilde{\boldsymbol{\eta}}_p + \mathbf{s}^T \tilde{\boldsymbol{\eta}}_p \tag{4.30}$$

where $\mathbf{s} = \boldsymbol{\nu} - (\boldsymbol{\nu}_d - \mathbf{K}_1 \tilde{\boldsymbol{\eta}}_p) = \boldsymbol{\nu} - \boldsymbol{\nu}_v$ is a measure of tracking, $\mathbf{K}_1$ is a diagonal, positive definite matrix, and $\boldsymbol{\nu}_v$ is a virtual velocity vector. Stabilization of position is achieved by having $\boldsymbol{\nu}$ converge to $\boldsymbol{\nu}_v$.

4.2.2 Step 2 - Stabilize velocity

Consider the second candidate Lyapunov function

$$V_2(\tilde{\boldsymbol{\eta}}, \mathbf{s}, t) = V_1(\tilde{\boldsymbol{\eta}}_p, t) + \frac{1}{2}\mathbf{s}^T \mathbf{M} \mathbf{s} \tag{4.31}$$

The time derivative is

$$\dot{V}_2 = \dot{V}_1 + \mathbf{s}^T \mathbf{M} \big(\dot{\boldsymbol{\nu}} - \dot{\boldsymbol{\nu}}_{\boldsymbol{v}} \big) \tag{4.32}$$

$$= -\tilde{\boldsymbol{\eta}}_p^T \mathbf{K}_1 \tilde{\boldsymbol{\eta}}_p + \mathbf{s}^T \big(\tilde{\boldsymbol{\eta}}_p - \mathbf{D}(\boldsymbol{\nu})\boldsymbol{\nu} + \mathbf{B}\mathbf{u} + \boldsymbol{\tau}_d - \mathbf{M}\dot{\boldsymbol{\nu}}_{\boldsymbol{v}} \big) \tag{4.33}$$

$$= -\tilde{\boldsymbol{\eta}}_p^T \mathbf{K}_1 \tilde{\boldsymbol{\eta}}_p + \mathbf{s}^T \big(\tilde{\boldsymbol{\eta}}_p - \mathbf{D}(\boldsymbol{\nu})\mathbf{s} - \mathbf{D}(\boldsymbol{\nu})\boldsymbol{\nu}_v + \mathbf{B}\mathbf{u} + \boldsymbol{\tau}_d - \mathbf{M}\dot{\boldsymbol{\nu}}_{\boldsymbol{v}} \big) \tag{4.34}$$

$$= -\tilde{\boldsymbol{\eta}}_p^T \mathbf{K}_1 \tilde{\boldsymbol{\eta}}_p - \mathbf{s}^T \mathbf{D}(\boldsymbol{\nu})\mathbf{s} + \mathbf{s}^T \big(\mathbf{B}\mathbf{u} - \mathbf{M}\dot{\boldsymbol{\nu}}_{\boldsymbol{v}} - \mathbf{D}(\boldsymbol{\nu})\boldsymbol{\nu}_v + \tilde{\boldsymbol{\eta}}_p + \boldsymbol{\tau}_d \big) \tag{4.35}$$

$$= -\tilde{\boldsymbol{\eta}}_p^T \mathbf{K}_1 \tilde{\boldsymbol{\eta}}_p - \mathbf{s}^T \mathbf{D}(\boldsymbol{\nu})\mathbf{s} + \mathbf{s}^T \big(\mathbf{B}\mathbf{u} - \boldsymbol{\phi}(\dot{\boldsymbol{\nu}}_v, \boldsymbol{\nu}_v)^T \boldsymbol{\theta} + \tilde{\boldsymbol{\eta}}_p + \boldsymbol{\tau}_d \big) \tag{4.36}$$

where $\boldsymbol{\phi}(\dot{\boldsymbol{\nu}}_v, \boldsymbol{\nu}_v)^T \boldsymbol{\theta} = \mathbf{M}\dot{\boldsymbol{\nu}}_{\boldsymbol{v}} + \mathbf{D}(\boldsymbol{\nu})\boldsymbol{\nu}_v$. The regressor $\boldsymbol{\phi}(\dot{\boldsymbol{\nu}}_v, \boldsymbol{\nu}_v) \in \mathbb{R}^{12\times 6}$ is a matrix of known signals and $\boldsymbol{\theta} \in \mathbb{R}^{12\times 1}$ is a vector of unknown parameters. Note that the damping term $\mathbf{D}(\boldsymbol{\nu})\boldsymbol{\nu}$ is split into two terms in Equation (4.34) in order to exploit the dissipative damping in the system with the term $\mathbf{s}^\top \mathbf{D}(\boldsymbol{\nu})$ where $\mathbf{D}(\boldsymbol{\nu}) \geq 0$ is strictly positive.

If a disturbance observer is used, one can either assume $\boldsymbol{\tau}_d$ can be perfectly canceled or that residuals $\boldsymbol{\epsilon} = \boldsymbol{\tau}_d - \hat{\boldsymbol{\tau}}_{\boldsymbol{d}}$ remain, as in Wei et al. (2015). In that case the the regressor and parameter vector must be redefined to include these terms. Note that if a disturbance observer is not used, $\boldsymbol{\tau}_d$ should still be parameterized in the regressor in some way. In Ohrem (2015) the disturbance was assumed to be a two-dimensional current being constant in $\{n\}$. However, in this thesis it is assumed that the residuals are small and can be ignored.

Input-to-state stability in presence of unmodeled disturbances

If assumed that the parameter vector $\boldsymbol{\theta}$ is perfectly known and that actuator dynamics can be neglected, then the control law can be chosen as in Equation (4.37).

$$\mathbf{Bu} = \boldsymbol{\phi}(\dot{\boldsymbol{\nu}}_v, \boldsymbol{\nu}_v)^\top \boldsymbol{\theta} - \tilde{\boldsymbol{\eta}}_p - \mathbf{K}_2\mathbf{s} \tag{4.37}$$

The time derivative of V_2 becomes

$$\dot{V}_2 = -\tilde{\boldsymbol{\eta}}_p^T \mathbf{K}_1 \tilde{\boldsymbol{\eta}}_p - \mathbf{s}^T \big(\mathbf{D}(\boldsymbol{\nu}) + \mathbf{K}_2\big)\mathbf{s} + \mathbf{s}^\top \boldsymbol{\tau}_d \tag{4.38}$$

Let $\mathbf{x} = [\tilde{\boldsymbol{\eta}}_p \ \mathbf{s}]^\top$ and $\mathbf{K}(\boldsymbol{\nu}) = \text{diag}\{\mathbf{K}_1, \ \mathbf{D}(\boldsymbol{\nu}) + \mathbf{K}_2\}$. This gives

$$\begin{aligned}
\dot{V}_2 &= -\mathbf{x}^\top \mathbf{K}(\boldsymbol{\nu})\mathbf{x} + \mathbf{s}^\top \boldsymbol{\tau}_d && (4.39)\\
&\leq -\lambda_K(\boldsymbol{\nu}) \left\|\boldsymbol{x}\right\|^2 + \left\|\boldsymbol{s}\right\| \left\|\boldsymbol{\tau}_d\right\| && (4.40)\\
&\leq -\lambda_K(\boldsymbol{\nu}) \left\|\boldsymbol{x}\right\|^2 + \left\|\boldsymbol{x}\right\| \left\|\boldsymbol{\tau}_d\right\| && (4.41)\\
&\leq -(1-\gamma)\lambda_K(\boldsymbol{\nu}) \left\|\boldsymbol{x}\right\|^2 - \gamma\lambda_K(\boldsymbol{\nu}) \left\|\boldsymbol{x}\right\|^2 + \left\|\boldsymbol{x}\right\| \left\|\boldsymbol{\tau}_d\right\| && (4.42)\\
&\leq -(1-\gamma)\lambda_K(\boldsymbol{\nu}) \left\|\boldsymbol{x}\right\|^2 \leq 0, \quad \forall \left\|\boldsymbol{x}\right\| \geq \frac{\left\|\boldsymbol{\tau}_d\right\|}{\gamma\lambda_K(\boldsymbol{\nu})} && (4.43)
\end{aligned}$$

where $0 < \gamma < 1$ and $\left\|\cdot\right\|^2$ is the Euclidean norm. For every velocity $\boldsymbol{\nu}$, $\lambda_K(\boldsymbol{\nu})$ denotes the smallest eigenvalue of $\mathbf{K}(\boldsymbol{\nu})$, which exist since $\mathbf{D}(\boldsymbol{\nu})$ is strictly positive and $\mathbf{D}(\mathbf{0}) = \mathbf{0}$. Thus, under the assumptions made above, this system is input-to-state stable with respect to unmodelled disturbances $\boldsymbol{\tau}_d$ (Khalil 2000, Theorem 4.19). Equation (4.43) means that the position and velocity errors $\boldsymbol{x}$ will not converge to zero, but to an n-sphere (a sphere in a space of arbitrary dimension, 12 in this case) with radius $\left\|\boldsymbol{\tau}_d\right\| / \big(\gamma\lambda_K(\boldsymbol{\nu})\big)$ from the origin, due to the disturbances pushing the system out of equilibrium.

4.2.3 Step 3 - Adaptation and control law

Define the virtual input

$$\mathbf{Bu} = \mathbf{z} + \mathbf{Bu}_v \tag{4.44}$$

where $\mathbf{z} = \mathbf{Bu} - \mathbf{Bu}_v$ is an error variable and

$$\boldsymbol{\tau}_v = \mathbf{Bu}_v = \boldsymbol{\phi}^\top \hat{\boldsymbol{\theta}} - \hat{\boldsymbol{\tau}}_d - \tilde{\boldsymbol{\eta}}_p - \mathbf{K}_2\mathbf{s} \tag{4.45}$$

Using Equation (4.45) in (4.36) gives

$$\dot{V}_2 = -\tilde{\boldsymbol{\eta}}_p^T \mathbf{K}_1 \tilde{\boldsymbol{\eta}}_p - \mathbf{s}^T \big(\mathbf{D}(\boldsymbol{\nu}) + \mathbf{K}_2\big)\mathbf{s} + \mathbf{s}^T \big(\mathbf{z} + \boldsymbol{\phi}(\dot{\boldsymbol{\nu}}_v, \boldsymbol{\nu}_v)^T \tilde{\boldsymbol{\theta}}\big) \tag{4.46}$$

where $\tilde{\boldsymbol{\theta}} = \hat{\boldsymbol{\theta}} - \boldsymbol{\theta}$.

Assumption 4.1. *The parameters $\boldsymbol{\theta}$ of Merlin are slowly varying such that $\dot{\boldsymbol{\theta}} \approx \mathbf{0}$ and $\dot{\tilde{\boldsymbol{\theta}}} \approx \dot{\hat{\boldsymbol{\theta}}}$*

Consider the Lyapunov function candidate

$$V_3(\tilde{\boldsymbol{\eta}}_p, \mathbf{s}, \mathbf{z}, \tilde{\boldsymbol{\theta}}, t) = V_2(\tilde{\boldsymbol{\eta}}, \mathbf{s}, t) + \frac{1}{2}\mathbf{z}^\top \mathbf{z} + \frac{1}{2}\tilde{\boldsymbol{\theta}}^\top \boldsymbol{\Gamma}^{-1}\tilde{\boldsymbol{\theta}} \tag{4.47}$$

Taking the time derivative and using the actuator dynamics in Equation (3.37) gives

$$\dot{V}_3 = \dot{V}_2 + \mathbf{z}^\top \big(\mathbf{B}\dot{\mathbf{u}} - \mathbf{B}\dot{\mathbf{u}}_\mathbf{v}\big) + \tilde{\boldsymbol{\theta}}^\top \boldsymbol{\Gamma}^{-1}\dot{\hat{\boldsymbol{\theta}}} \tag{4.48}$$

$$= \dot{V}_2 + \mathbf{z}^\top \big(\mathbf{B}\mathbf{T}^{-1}(\mathbf{u}_c - \mathbf{u}) - \mathbf{B}\dot{\mathbf{u}}_\mathbf{v}\big) + \tilde{\boldsymbol{\theta}}^\top \boldsymbol{\Gamma}^{-1}\dot{\hat{\boldsymbol{\theta}}} \tag{4.49}$$

$$= -\tilde{\boldsymbol{\eta}}_p^T \mathbf{K}_1 \tilde{\boldsymbol{\eta}}_p - \mathbf{s}^T \big(\mathbf{D}(\boldsymbol{\nu}) + \mathbf{K}_2\big)\mathbf{s} + \mathbf{s}^T \big(\mathbf{z} + \boldsymbol{\phi}^\top \tilde{\boldsymbol{\theta}}\big)$$

$$\ldots + \mathbf{z}^\top \big(\mathbf{B}\mathbf{T}^{-1}(\mathbf{u}_c - \mathbf{u}) - \mathbf{B}\dot{\mathbf{u}}_\mathbf{v}\big) + \tilde{\boldsymbol{\theta}}^\top \boldsymbol{\Gamma}^{-1}\dot{\hat{\boldsymbol{\theta}}} \tag{4.50}$$

$$= -\tilde{\boldsymbol{\eta}}_p^T \mathbf{K}_1 \tilde{\boldsymbol{\eta}}_p - \mathbf{s}^T \big(\mathbf{D}(\boldsymbol{\nu}) + \mathbf{K}_2\big)\mathbf{s} + \tilde{\boldsymbol{\theta}}^\top \big(\boldsymbol{\phi}\mathbf{s} + \boldsymbol{\Gamma}^{-1}\dot{\hat{\boldsymbol{\theta}}}\big)$$

$$\ldots + \mathbf{z}^\top \big(\mathbf{s} + \mathbf{B}\mathbf{T}^{-1}(\mathbf{u}_c - \mathbf{u}) - \mathbf{B}\dot{\mathbf{u}}_\mathbf{v}\big) \tag{4.51}$$

The parameter estimate update law is chosen as

$$\dot{\hat{\boldsymbol{\theta}}} = -\boldsymbol{\Gamma}\boldsymbol{\phi}\boldsymbol{s} \tag{4.52}$$

where the adaptation gain $\boldsymbol{\Gamma}$ should have dimension 12×12. To simplify matters, one can assume that $\boldsymbol{\Gamma} = \text{diag}\{\boldsymbol{\Gamma}^*, \boldsymbol{\Gamma}^*\}$, such that the update law can be written

$$\dot{\hat{\boldsymbol{\theta}}} = -\boldsymbol{\phi}\boldsymbol{\Gamma}^*\boldsymbol{s} \tag{4.53}$$

Thus, the number of tuning parameters are reduced from 12 to 6 and the gain $\boldsymbol{\Gamma}^*$ can be understood as the adaptation gain of each degree of freedom instead of the adaptation gain for each parameter in $\hat{\boldsymbol{\theta}}$.

The control law is chosen as

$$\mathbf{u}_c = \mathbf{u} + \mathbf{T}\mathbf{B}^\dagger \big(\mathbf{B}\dot{\mathbf{u}}_v - \mathbf{s} - K_3\mathbf{z}\big) \tag{4.54}$$

where K_3 is a positive scalar. Since the thrusters have about the same response time, the diagonal matrix $\mathbf{T}$ with time constants T on the diagonal, is replaced

with the scalar value T. Equation (4.51) becomes

$$\dot{V}_3 = -\tilde{\boldsymbol{\eta}}_p^T \mathbf{K}_1 \tilde{\boldsymbol{\eta}}_p - \mathbf{s}^T \big(\mathbf{D}(\boldsymbol{\nu}) + \mathbf{K}_2\big)\mathbf{s} - K_3 \mathbf{z}^\top \mathbf{z} \tag{4.55}$$

which is only negative semidefinite in the state space $\{\tilde{\boldsymbol{\eta}}_p, \mathbf{s}, \mathbf{z}, \tilde{\boldsymbol{\theta}}\}$. The stability analysis for this system can be found in Appendix A. A a block diagram of the adaptive control law is shown in Figure 4.3.

Final control law

The control law in the original error variables is given in Equation (4.56)

$$\mathbf{u}_c = (1 - TK_3)\mathbf{u} + T\dot{\mathbf{u}}_v + TK_3\mathbf{B}^\dagger \Big(\boldsymbol{\phi}^\top \hat{\boldsymbol{\theta}} - \boldsymbol{\tau}_d - \mathbf{K}_p \tilde{\boldsymbol{\eta}}_p - \mathbf{K}_d \tilde{\boldsymbol{\nu}}\Big) \tag{4.56}$$

where $\mathbf{K}_p = 1/K_3\mathbf{K}_1 + \mathbf{K}_1\mathbf{K}_2 + \mathbf{I}$ and $\mathbf{K}_d = \mathbf{K}_2 + 1/K_3\mathbf{I}$. It is seen that the term $(1 - TK_3)$ should be positive to avoid oscillations, so therefore $K_3 \leq 1/T$. If equality is used, it is seen that the term $(1 - TK_3)\mathbf{u}$ cancel out, which means there is no need for feedback from the thrusters.

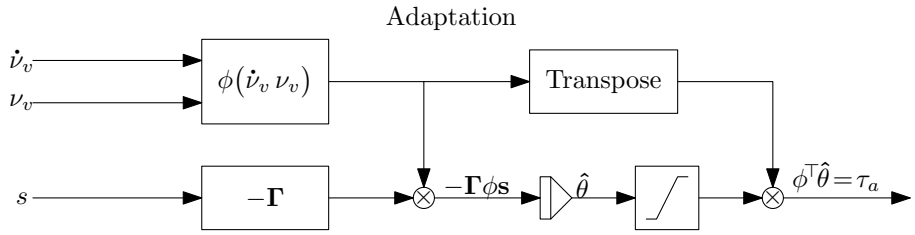

Figure 4.3: The basics of adaptation where the details of the regressor $\boldsymbol{\phi}(\cdot)$ are left out. A saturating element is introduced to keep the estimated parameters within a realistic bound.

Regressor and parameter vector

The regressor matrix and parameter vector for NCS are

$$\boldsymbol{\phi}(\dot{\boldsymbol{\nu}}_v, \boldsymbol{\nu}_v) = \left[\begin{array}{cccccc} \dot{u}_v & 0 & 0 & 0 & 0 & 0 \\ 0 & \dot{v}_v & 0 & 0 & 0 & 0 \\ 0 & 0 & \dot{w}_v & 0 & 0 & 0 \\ 0 & 0 & 0 & \dot{p}_v & 0 & 0 \\ 0 & 0 & 0 & 0 & \dot{q}_v & 0 \\ 0 & 0 & 0 & 0 & 0 & \dot{r}_v \\ \hline |u|u_v & 0 & 0 & 0 & 0 & 0 \\ 0 & |v|v_v & 0 & 0 & 0 & 0 \\ 0 & 0 & |w|w_v & 0 & 0 & 0 \\ 0 & 0 & 0 & |p|p_v & 0 & 0 \\ 0 & 0 & 0 & 0 & |q|q_v & 0 \\ 0 & 0 & 0 & 0 & 0 & |r|r_v \end{array}\right] \tag{4.57}$$

$$\hat{\boldsymbol{\theta}} = \left[\begin{array}{c} m - X_{\dot{u}} \\ m - Y_{\dot{v}} \\ m - Z_{\dot{w}} \\ I_{xx} - K_{\dot{p}} \\ I_{yy} - M_{\dot{q}} \\ I_{zz} - N_{\dot{r}} \\ \hline X_{u|u|} \\ Y_{v|v|} \\ Z_{w|w|} \\ K_{p|p|} \\ M_{q|q|} \\ N_{r|r|} \end{array}\right] \tag{4.58}$$

4.2.4 Implementation considerations

The control law (4.56) require the time derivative of (4.45), which must be available without using time derivatives of the states $\boldsymbol{\nu}, \boldsymbol{\eta}$ and $\mathbf{u}$ (T. Fossen and Berge 1997). For Merlin, only measurements of $\boldsymbol{\nu}$ and $\mathbf{u}$ are available, and $\boldsymbol{\eta}$ is estimated using the EKF developed in Knausgård (2013). The time derivative can be calculated based on (T. Fossen and Berge 1997)

$$\mathbf{B}\dot{\boldsymbol{u}}_v = \frac{\partial \mathbf{B}\mathbf{u}_v}{\partial \dot{\boldsymbol{\nu}}_v}\ddot{\boldsymbol{\nu}}_v + \frac{\partial \mathbf{B}\mathbf{u}_v}{\partial \boldsymbol{\nu}_v}\dot{\boldsymbol{\nu}}_v + \frac{\partial \mathbf{B}\mathbf{u}_v}{\partial \boldsymbol{\nu}}\dot{\boldsymbol{\nu}} + \frac{\partial \mathbf{B}\mathbf{u}_v}{\partial \tilde{\boldsymbol{\eta}}}\dot{\tilde{\boldsymbol{\eta}}} + \underbrace{\dot{\boldsymbol{\tau}}_d}_{\approx 0} \tag{4.59}$$

$$= \mathbf{M}\ddot{\boldsymbol{\nu}}_v + \Big(\mathbf{D}(\boldsymbol{\nu}) + \mathbf{K}_2\Big)\dot{\boldsymbol{\nu}}_v + \mathbf{D}^*\big(\mathrm{sgn}(\boldsymbol{\nu})\boldsymbol{\nu}_v\big)\dot{\boldsymbol{\nu}} + \dot{\tilde{\boldsymbol{\eta}}}_p \tag{4.60}$$

where $\mathbf{D}^*(\cdot)$ is equal to $\mathbf{D}(\cdot)$ but does not take the absolute value of its argument. The disturbances are assumed to be slowly varying. During station keeping, where the desired velocity and acceleration $\dot{\boldsymbol{\nu}}_d, \ddot{\boldsymbol{\nu}}_d$ are zero, one may simplify according to:

$$\ddot{\boldsymbol{\nu}}_v = \ddot{\boldsymbol{\nu}}_d + \mathbf{K}_1\dot{\boldsymbol{\nu}}_d - \mathbf{K}_1\mathbf{M}^{-1}\Big(\boldsymbol{\tau} - \mathbf{D}(\boldsymbol{\nu})\boldsymbol{\nu}\Big) \tag{4.61}$$

$$\approx \mathbf{K}_1\mathbf{M}^{-1}\Big(\boldsymbol{\tau} - \mathbf{D}(\boldsymbol{\nu})\boldsymbol{\nu}\Big) \tag{4.62}$$

such that

$$\mathbf{M}\ddot{\boldsymbol{\nu}}_v \approx -\mathbf{K}_1\Big(\boldsymbol{\tau} - \mathbf{D}(\boldsymbol{\nu})\boldsymbol{\nu}\Big) \tag{4.63}$$

where it is assumed that $\mathbf{M}\mathbf{K}_\mathbf{1}\mathbf{M}^{-1} \approx \mathbf{K}_1$ so that the inverse of the (unknown) inertia matrix is avoided. This is in general not mathematically correct, but work if the diagonal elements of the inertia matrix are dominating. From Equation (3.21) it is seen that the largest off-diagonal element is about 6 percent of the smallest diagonal element, such that Equation 4.63 makes a valid approximation.

4.3 Saturation

A saturating element is introduced in Figure 4.2 and 4.3 to limit the integral action of the disturbance observer and adaptation. The limit should be below the maximum available thrust, e.g. 70 %, to prevent spending all of the available input on integral action.

4.4 Velocity Control

The control system developed above is based on position measurements and controls both position and velocity. In this thesis, velocity control is used in low-speed maneuvering with joystick and in path following, by tracking desired velocities in the horizontal plane. The remaining DOFs should still be governed by position control. The approach taken here is to use one controller which can be set to position or velocity mode for any DOF. This will make for a simple implementation and yield a compact system.

To enable velocity control for *any* DOF, one may require the position error $\tilde{\eta}_i$ to be zero for that DOF. This is achieved by output tracking the actual position,

i.e. $\eta_{d,i} \equiv \eta_i$, as will be shown by deriving the velocity controller in a way similar to the DP controller.

The velocity error is defined as $\tilde{\boldsymbol{\nu}} = \boldsymbol{\nu} - \boldsymbol{\nu}_d$. Consider the Lyapunov function candidate

$$V_1^*(\tilde{\boldsymbol{\nu}}, t) = \frac{1}{2}\tilde{\boldsymbol{\nu}}^\top \mathbf{M}\tilde{\boldsymbol{\nu}} \tag{4.64}$$

The time derivative is

$$\begin{aligned}
\dot{V}_1^* &= \tilde{\boldsymbol{\nu}}^\top \big(-\mathbf{D}(\boldsymbol{\nu})\boldsymbol{\nu} - \mathbf{M}\dot{\boldsymbol{\nu}}_d + \mathbf{B}\mathbf{u} + \boldsymbol{\tau}_d \big) && (4.65)\\
&= \tilde{\boldsymbol{\nu}}^\top \big(-\mathbf{D}(\boldsymbol{\nu})\boldsymbol{\nu}_d - \mathbf{D}(\boldsymbol{\nu})\tilde{\boldsymbol{\nu}} - \mathbf{M}\dot{\boldsymbol{\nu}}_d + \mathbf{B}\mathbf{u} + \boldsymbol{\tau}_d \big) && (4.66)\\
&= -\tilde{\boldsymbol{\nu}}^\top \mathbf{D}(\boldsymbol{\nu})\tilde{\boldsymbol{\nu}} + \tilde{\boldsymbol{\nu}}^\top \big(\mathbf{B}\mathbf{u} - \boldsymbol{\phi}(\dot{\boldsymbol{\nu}}_d, \boldsymbol{\nu}_d, \boldsymbol{\nu})^\top \hat{\boldsymbol{\theta}} + \boldsymbol{\tau}_d \big) && (4.67)
\end{aligned}$$

Note that if $\tilde{\boldsymbol{\eta}}_p = \mathbf{0}$ then the expression for the virtual velocity $\boldsymbol{\nu}_v$ becomes

$$\boldsymbol{\nu}_v = \boldsymbol{\nu}_d - \mathbf{K}_1\tilde{\boldsymbol{\eta}}_p \equiv \boldsymbol{\nu}_d \tag{4.68}$$

Thus, $\mathbf{s} = \boldsymbol{\nu} - \boldsymbol{\nu}_v = \boldsymbol{\nu} - \boldsymbol{\nu}_d = \tilde{\boldsymbol{\nu}}$. In other words, by carrying out the same steps as in Section 4.2 one will arrive at the control law

$$\mathbf{u}_c = (1 - TK_3)\mathbf{u} + T\dot{\mathbf{u}}_v + TK_3\mathbf{B}^\dagger \Big(\boldsymbol{\phi}^\top \hat{\boldsymbol{\theta}} - \boldsymbol{\tau}_d - \mathbf{K}_d\tilde{\boldsymbol{\nu}} \Big) \tag{4.69}$$

which is equal to (4.56) with $\tilde{\boldsymbol{\eta}}_p = \mathbf{0}$. Thus, velocity control can be enabled for any DOF by output tracking the position for that DOF. This works because the controller is decoupled by having diagonal gain matrices $\mathbf{K}_1, \mathbf{K}_2$ and a block diagonal structure in the regressor $\boldsymbol{\phi}$.

4.5 Initialization

The use case for the station keeping system, is that a pilot positions the ROV manually and activates the automatic system using the HMI. It is important that the transfer from manual to automatic mode is made as smooth as possible. For instance, there might be current in the water and the pilot will manually stabilize the ROV before activating station keeping. This means it is known in advance how much thrust is needed to stabilize, so there is no need to let the controller start from scratch. This can be done by manipulating Equation (4.45):

$$\begin{aligned}
\boldsymbol{\tau}_v(0) &\approx -\hat{\boldsymbol{\tau}}(0)_d - \mathbf{K}_2\mathbf{s}(0) && (4.70)\\
&\Downarrow && (4.71)\\
\mathbf{x}_{dob}(0) &= -\boldsymbol{\tau}_v(0) - \mathbf{K}_2\mathbf{s}(0) - \mathbf{K}_{dob}\boldsymbol{\nu}(0) && (4.72)
\end{aligned}$$

where

$$\boldsymbol{\tau}_v(0) = k_{thr}\mathbf{B}\begin{bmatrix}|f_1|f_1\\ \vdots \\ |f_8|f_8\end{bmatrix} \tag{4.73}$$

and f_i are the frequencies sent to the converts when switching to automatic mode. The adaptive controller is always restarted from zero. An important implementation aspect in this regard is to deactivate the joystick by default when entering automatic mode. This prevents the joystick signals from entering the control loop when station keeping should be the active mode. A semi-automatic option is available which lets the pilot dynamically position the ROV.

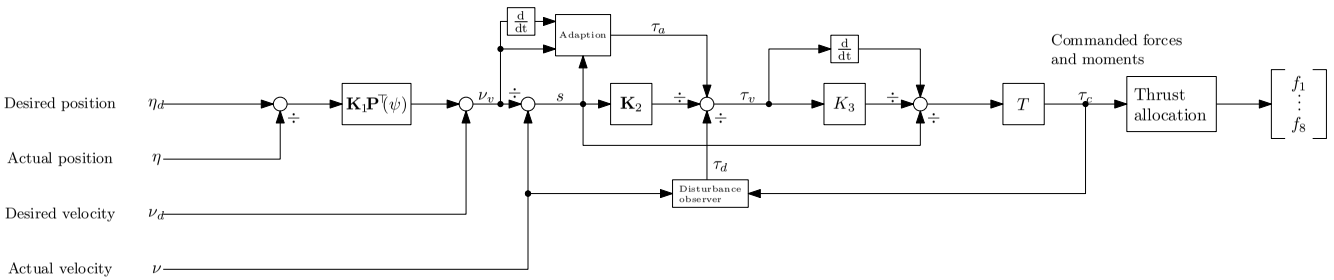

Figure 4.4: Overview of the developed control system using adaptation and disturbance observer for integral action.

Chapter 5

Guidance

Methods of guiding Merlin WR200 is considered in this chapter, including trajectory tracking and an algorithm for path following based on waypoints.

5.1 Joystick in closed-loop control

A joystick lets the pilot maneuver the ROV while the control system compensates for environmental loads, illustrated in Figure 5.1. The goal is to let the pilot position the ROV with ease even in the presence of e.g. currents. Knausgård (2013) and Dukan (2014) consider a second order velocity reference model as in Equation (5.1) for filtering raw joystick inputs.

$$\ddot{\boldsymbol{\nu}}_d + 2\Delta\Omega\dot{\boldsymbol{\nu}}_d + \Omega^2\boldsymbol{\nu}_d = \Omega^2\boldsymbol{\nu}^j \tag{5.1}$$

After sea trials, both theses conclude that controlling thrust directly is the preferred option due to slow response when using the reference model (5.1). Dukan (2014) points to the model causing significant delay, such that the pilot may experience slow response and not being in control. One may argue that a drawback of manually controlling a subset of the DOFs (i.e. direct thrust) by bypassing the controller, is the need to properly handle the transition back to automatic mode. This involves proper initialization of the integrators to avoid drift and unwanted transient behavior.

To ensure stability and predictability, a joystick velocity reference model is still pursued in this thesis. A new model is suggested using only a first order low

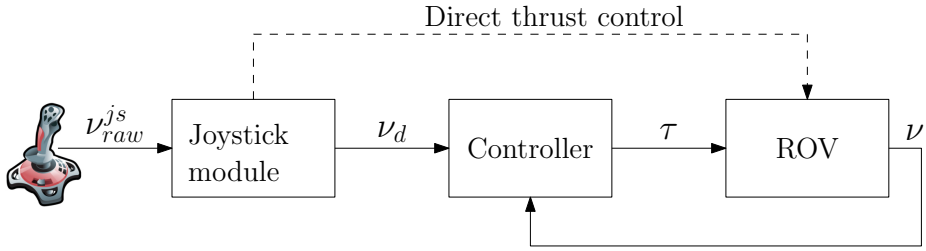

Figure 5.1: Joystick in closed-loop control. One may also use the joystick to control thrust directly by bypassing the controller, but this is not used in this thesis

pass filter to reduce phase lag, but at the cost of not having a filtered reference acceleration input to the controller.

Moreover, a state machine is suggested to monitor each axis of the joystick with the states given below (Fig. 5.2). Each state machine include a variable `active_bit` used by the reference model to determine if the joystick signal for that axis should be considered.

Inactive The stick position is within the upper and lower limit and is not in use. `active_bit` is set to 0.

Active The stick position is outside the upper and lower limit and is being used. `active_bit` is set to 1.

Passive The stick has been active and is now within the upper and lower limit. If left in this state for some time, the state is considered inactive. `active_bit` is left unchanged in this state.

The passive state allows for the stick to safely pass through the origin. For the pilot it means he can provide both positive and negative inputs with ease.

5.1.1 Raw joystick signal

The raw joystick value $\nu^{js}_{\text{raw}} \in [-\nu^{js}_{max}, \nu^{js}_{max}]$ is transformed to a quadratic mapping to ensure better control of fine precision inputs. In addition, the raw signal is filtered using a first order low pass filter for smooth inputs (Fig. 5.3).

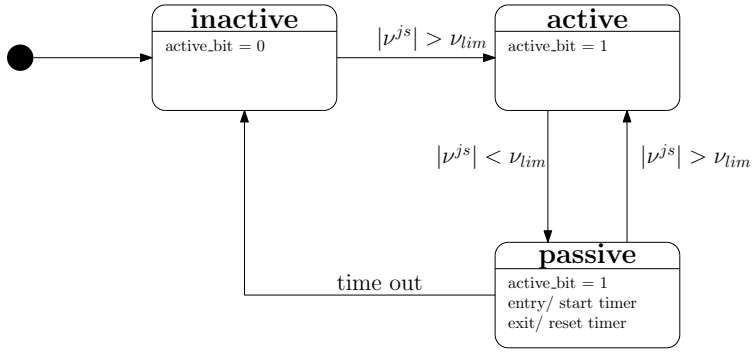

Figure 5.2: A state machine is used to monitor each axis of the joystick. This allows for better detection of an active stick, and allows for dead band limits and a timer to determine when a stick has become inactive after operation.

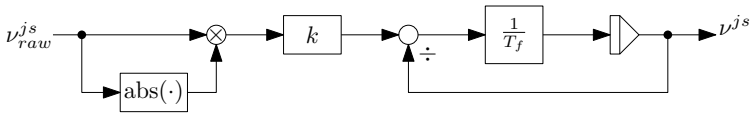

Figure 5.3: Quadratic mapping and low-pass filtering of raw joystick signal. The output is used in the joystick velocity reference model for low-speed maneuvering.

5.1.2 Surge, sway and heading

Pushing the joystick forward or sideways will produce desired velocities forward or sideways relative to the ROV, but the controller does not consider the actual position in the direction of travel. For instance, if a forward command is given, sideways motion is still under position control while only speed control is enabled for forward motion. Speed control is achieved by means of output-tracking the forward position, which is calculated by rotating the North and East position to the body-fixed frame. The desired forward position is updated in the body-fixed frame and rotated back to the NED frame for output tracking in NED. This is illustrated in Figure 5.4.

When the stick is inactive, the desired velocity is set to zero and once the velocity is sufficiently low, position control is activated to lock on the current position. The same strategy for surge and sway is taken for controlling heading except position control is enabled directly after releasing the stick. This is best illustrated by the pseudo-code in Algorithm (5.1) showing how the reference model work for surge motions.

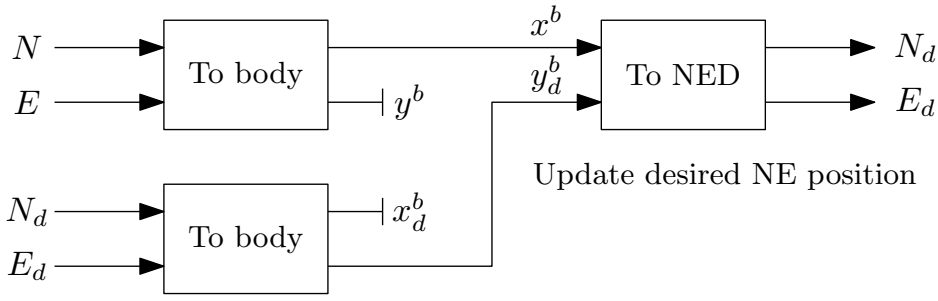

Figure 5.4: Desired North and East positions are updated to allow for motions in body the surge direction, when pushing the joystick forward

Algorithm 5.1 Pseudo-code for the joystick velocity reference model in surge. A desired velocity is computed from the filtered joystick signal. The desired forward position is updated in the body-fixed frame and transformed to the NED frame for output tracking in NED. The same principles are applied to sway and heading.

if active_bit **then**
  $u_d = u_{js}$
  $x_d = x_{rov}$
else if $|u| > u_{lim}$ **and** $t < t_{lim}$ **then**
  $u_d = 0$
  $x_d = x_{rov}$
  update timer t
else
  $u_d = 0$
  reset timer t
end if

5.1.3 Depth

A different approach is taken for depth control. A desired depth is found by integrating the desired heave velocity. Measures are taken to avoid having the desired depth lagging behind the direction of travel and to also ensure it is not too far ahead (Algorithm 5.2).

Algorithm 5.2 Pseudo-code for the joystick velocity reference model in heave. The desired heave velocity is computed from the filtered joystick signal, and a desired depth from integration of this value. Saturation is used to ensure that the desired depth is not lagging behind or lies to far ahead of the ROV.

```
if active_bit then
    z_d = D + h w_d k_1
    if z_d < D and w_d > 0 then
        z_d = D + k_2
    else if z_d > D and w_d < 0 then
        z_d = D − k_2
    end if
    z_d = max(D − k_3, min(D + k_3, z_d))
else
    z_d = D
    w_d = 0
end if
```

5.2 Reference models

5.2.1 Constant jerk reference model

The continuous equation for the constant jerk reference model found in Dukan (2014) is presented next. A constant jerk is switched on and off according to Equation (5.2) (Fig. 5.5)

$$\delta(t) = \begin{cases} 1 & \text{if } t_0 < t < t_1, \\ 0 & \text{if } t_1 \leq t < t_2, \\ -1 & \text{if } t_2 \leq t < t_3, \\ 0 & \text{if } t_3 \leq t < t_4, \\ -1 & \text{if } t_4 \leq t < t_5, \\ 0 & \text{if } t_5 \leq t < t_6, \\ 1 & \text{if } t_6 \leq t < t_7 \end{cases} \tag{5.2}$$

A move from A to B can be separated into 3 main stages: acceleration $\langle t_0, t_3 \rangle$, cruise $\langle t_3, t_4 \rangle$ and deceleration $\langle t_5, t_7 \rangle$. The ROV moves at a constant speed towards the target in the cruise stage while the acceleration and deceleration stages can be made symmetrical. The jerk, acceleration, velocity and position

are then found in continuous time as

$$j(t) = j_c\delta(t) \tag{5.3}$$

$$a(t) = \int_{t_0}^{t} j(\tau)\ \mathrm{d}\tau + a_0 = jt + a_0 \tag{5.4}$$

$$v(t) = \int_{t_0}^{t} a(\tau)\ \mathrm{d}\tau + v_0 = \frac{1}{2}jt^2 + a_0 t + v_0 \tag{5.5}$$

$$p(t) = \int_{t_0}^{t} v(\tau)\ \mathrm{d}\tau + p_0 = \frac{1}{6}jt^3 + \frac{1}{2}at^2 + v_0 t + p_0 \tag{5.6}$$

Given the constant jerk j_c, desired distance d_{ref} and the maximum acceleration and velocity, a solution to the (symmetrical) switching times are given by

$$\begin{aligned} t_1 &= a_{max}/j_c \\ t_2 &= v_{max}/a_{max} \\ t_3 &= t_2 + t_1 \\ t_4 &= d_{ref}/v_{max} \\ t_5 &= t_1 + t_4 \\ t_6 &= t_2 - t_1 + t_5 \\ t_7 &= t_1 + t_6 \end{aligned} \tag{5.7}$$

Feasible parameters

A feasible solution is found when the time instants (5.7) appear in ascending order. This is ensured by an algorithm that adjust the velocity and acceleration until a valid solution is found.

Discrete-time considerations

The continuous switching times in Equation (5.7) may be in between the time steps of the control system which runs at either 5 Hz or 10 Hz in this thesis. To obtain a finer time scale, the reference model is run N steps forward in time at each iteration, where $N = h/h_{\text{fast}}$ and h is the sampling period of the controller. $N = 250$ is chosen in this thesis for $h = 0.2$ seconds. In other words, the reference model is "sampled" at the rate $h_{\text{fast}} = h/N$ and the final values are output to the controller.

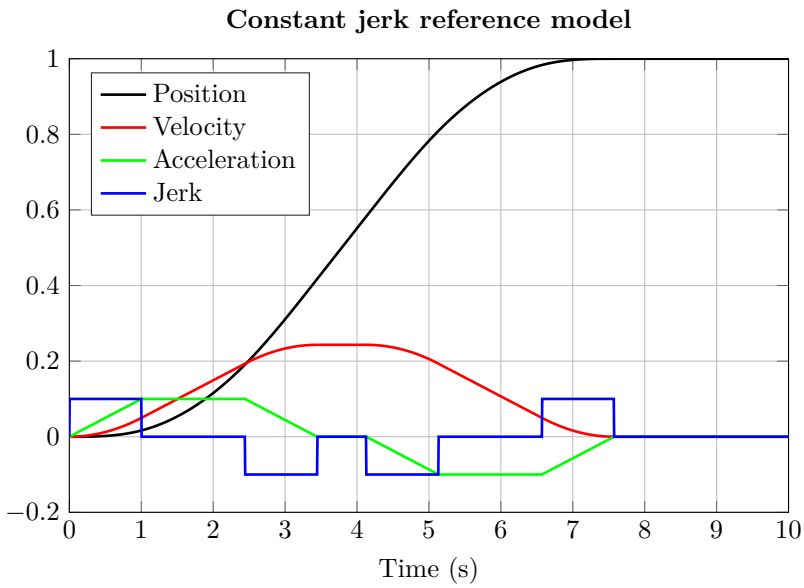

Figure 5.5: Desired position, velocity, acceleration and jerk in the path fixed frame using the constant jerk reference model

5.2.2 Filter-based reference model

Since the constant jerk reference model only works for fixed inputs, a filter-based reference model is also suggested for the guidance system. The filter-based model may be used for small adjustments or in situations where the reference is not fixed. From Thor I. Fossen (2011), a third order model is suggested

$$p_{d_i}^{(3)} + (2\zeta_i + 1)\omega_i \ddot{p}_{d_i} + (2\zeta_i + 1)\omega_i^2 \dot{p}_{d_i} + \omega_i^3 p_{d_i} = \omega_i^3 r_i \tag{5.8}$$

for $i = 1 \ldots 6$. Critical damping is obtained with $\zeta_i = 1$. The response of the model may be tuned through the natural frequency ω_i. For roll, pitch and heave, one may use the expected natural periods from Section 3.4.1 in Chapter 3 as a starting point.

5.3 Line-of-sight guidance

The LOS guidance law considered in this thesis is based on the two-dimensional steering law found in Thor I. Fossen (2011, p. 257) and the modifications for

fully actuated vehicles found in Dukan (2014). Ohrem (2015) also considered the two-dimensional steering law for fully actuated vehicles, by applying it to Merlin WR200 in a setting where the vehicle had to reverse the already driven path. To do so, some calculations in the LOS algorithm had to be modified. The modifications can be avoided by applying the LOS law to direct the velocity vector instead of the course angle, as done in Dukan (2014) and restated below. Since Merlin WR200 is fully actuated, one can control the heading angle independent of direction of travel. This enables several modes of operation, including reversing an already driven path. Moreover, LOS guidance is only considered in the two-dimensional case where depth is controlled to a constant value.

5.3.1 Algorithm

Let two waypoints $\mathbf{p}_k^n = [x_k,\ y_k]^\top$ and $\mathbf{p}_{k+1}^n = [x_{k+1},\ y_{k+1}]^\top$ define a horizontal straight-line path in the NED frame (Fig. 5.6). The path-fixed frame centered at $\mathbf{p}_k^n$, is obtained by rotating the NED frame an angle α_k given by

$$\alpha_k = \text{atan2}(y_{k+1} - y_k,\ x_{k+1} - x_k) \tag{5.9}$$

relative to the North-axis, and atan2 is the four-quadrant version of $\arctan(y/x) \in [-\pi/2,\ \pi/2]$. The position $\mathbf{p}^n(t) = [x(t),\ y(t)]^\top$ of the ROV in the path-fixed frame is then given by

$$\boldsymbol{\epsilon}(t) = \begin{bmatrix} s(t) \\ e(t) \end{bmatrix} = \mathbf{R}_z(\alpha_k)^\top (\mathbf{p}^n(t) - \mathbf{p}_{k+1}^n) \tag{5.10}$$

where

$$\mathbf{R}_z(\alpha_k) = \begin{bmatrix} \cos(\alpha_k) & -\sin(\alpha_k) \\ \sin(\alpha_k) & \cos(\alpha_k) \end{bmatrix} \tag{5.11}$$

is the rotation matrix between NED and the path frame, and

$$s(t) = [x(t) - x_k]\cos(\alpha_k) + [y(t) - y_k]\sin(\alpha_k) \tag{5.12}$$

$$e(t) = -[x(t) - x_k]\sin(\alpha_k) + [y(t) - y_k]\cos(\alpha_k) \tag{5.13}$$

$$\tag{5.14}$$

are the along-track distance and the cross-track error, respectively.

The path-tangential angle $\chi_p(e)$ is defined as

$$\chi_p(e) = \arctan(-e,\ \Delta) \tag{5.15}$$

where $\Delta > 0$ is the lookahead distance. The desired direction of the velocity vector is found from the desired course angle defined in Equation (5.16).

$$\chi_d = \alpha_k + \chi_p \tag{5.16}$$

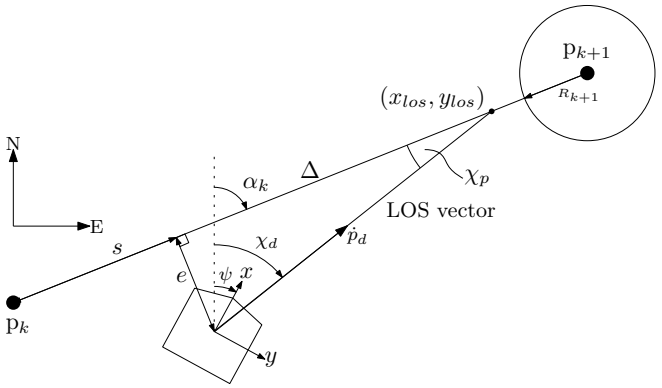

Figure 5.6: Two-dimensional LOS guidance principle applied to a fully actuated vehicle. The desired velocity is found from the LOS vector, leaving heading to be controlled independently. Image courtesy of Dukan (2014).

The desired velocity $\dot{\mathbf{p}}_d^n$ of the ROV in the NED frame is given by the desired course angle χ_d and a desired speed U_d according to

$$\dot{\mathbf{p}}_d^n = \mathbf{R}_z(\chi_d) \begin{bmatrix} 1 \\ 0 \end{bmatrix} U_d \tag{5.17}$$

The kinematic relationship between velocity in the NED frame and the body-fixed frame is given by Equation 5.18 (see Chapter 3, Section 3.2.1)

$$\dot{\mathbf{p}}_d^n = \mathbf{R}_b^n(\Theta_{nb})\mathbf{v}_d \tag{5.18}$$

Thus, the desired velocity vector in the body-fixed frame is found by inverting the kinematic equation (5.18) and inserting Equation (5.17)

$$\mathbf{v}_d^b = \begin{bmatrix} u_d \\ v_d \end{bmatrix} = \mathbf{R}_b^n(\Theta_{nb})^\top \mathbf{R}_z(\chi_d) \begin{bmatrix} 1 \\ 0 \end{bmatrix} U_d \tag{5.19}$$

One may choose the desired speed U_d as the output of a velocity reference model or via a control available to the pilot, for example. The former option is applied in this thesis.

5.3.2 Switching waypoint

Thor I. Fossen (2011) propose to switch waypoint when the vehicle is either within a circle of acceptance

$$[x_{k+1} - x(t)]^2 + [y_{k+1} - y(t)]^2 \leq R_{k+1}^2 \tag{5.20}$$

with radius R_{k+1} around waypoint $\mathbf{p}_{k+1}^n$, or when the covered along-track distance $s(t)$ is sufficiently close to the total length s_{k+1} between waypoints $\mathbf{p}_{k+1}^n$ and $\mathbf{p}_k^n$

$$s(t) \geq s_{k+1} - R_{k+1} \tag{5.21}$$

The former strategy should be used if it is important to pass through each waypoint, whereas the latter should be used when the waypoints simply define a path (Thor I. Fossen 2011).

Chapter 6

Simulation

6.1 ROV Simulator

IKM Subsea Solutions AS facilitates a high-fidelity simulator for training ROV pilots. The simulator is powered by the industry leading Vortex Dynamics engine[1] and combined with the control systems and equipment produced by IKM Subsea Solutions AS. This gives a realistic rendering of hydrodynamics, propulsion systems, tether, manipulators and sensors (IKM Subsea 2015), and has proven to be a valuable tool for developing control systems.

Several issues regarding time delay, coordinate frames and thruster numbering, were mentioned in Ohrem (2015), leading to valuable time being spent on troubleshooting. With this in mind, some steps were taken before starting to work on the control system

- Identify the time delay
- Verify coordinate frame
- Verify thruster numbering
- Verify direction of thrust

Using Wireshark[2], it was possible to trace the network communication between the computer running Matlab[3] with the control system, and the simulator. It

[1] http://www.cm-labs.com/
[2] https://www.wireshark.org/
[3] http://se.mathworks.com/

was found that UDP packets sent from the Matlab computer spent about 1-2 seconds reaching the simulator, supporting the observations made in Ohrem (2015). Thanks to the supervisor at IKM Subsea Solutions, the one-way communication delay was reduced to about 210-380 ms, as shown in Figure 6.1. By flying the ROV at full speed and counting the number of times the same data was received from the simulator, a measure of the refresh rate could be made. Figure 6.2 shows that the average is about 0.2 seconds or 5 Hz, which was chosen as the sample rate of the controller in Matlab. Note that this is half the speed of the implementation in the PLC which runs at 10 Hz.

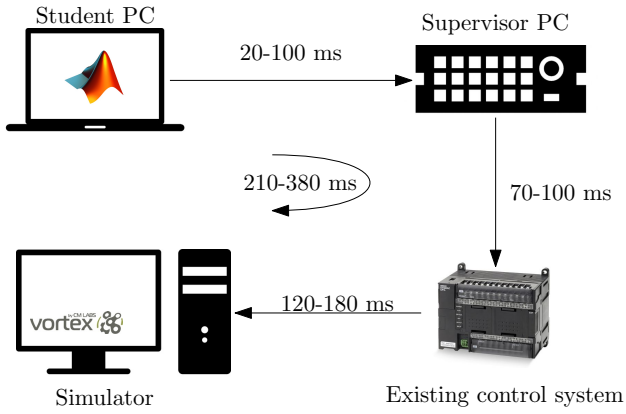

Figure 6.1: Simulator setup when prototyping the control system in Matlab. A rather large delay is experienced by the student PC as data must travel through several nodes along the way.

6.1.1 Available measurements

The Cartesian position coordinates in the simulator adhere to a North-West-Up frame, whereas roll, pitch and yaw are defined according to North-East-Down frame. Transforming the position measurement to NED is done according to

Equation (6.1).

$$\mathbf{p}^n = \begin{bmatrix} N \\ E \\ D \end{bmatrix} = \begin{bmatrix} x \\ -y \\ -z \end{bmatrix} \tag{6.1}$$

where $[x,\ y,\ z]^\top$ are the Cartesian coordinates of the ROV in the simulator.

At present time, the simulator can only provide position measurements. One may estimate the velocity using a Kalman filter or nonlinear passive observer (see e.g. Thor I. Fossen 2000; Steinke and B. J. Buckham 2005; Dukan, Ludvigsen, and Asgeir J. Sørensen 2011; Candeloro et al. 2012), however the simplest solution, is to calculate the velocity by numerically differentiating the noiseless position measurements and using a low-pass filter. The result contains noise which can be traced back to the update rate of the control system being to fast, i.e. using the same position measurement in two consecutive iterations. This proved not to be a problem in simulations. The low-pass filter was tuned to provide as much smoothing as possible without introducing too much delay, which can destabilize the system.

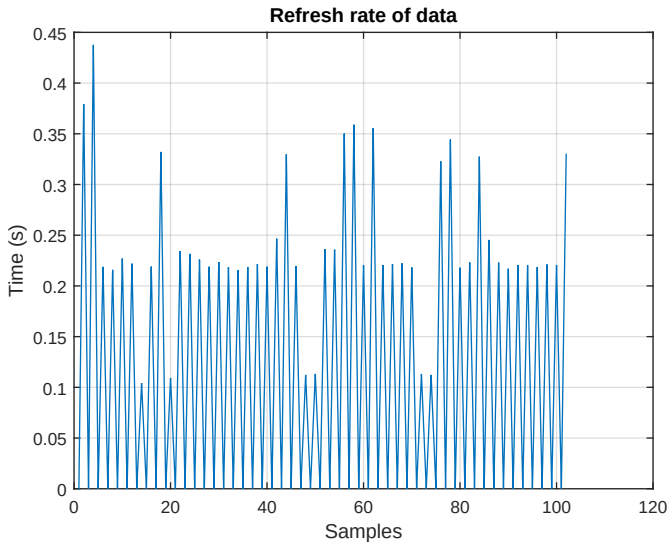

Figure 6.2: Counting the number of times the same data is received in Matlab gives an estimate of the refresh rate. New data seem to arrive every 0.2 seconds, indicating that the sampling rate should be 5 Hz or slower.

6.2 Implementation

6.2.1 Matlab

The developed control system was implemented in Matlab for quick prototyping. Using this software, one can easily add new functionality, which speeds up the development process. The cost of this setup is a rather large communication delay with the simulator, which in general can be destabilizing in control systems. The new control law, reference models and waypoint guidance system was all implemented using object-oriented-programming in Matlab. A brief overview is given in Appendix C.

6.2.2 Hardware-in-the-loop

The control law and joystick reference model for low speed maneuvering was implemented on an Omron PLC, which communicate with the simulator through the existing control system (Fig. 6.3). When the control system is running on a PLC, the communication delay is reduced to about 140-210 milliseconds, almost twice as fast as when using the student PC running Matlab. The sampling rate of the controller is 10 Hz, which will also be the sampling rate in the field to match the rate of the navigation system. The delay between the PLCs is not a communication delay, but the scan-time of the existing control system, which is approximately 20-30 ms.

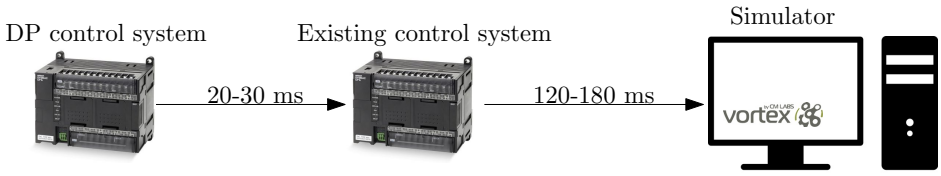

Figure 6.3: The main components of the HIL-setup. The developed controller is implemented in a PLC that communicates with the existing control system of Merlin WR200. This is done to avoid altering code in the existing controller in the development phase.

6.2.3 Numerical integration method

This thesis use forward Euler integration method for numerical integration in the disturbance observer and parameter estimate update law.

$$x_{k+1} = x_k + hf\big(x_k, u_k, t_k\big) \tag{6.2}$$

where h is the sampling period and k the discrete time variable.

6.2.4 Numerical differentiation method

Using the forward Euler method in Equation (6.2), the derivate can be approximated as

$$\dot{x}(t) \approx \frac{x_{k+1} - x_k}{h} = \mathrm{d}x_k \tag{6.3}$$

In addition a first order low pass filter is used filter out noise from the differentiation process

$$y_{k+1} = (1 - \alpha)y_k + \alpha \mathrm{d}x_k \tag{6.4}$$

with $\alpha = h/T_f$.

6.2.5 Heading discontinuity

Special considerations are taken for the heading angle due to the discontinuity when crossing 360 degrees. If the heading at time k is 5 degrees, but the previous value was 350 degrees, the ROV most likeley turned a distance of 15 degrees over the discontinuity and not -345 degrees in the opposite direction. This is corrected in the following algorithm which is also used when calculating the heading error in the controller.

Algorithm 6.1 Algorithm for handling heading discontinuity around 0/360 degrees.

Require: $\Delta_\psi = \psi(k) - \psi(k-1)$ or $\Delta_\psi = \psi - \psi_d$
  if $\Delta_\psi \leq -\pi$ **then**
    $\Delta_\psi = \Delta_\psi + 2\pi$
  else if $\Delta_\psi > \pi$ **then**
    $\Delta_\psi = \Delta_\psi - 2\pi$
  end if

Chapter 7

Simulation Results

This chapter presents results retrieved using the high-fidelity simulator at IKM, Bryne. The new control system (NCS) is compared to the original PCABS controller and its extension PCABS-D, in three scenarios. Results also include waypoint tracking in 2D, joystick maneuvering in strong current, and a stress test pushing the new controller to the limit. A discussion of the results can be found at the end of this chapter.

7.1 Performance Evaluation

Merlin WR200 operates in 6 DOF and output 6 positions to be evaluated. Comparing the controllers by only inspecting figures, may lead to subjective results and may fail to give an overall performance measure. Thus, it is convenient with automated tools for measuring and comparing the performance of the control systems, aiding the inspection of graphs and figures. To this end, 3 measures will be used: Integrated Absolute value of Error (IAE) of the position errors, Root Mean Square (RMS) of the position errors and the Mean of absolute value of rate of change of the input (MADU). IAE is also known as the $\mathcal{L}_1$ norm, and RMS as a scaled $\mathcal{L}_2$ norm. The discrete implementation used in this thesis are given by Equations (7.1), (7.2) and (7.3).

$$\text{IAE} = \sum_{k=1}^{N} |e(k)| \tag{7.1}$$

$$\text{RMS} = \sqrt{\frac{\sum_{k=1}^{N} e(k)^2}{N}} \tag{7.2}$$

$$\text{MADU} = \frac{1}{N} \sum_{k=1}^{N} |u(k+1) - u(k)| \tag{7.3}$$

Since MADU is calculated individually for the 8 thrusters, it is seen as more convenient to average the measure to obtain one number describing the thruster usage. This will be referred to as Mean of MADU (MMADU) and gives an overall average of the rate of change of the input, which is important with respect to power consumption and wear and tear of the thrusters. A lower value is considered better when using the measures given above.

IAE and RMS are applied to the 6 position errors $\tilde{\boldsymbol{\eta}} = [\tilde{N},\ \tilde{E},\ \tilde{D},\ \tilde{\phi},\ \tilde{\theta},\ \tilde{\psi}]\top$. Based on IAE and RMS, a comparison is made by assigning points based on the lowest values which are weighed according to Table 7.1. The best scoring controller receives 1 point, the second best 2 points and the third best 3 points. The idea of "lower is better" still apply. The scores are normalized by dividing each row with the largest score in that row. Roll and pitch are weighed less as these DOFs are not as crucial as the other 4 during DP and station keeping.

Table 7.1: Each DOF is weighed when comparing IAE and RMS. Roll and pitch are given a lower weight as they are not crucial to station keeping considering the ROV is naturally stable in these DOFs.

$\tilde{N}$	$\tilde{E}$	$\tilde{D}$	$\tilde{\phi}$	$\tilde{\theta}$	$\tilde{\psi}$
1	1	1	0.5	0.5	1

7.2 Comparing the controllers

This section gives the results of comparing the PCABS, PCABS-D and NCS controllers. The motivation for these tests is to document if an increase in performance can be traced back to an increase in complexity or additional modeling in the control system. To this end, three scenarios A-C are considered:

Scenario A Station keeping for 100 seconds

Scenario B After A, move horizontally to a new position

Scenario C After A, rotate 90 degrees and maintain initial position.

A current of 1.5 knots (≈ 0.77 m/s) with bearing 59° is turned on after approximately 5 seconds. The initial depth is 140 meters and the tether length is 20 meters. Both tethering out and turning on the current are done manually, but carried out in a structured manner to ensure similar initial conditions. The ROV is initially heading due East and the current is attacking the ROV from starboard side, pushing it both forward and sideways.

In Scenario B and C, the filter-based reference model of Section 5.2.2 in Chapter 5, is applied with the parameters in Table 7.2. The natural frequencies ω_i are chosen rather conservatively in these simulations, yielding slow motions. Both PCABS and PCABS-D use the exact same gains whereas NCS use a smaller heave velocity error gain, and larger DOB and adaptation gains (Table 7.3 and 7.4). These tests are run in Matlab according to the connection topology in Figure 6.1 in Chapter 6.

Table 7.2: Reference model parameters used in Scenario B and C.

DOF	Natural frequency ω (rad/s)	Relative damping ζ
Surge	0.09	1
Sway	0.09	1
Heave	1.0	1
Roll	1.0	1
Pitch	1.0	1
Yaw	0.1	1

Table 7.3: Controller gains for PCABS and PCABS-D.

Parameter	Value
$\mathbf{K}_1$	diag(0.1, 0.1, 0.1, 0.09, 0.09, 0.2)
$\mathbf{K}_2$	diag(4400, 4400, 7000, 4000, 4000, 9500)
$\mathbf{K}_{dob}$	diag(300, 300, 300, 100, 100, 10)
$\mathbf{\Gamma}$	diag(500, 500, 500, 500, 500, 200)

Table 7.4: Controller gains for NCS.

Parameter	Value
$\mathbf{K}_1$	diag(0.1, 0.1, 0.1, 0.09, 0.09, 0.2)
$\mathbf{K}_2$	diag(4400, 4400, 5000, 4000, 4000, 9500)
K_3	$1/1.2 \approx 0.833$
$\mathbf{K}_{dob}$	diag(1000, 1000, 1000, 1000, 1000, 1000)
$\mathbf{\Gamma}$	diag(1000, 1000, 1500, 1500, 1500, 1000)

7.2.1 Scenario A: Station keeping

The ROV should maintain the position and heading for 100 seconds (Fig. 7.1). As mentioned above, the current is turned on after approximately 5 seconds, which gives a rather large step in the disturbance. The major difficulty is to suppress the disturbance and get back into position. A comparison is provided in Figure 7.2 along with position and attitude errors in Figures 7.3a and 7.3b. Supplementary information is found in Appendix B.

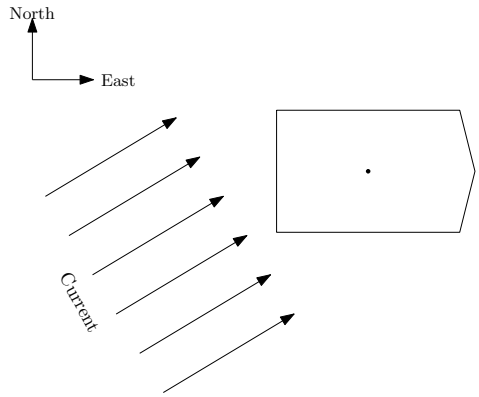

Figure 7.1: Simulation Scenario A. The objective is station keeping with current speed 1.5 knots.

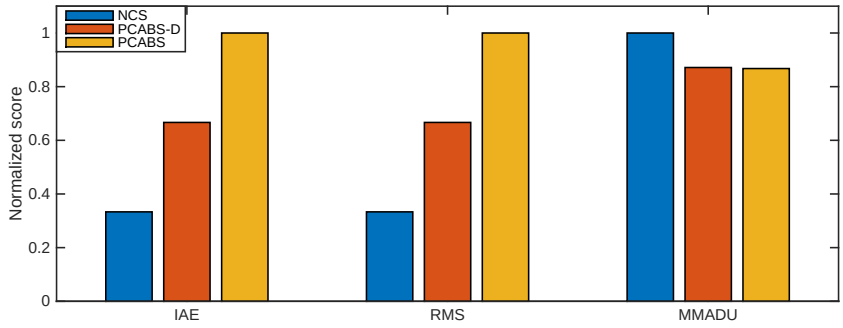

Figure 7.2: Scenario A. The new control system (NCS) score better than PCABS and PCABS-D in terms of keeping errors small, but use more thrust. A disturbance observer enables PCABS-D to reject disturbances more efficiently than PCABS, by using about the same amount of thrust.

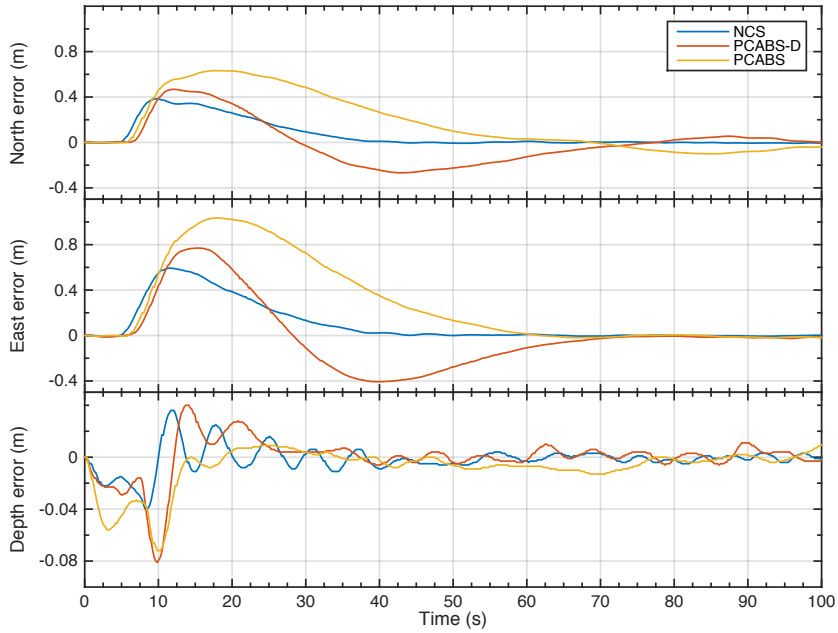

(a) Position errors

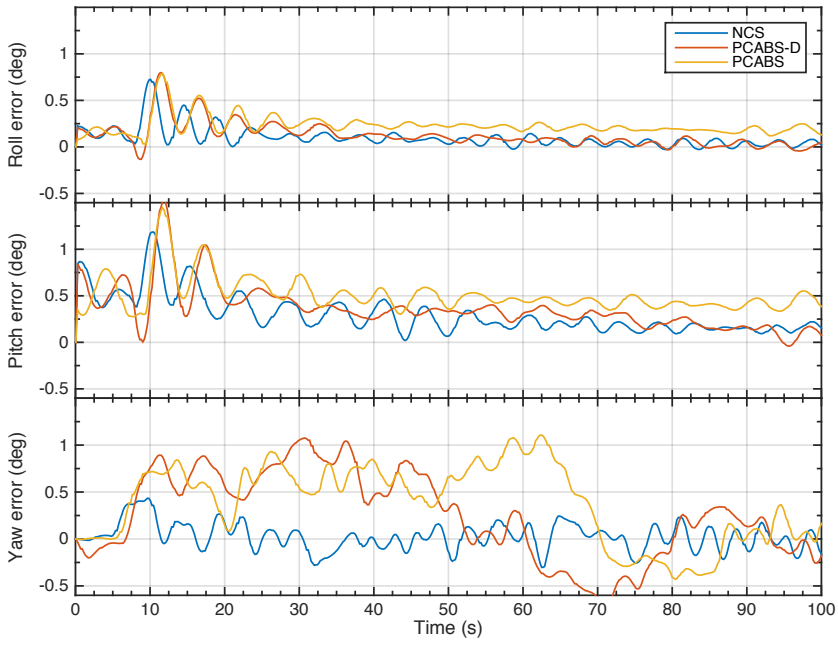

(b) Attitude errors

Figure 7.3: Scenario A. NCS show fast convergence to the setpoint whereas PCABS-D overshoots and PCABS drifts more than the other controllers.

7.2.2 Scenario B: Horizontal motion

After maintaining the position in the presence of current for 100 seconds, the ROV is commanded to move 3 meters forward, and 1 meter starboard relative to the initial position while maintaining the same heading (Fig.7.4). This test does only consider data after the first 100 seconds. A comparison is provided in Figure 7.5 along with position and attitude errors in Figures 7.6a and 7.6b. Supplementary information is found in Appendix B.

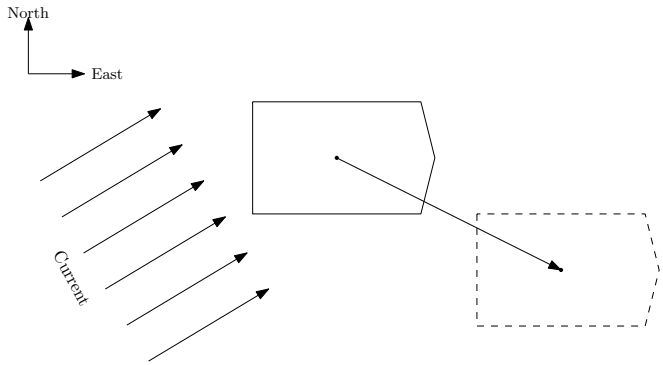

Figure 7.4: Simulation Scenario B. The objective is to move 3 meters forward and 1 meter starboard with current speed 1.5 knots and bearing 59 degrees.

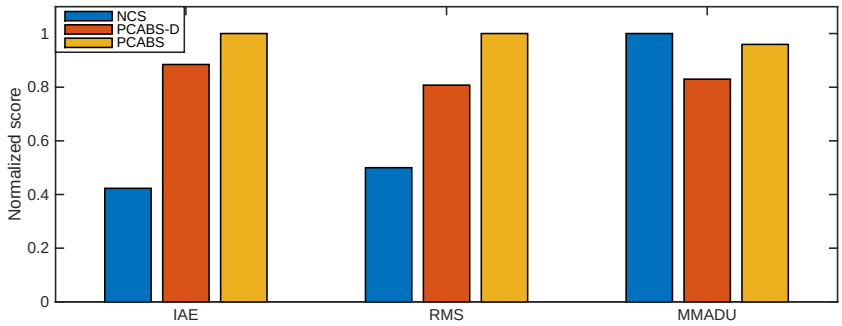

Figure 7.5: Scenario B. NCS is more effective in keeping errors small, but use more thrust. The integral terms of NCS are tuned more aggressively than for PCABS and PCABS-D.

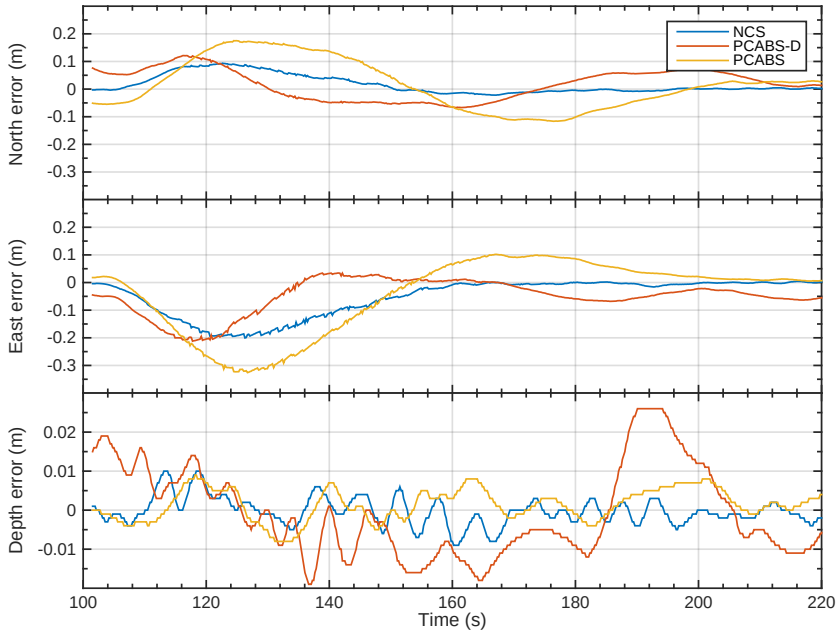

(a) Position errors

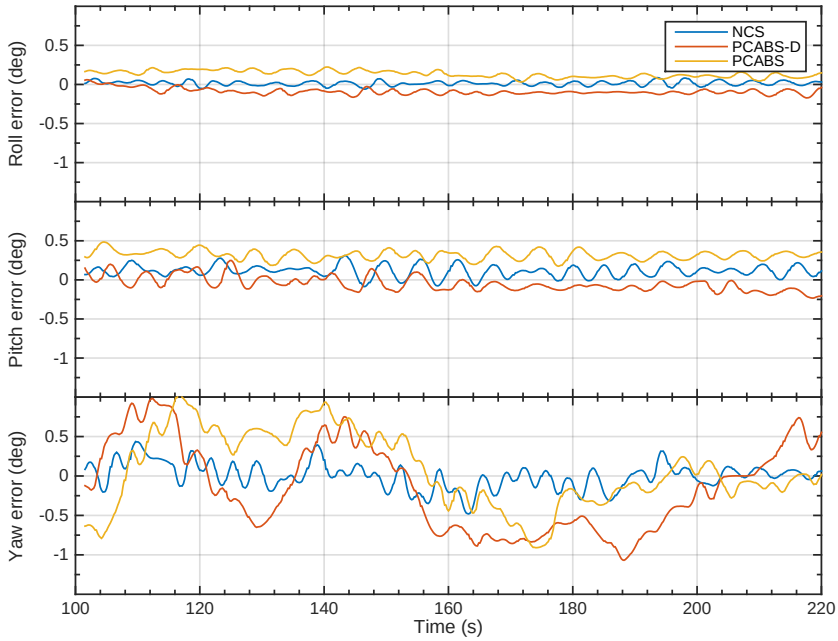

(b) Attitude errors

Figure 7.6: Scenario B. Current is compensated for during station keeping in the first 100 seconds, such that all controllers perform well in this simulation.

7.2.3 Scenario C: Rotational motion

After maintaining the position in the presence of current for 100 seconds, the ROV is commanded to rotate 90° in-place (Fig. 7.7). This test does only consider data after the first 100 seconds. A comparison is provided in Figure 7.8 along with position and attitude errors in Figures 7.9a and 7.9b. Supplementary information is found in Appendix B.

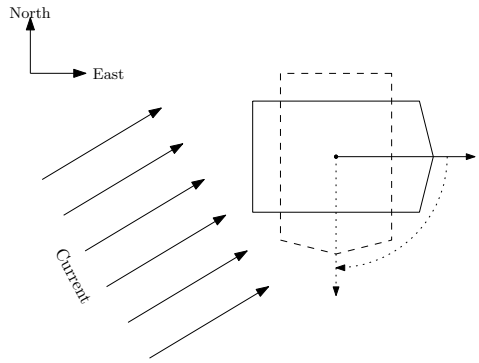

Figure 7.7: Simulation Scenario C. The objective is rotate 90 degrees in-place in the presence of current.

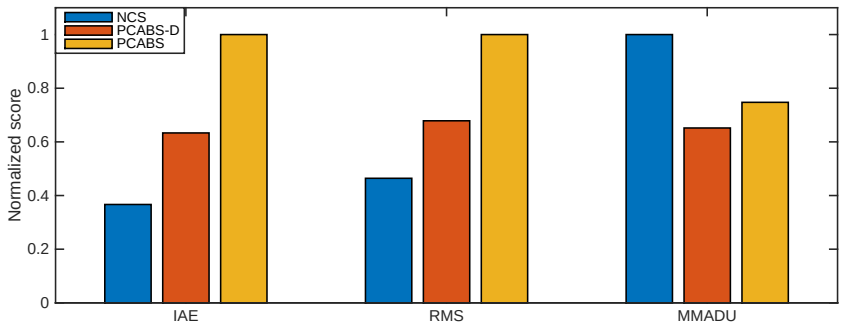

Figure 7.8: PCABS should have an advantage in this scenario, but is outperformed by the observer in PCABS-D.

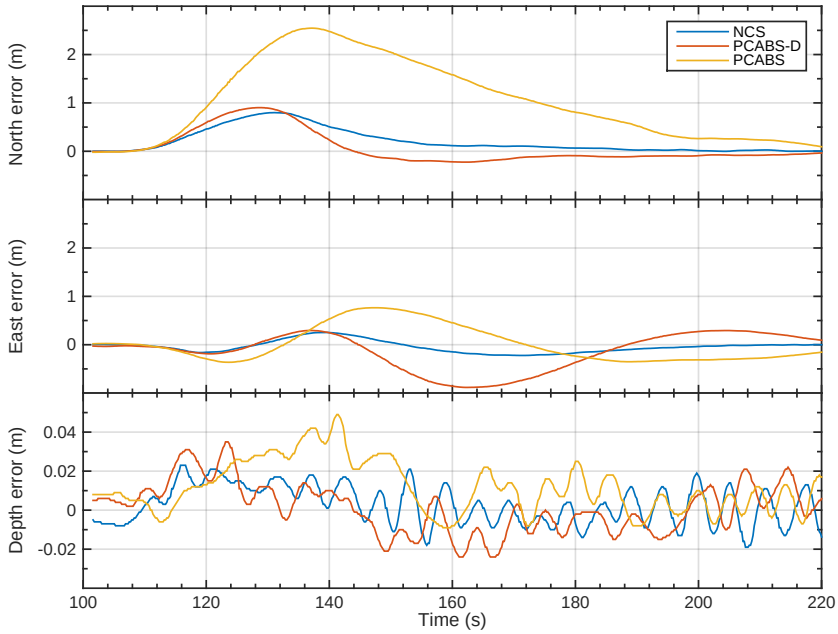

(a) Position errors

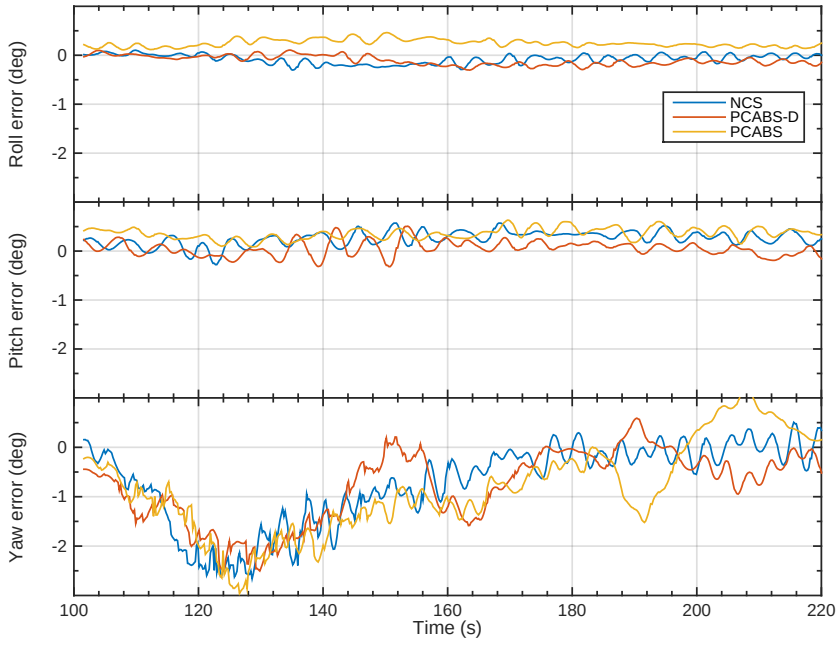

(b) Attitude errors

Figure 7.9: Scenario C. A current with speed 1.5 knots pose a great challenge as the disturbance is constantly changing its point of attack, seen from the ROV.

7.3 Joystick in the loop

The joystick module allows the pilots to position the ROV in a semi-automatic setting. When the current speed is small, pilots are in general not in need of such a system as they have good control over the vehicle. They also have bias adjustment controls at their disposal for manual feed-forward if necessary. However, when the current velocity approaches 2 knots, manual control is challenging and this is where the semi-automatic mode is useful.

The following simulations were done with 2 knots of current and the author was positioning the ROV over a landmark in the underwater terrain. Station keeping is turned off the first 10 seconds and the ROV is drifting due to the current (Fig. 7.10a). After approximately 180 seconds the current was turned up to 2.5 knots which cause the position to drift shortly before ending the test (Fig. 7.10b).

An important aspect of semi-automatic control in the presence of current, is the initialization of the controller when activating the control system, as described in Section 4.5. The effect of this initialization is best seen by studying the input. Figure 7.12a shows the surge force when activating station keeping without initialization, whereas the system is initialized in Figure 7.12b. The current was set to 1.5 knots when testing initialization.

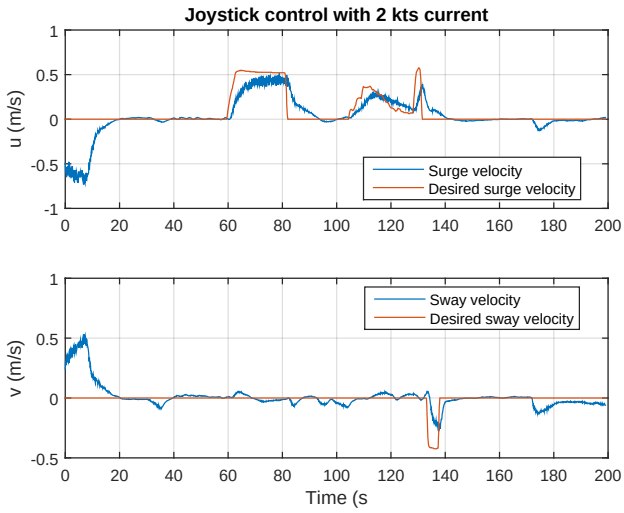

(a) Desired trajectories produced by the joystick

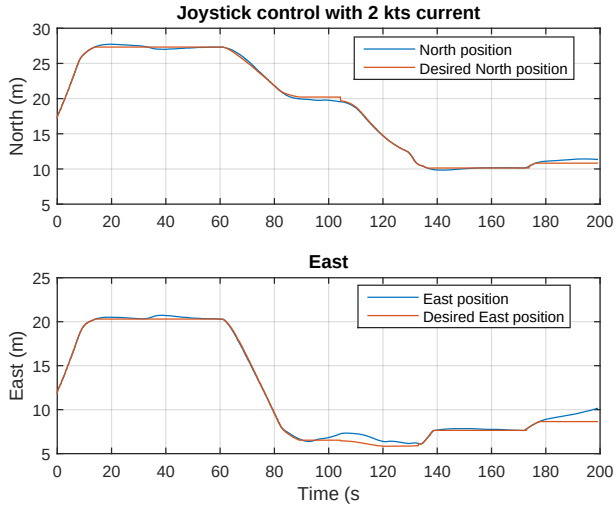

(b) Output tracking of North and East positions in semi-auto mode. Position control activated when the stick is inactive.

Figure 7.10: Using a joystick to move forward and sideways using the proposed joystick velocity reference model.

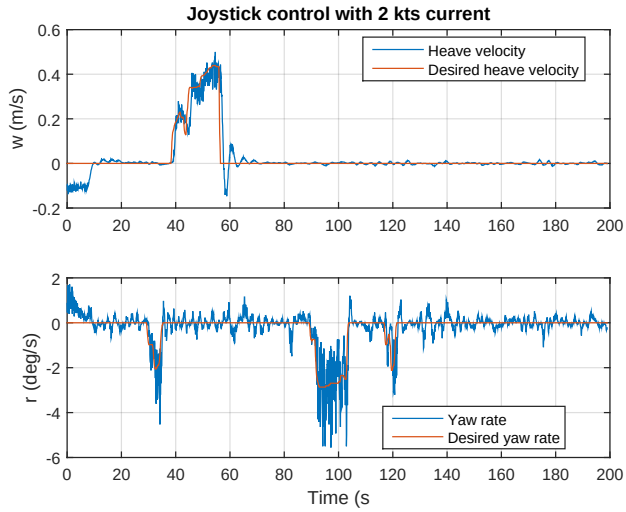

(a) Desired trajectories produced by the joystick

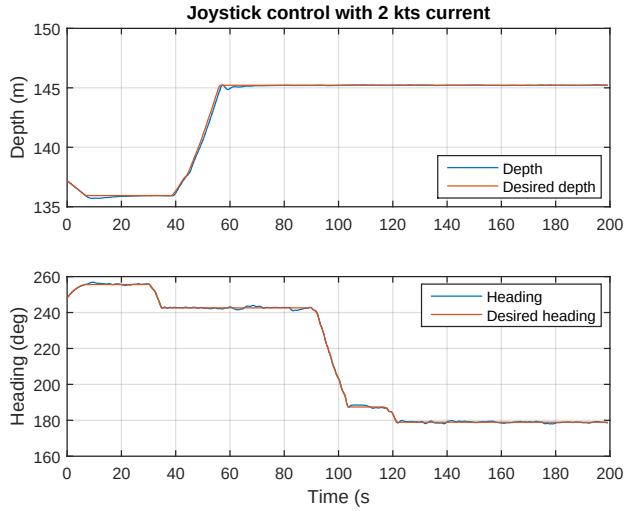

(b) Depth and heading

Figure 7.11: Using a joystick to dive and change heading with the proposed joystick velocity reference model.

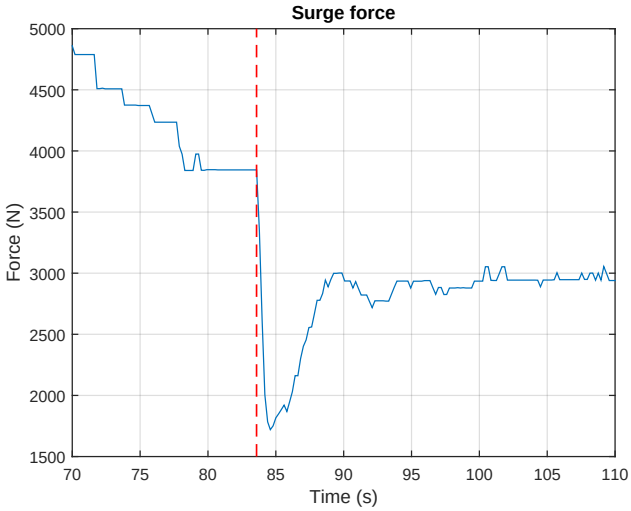

(a) No initialization.

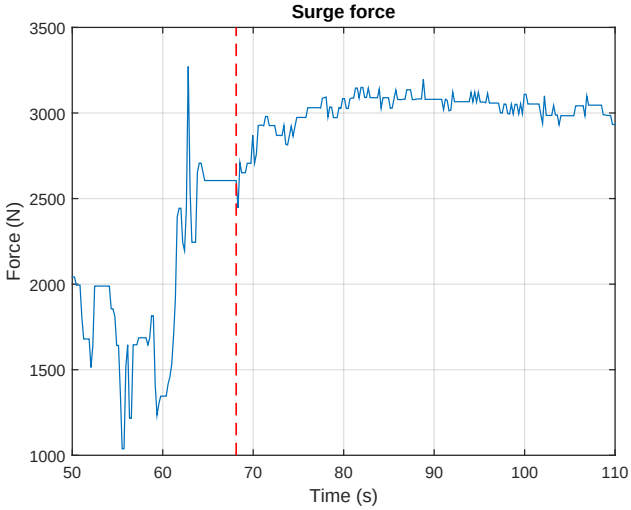

(b) With initialization.

Figure 7.12: Force in surge direction when activating station keeping in the presence of current with and without initialization of the controller. The switch is marked with the red dotted line.

7.4 Stress test

A stress test simulation is performed to push the control system to the limit. The current is set to 2.5 knots ($\approx$ 1.29 m/s) with bearing 59°. In addition, 3-4 meter high waves are introduced, corresponding to Beaufort number 6 with wind speeds at 22-27 knots (Price and Bishop 1974). This is the maximum setting in the simulator. Initially, the ROV is heading due East with heading 90° such that the current is attacking the ROV from starboard side, pushing it both forward and sideways (Fig. 7.13). There is slack in the tether to minimize disturbances from the waves. The objective is to maintain the initial position and attitude.

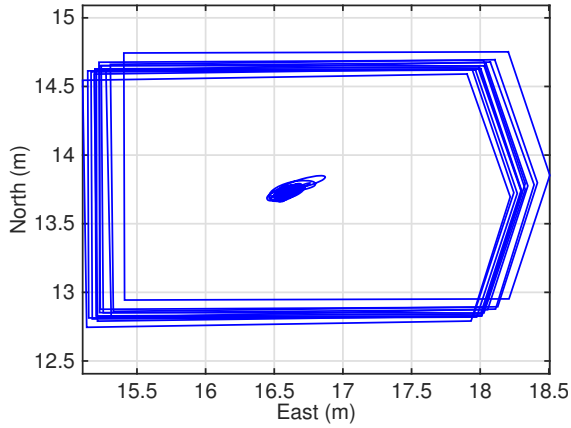

Figure 7.13: ROV outline with heading during station keeping after the transient period in simulated stress test.

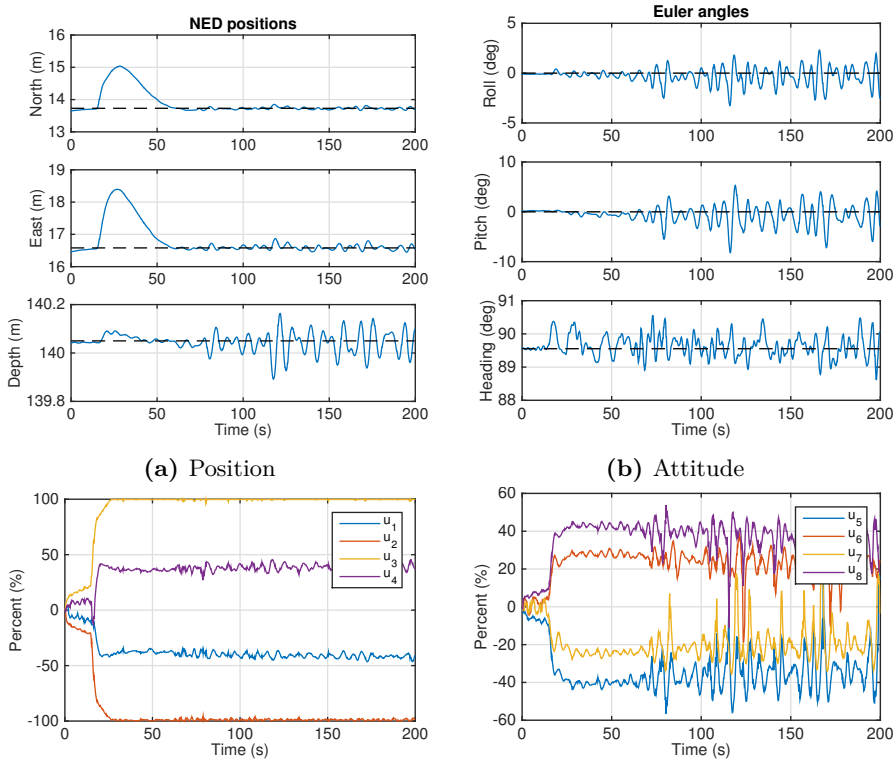

(a) Position

(b) Attitude

(c) Horizontal thrusters

(d) Vertical thrusters

Figure 7.14: Position, attitude and thruster usage during stress test with 2.5 knots current and Beaufort nr. 6. The dotted lines in Figure 7.14a and 7.14b indicate the setpoints. The ROV is able to maintain its position, but two thrusters are working at 100 % such the ROV cannot fully compensate for the environmental disturbances.

7.5 Waypoint Tracking in 2D

The LOS guidance law for fully actuated vehicles are demonstrated by tracking a set of waypoints. The velocity control scheme from Section 4.4 in Chapter 4 is applied for surge and sway when moving in the plane.

7.5.1 Visiting each point

In the first case, the ROV should visit waypoints around subsea installations in a survey-like mission (Fig. 7.15 and 7.17). The guidance law is used in a traditional setting where heading is directed toward the next waypoint. The constant jerk reference model from Section 5.2.1 in Chapter 5 (Table 7.5a and 7.5b) is used to generate reference trajectories for surge velocity and yaw rate. The guidance system operates as a state machine where the ROV should adjust course before going into transit toward the next waypoint. Position control is activated for surge and sway when adjusting course, but deactivated when moving in the plane. Velocity, yaw rate and cross-track error are shown in Figure 7.16.

Table 7.5: Parameters applied to the constant jerk reference model for waypoint tracking. The parameters are adjusted by an algorithm to ensure feasible trajectories.

(a) Parameters for surge

Parameter	Value	Unit
Jerk	0.1	m/s^3
Acceleration	0.1	m/s^2
Speed	1.0	m/s

(b) Parameters for yaw

Parameter	Value	Unit
Jerk	0.05	rad/s^3
Acceleration	0.01	rad/s^2
Speed	0.1	rad/s

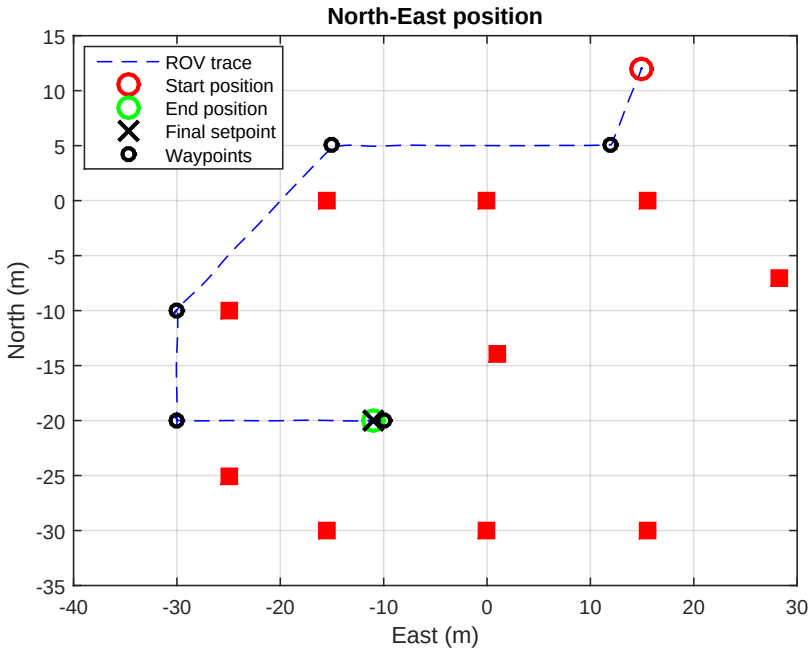

Figure 7.15: North-East plot over seabed during waypoint tracking. The red boxes represent subsea installations. The ROV adjusts the course to the next waypoint before transit.

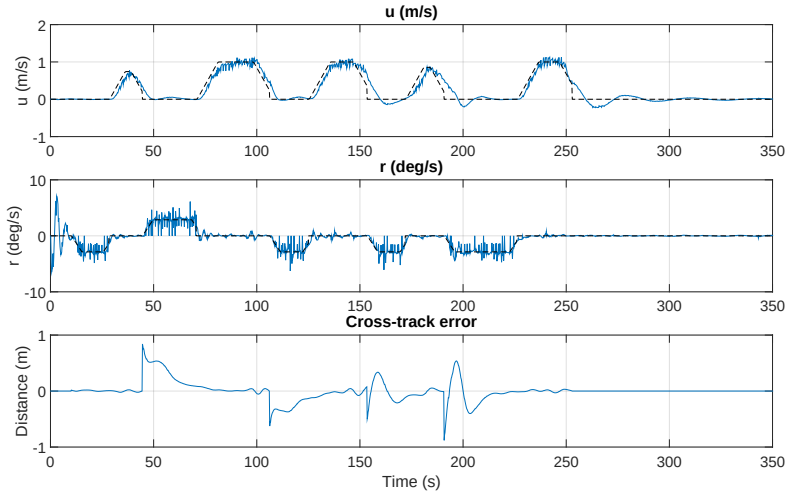

Figure 7.16: Forward velocity, yaw rate and cross-track error during waypoint tracking.

7.5.2 Path following

The same waypoints are used to define a path for the ROV to follow (Fig. 7.18). As in the reverse path problem considered in Ohrem (2015), the waypoints are assumed to have been created by the ROV when it was moving through the ocean space. The objective may now be to return to the TMS by reversing the already driven path while maintaining the heading angle. The LOS guidance law is applied to the velocity vector (Fig. 7.21), leaving heading to be controlled independently of direction of travel (Fig. 7.19). North and East positions are shown in Figure 7.20 and depth in Figure 7.19. The speed along the path U_d is set to the constant value 0.4 m/s (≈ 0.78 kts).

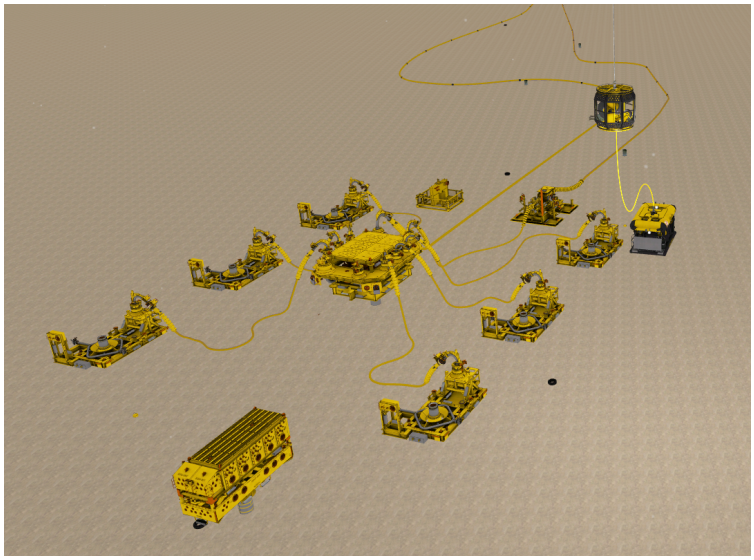

Figure 7.17: Simulated subsea enviroment. ROV in transit between waypoint 1 and 2.

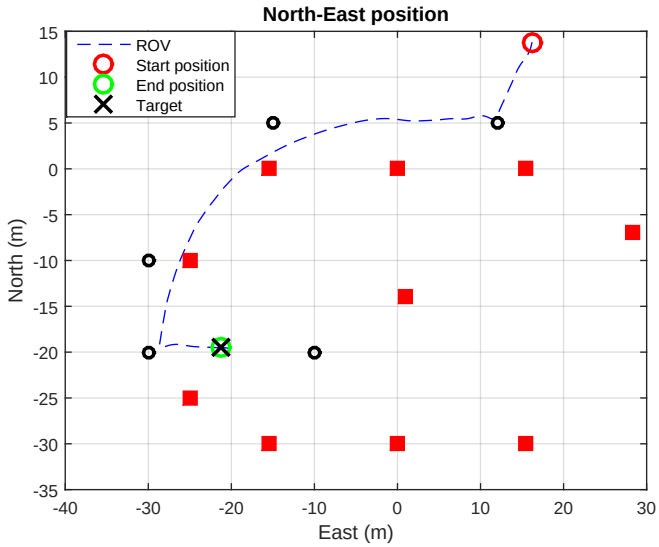

Figure 7.18: A path is implicitly defined by the waypoints. The ROV follows the path by directing the velocity vector toward the next waypoint, leaving heading fixed at 90 degrees. This can only be accomplished for fully actuated vehicles. It is not necessary to visit each point in this scenario, such that the ROV makes smoother motions than when stopping at each point.

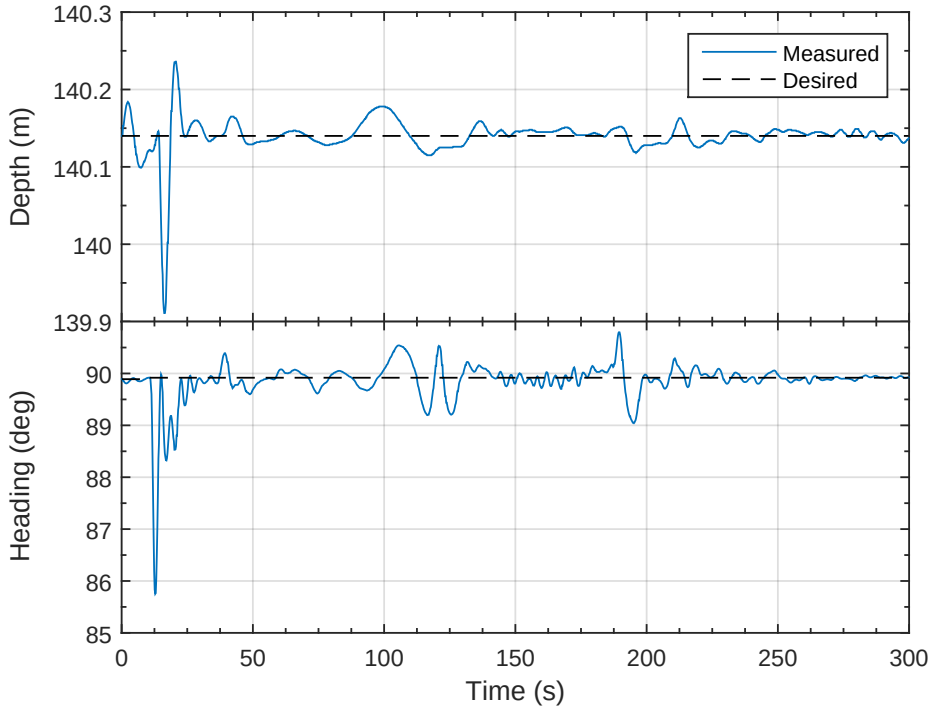

Figure 7.19: Depth and heading are regulated to constant values when following the path. The direction of travel is independent of the heading as the ROV is fully actuated.

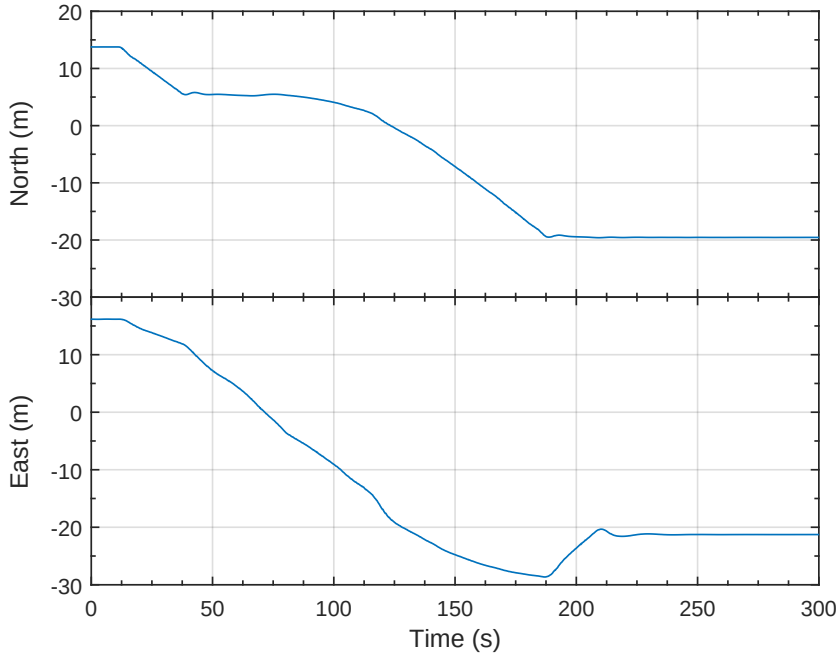

Figure 7.20: Uncontrolled North and East positions in path following.

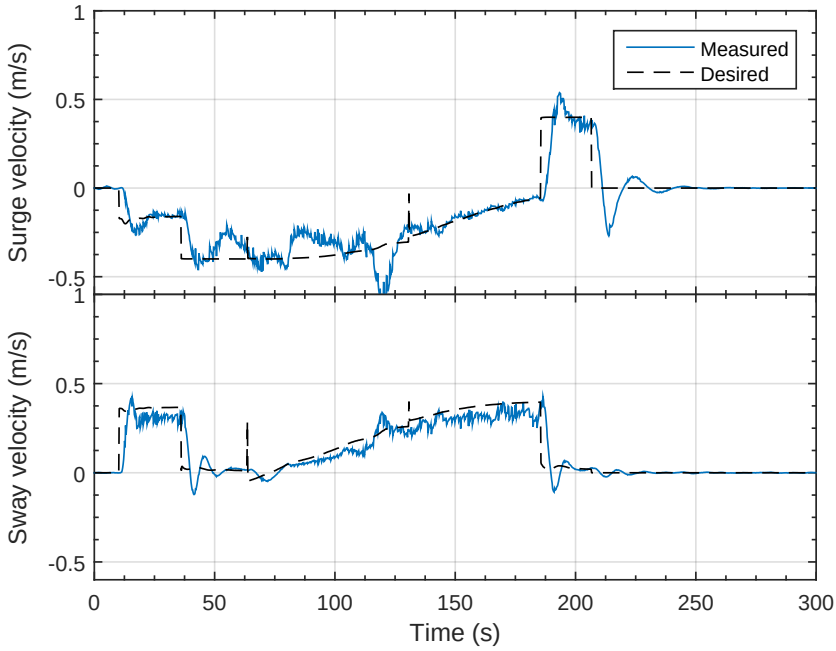

Figure 7.21: Surge and sway velocities with desired trajectories.

7.6 Control action of NCS

It is concerning to use both adaptation and a disturbance observer at the same time, as these two sets of integrators may interact and cause problems. Furthermore, it is of interest to investigate the influence of actuator dynamics compensation on the control action. The performance of the control system when omitting adaptation (Fig. 7.22), is investigated in the previously mentioned Scenarios A-C. As the results in each Scenario were fairly similar, only results from Scenario C are presented (Fig.7.23, 7.24a and 7.24b). Supplementary information can be found in Section B.2 in Appendix B.

The control action from these simulations are unfortunately unavailable, such that the control inputs from path following found in Section 7.5.2, are studied instead. This should not pose a problem for the analysis, as the objective is to investigate the contribution of adaptation, disturbance observer and actuator dynamics compensation on the control law, which are not bound to a specific scenario.

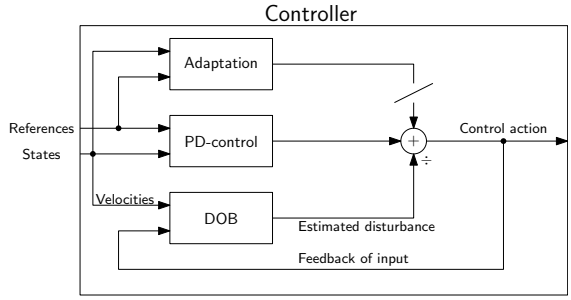

Figure 7.22: NCS without parameter adaptation.

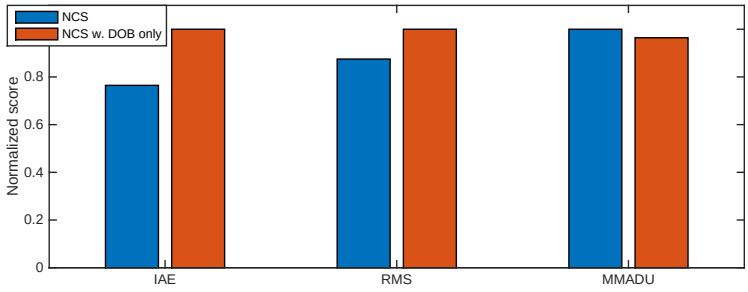

Figure 7.23: Scenario C is simulated for NCS with and without adaptation.

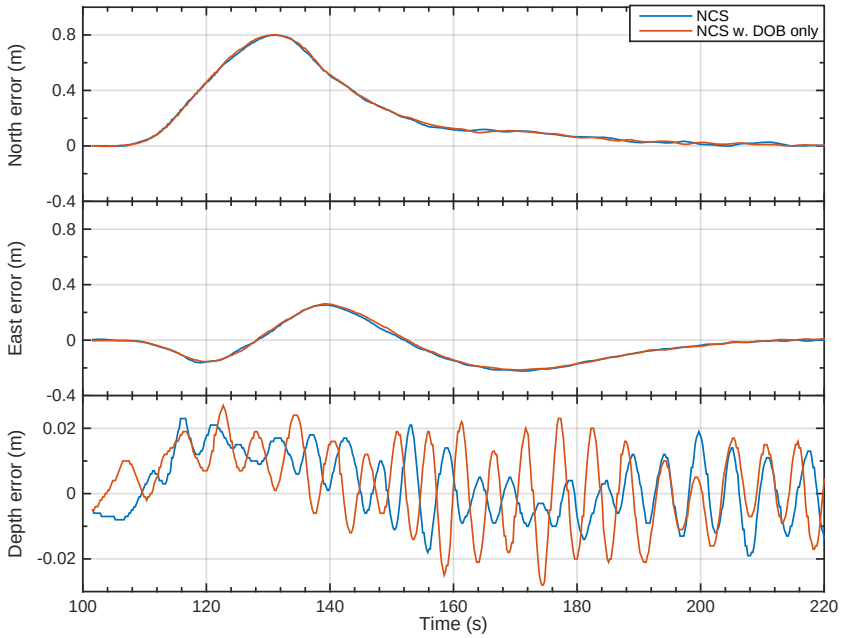

(a) Position errors

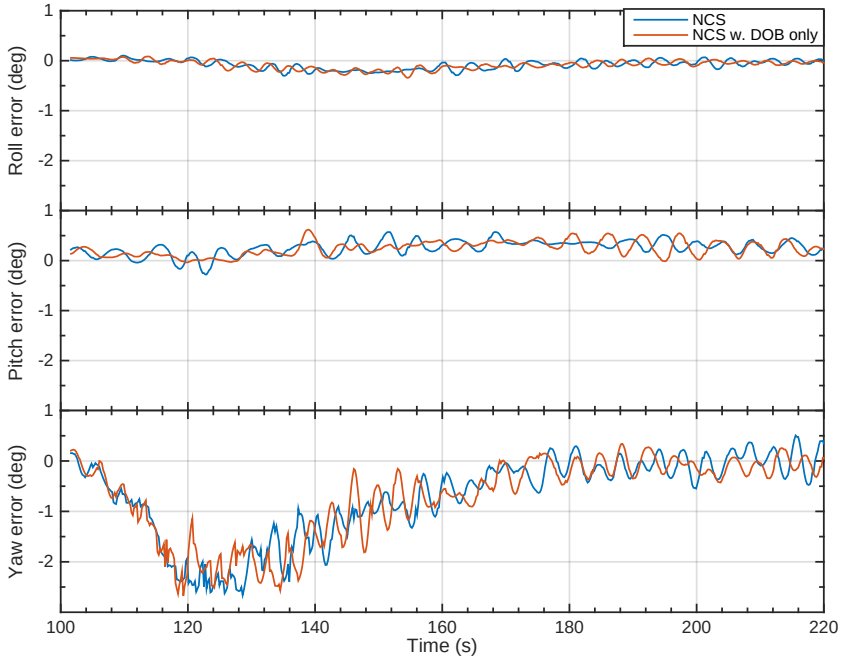

(b) Attitude errors

Figure 7.24: The influence of adaptation is seemingly small compared to when only an observer is used.

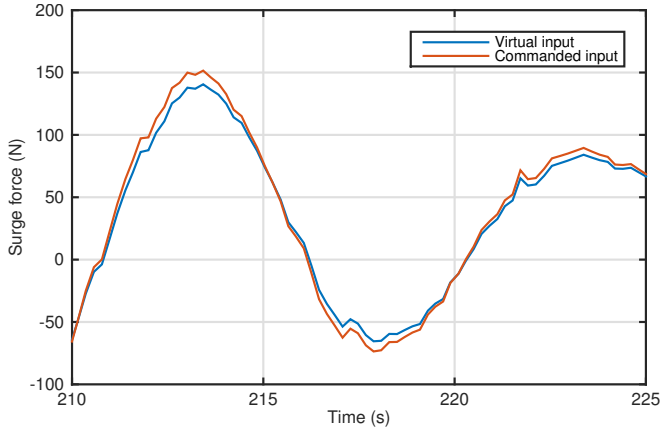

(a) Close-up of virtual and commanded sway force in path following

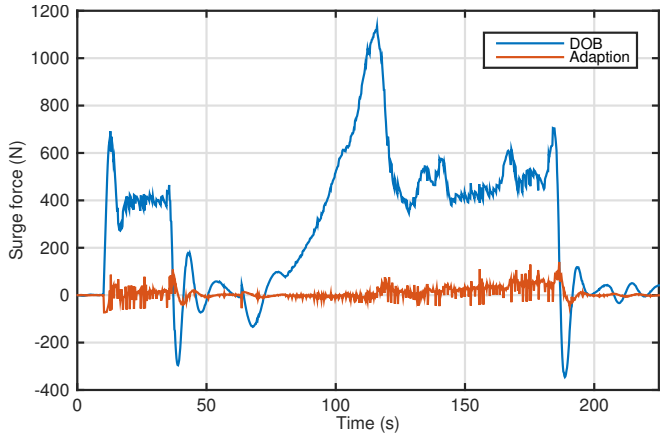

(b) Adaptation and estimated disturbance in sway in path following

Figure 7.25: Path following. The virtual control action (used by PCABS/PCABS-D) is about equal to the commanded control action, which includes compensation of the actuator dynamics (used by NCS). The integral action is dominated by the disturbance observer.

7.7 Discussion of results

7.7.1 Scenario A

All controllers are able to reject the disturbance and satisfy the control objective. In terms of keeping errors small, NCS score better than PCABS-D and PCABS, but use more thrust due to more aggressive tuning (Fig. 7.2). Using NCS, North and East positions settle fast and without overshoot (Fig 7.3a), and heading is kept within a bound of roughly ± 0.25 degrees (Fig 7.3b). All controllers stabilize roll and pitch, but PCABS show the largest deviation from the setpoints. If given more time, the integral action would probably regulate roll and pitch to zero. PCABS shows the best depth regulation, whereas PCABS-D and NCS cause oscillations. This is most likely due to the disturbance observer using excessive gain in heave. Moreover, PCABS show drift in North-East before settling, whereas PCABS-D overshoots. This may suggest conservative adaptation gain $\mathbf{\Gamma}$ and too large disturbance observer gains in $\mathbf{K}_{dob}$ for surge and sway in PCABS-D. On average, PCABS-D spend an equal amount of thrust as PCABS, and at the same time showing tighter control of the position errors. This suggests that adding a disturbance observer has a positive impact on the performance and disturbance rejection capabilities.

7.7.2 Scenario B

The observations made for Scenario A may be restated for the results of Scenario B. Fig 7.5 shows that NCS score best in terms of keeping errors small, but use more thrust than PCABS and PCABS-D. The input necessary to compensate for the current has been built up before moving horizontally, such that all controllers show only small deviations from the setpoints (Fig.7.6a and 7.6b). They are however showing the same trends as in Scenario A: Considering North and East, PCABS is deviating the most from the setpoints, PCABS-D overshoots and NCS converge nicely. PCABS and NCS show good depth control, whereas PCABS-D show larger deviations. The reader should keep in mind the scale of the figure, where the relatively large deviation is still within 3 cm from the setpoint. NCS is able to maintain its heading far better than PCABS and PCABS-D, as it is deviating less from the trajectory.

7.7.3 Scenario C

Scenario C constitute the most challenging control problem among the three scenarios, as the ROV must rotate in the force field of the current. Thus, the disturbance is constantly changing seen from the ROV. It is in situations like this the PCABS controller should have an advantage as the current is parameterized in the controller as constant in the NED frame, meaning that the compensation of the current rotates with the ROV. However, PCABS show significant drift compared to the other two controllers, especially in North, and also the largest deviations in heading (Fig. 7.9b). The raw data found in Appendix B.1.3 show that PCABS-D does the best job of stabilizing roll, pitch in terms of IAE and RMS, and heading in terms of RMS. It is also slowly oscillating in East, which may be due to excessive gains in the observer, as mentioned in the discussion of Scenario B. Figure 7.8 shows that the overall best controller is NCS, followed by PCABS-D.

7.7.4 Overall discussion of Scenarios A, B and C

It is evident from these simulation scenarios that NCS is the best performing controller with respect to keeping position errors small. This is not surprising as the integral terms are tuned more aggressively. However, the objective of these tests was not to simply compare different controllers, but to document if an increase in performance could be traced back to additional complexity and modeling. PCABS-D extends PCABS by adding a disturbance observer (see also Figure. 4.1 in Chapter 4), which greatly improves the disturbance rejection capabilities (Fig. 7.2, 7.5 and 7.8). The same figures also show that on average, PCABS-D spend less or equal to the amount of thrust as PCABS, all while showing tighter control of the states. Thus it would seem as the biggest contribution to improved results, is the disturbance observer. Despite the observer in PCABS-D being excessively tuned for surge, sway, and heave, its performance comes close to that of NCS. This may suggest that the additional complexity of NCS is superfluous. Section 7.6 investigates the control action of NCS in more detail.

Finally, the roll and pitch angles are small (Fig. 7.3b, 7.6b and 7.9b), such that the assumptions for using vessel parallel coordinates are met. This greatly simplify the implementation of the kinematic equations (Eq. 3.1), by reducing the amount of trigonometric expressions to be evaluated at run-time. Furthermore, the roll and pitch angles seem to oscillate with periods of 5 and 6 seconds, which is very close to the estimated natural frequencies from Section 3.4.1 in Chapter 3). These oscillations are due to coupling between the surge-sway and roll-pitch subsystems,

where motions in surge and sway cause motions in roll and pitch. The amplitudes of oscillations are however small ($\approx < 0.5$ degrees), but one could add low-pass or notch filters to prevent these frequencies from entering the control loop, if necessary. This to prevent the controller from unintentionally exciting the natural periods.

7.7.5 Joystick in the loop

It is hard to capture the experience felt by the user with figures and plots. It does not matter to the user if the desired velocity is not perfectly tracked. What matters is if the ROV moves when you want it to move, and if it stops when you want it to stop. The author have no experience from flying ROVs other than using the simulator at IKM Subsea, which despite some discrepancies with the physical world, is still considered a platform for training pilots. Figure 7.10a show that the ROV is tracking the velocity references and updates the desired North and East positions accordingly, by means of output tracking, shown in Figure 7.10b. At approximately 90 seconds the East position starts to drift, which is caused by the change of heading shown in Figure 7.11b. Changing depth is also done with ease, but there are no disturbances affecting depth in these simulations.

Figures 7.12a and 7.12b show the effect of the proposed solution for controller initialization. With 1.5 knots current, the ROV was stabilized manually before activating station keeping. When the controller is not initialized, the input forces make a large drop before returning to the level necessary to withstand the current. With initializing, it is seen that only a small adjustment is necessary to stabilize. Proper initialization ensures predictable behavior and minimize drift due to current when activating station keeping.

7.7.6 Stress test

The objective of the stress test was to find a set of extreme operational conditions in which the control system is still functional. In this test the current was attacking the ROV from starboard side pushing it both forward and sideways. In addition, waves were introduced at Beaufort number 6 causing the TMS to move up and down periodically. Thanks to the TMS, these motions have little effect on the ROV after deploying some tether, as seen in Figure 7.14a. Furthermore, Figure 7.14c show thruster 2 and 3 of the horizontal thrusters (see Figure 3.5) working at full speed. The control forces are saturated, but the force ratio is maintained such that the ROV is able to maintain the position (Fig. 7.13 and

7.14a.) In these conditions, the heading deviations are bounded within approximately $\pm$ 0.5 degrees from the setpoint (Fig. 7.14b). Roll and pitch are not regulated to zero in these conditions. Station keeping is functional in these conditions, but the control forces are saturated. An upper limit to the amount of current the system can handle seem to be 2.5 knots. This limit may however be higher or lower in the real world.

7.7.7 Waypoint Tracking

Visiting waypoints

Figure 7.15 shows that the ROV positioned itself slightly West of the final waypoint, which can be explained by how the guidance system handles the final waypoint and the radius of acceptance. When the ROV has reached the final waypoint, the guidance system will output the current position as the new setpoint, shown as "Final setpoint" in 7.15. One could avoid this simply by setting the final waypoint as the new setpoint instead. This is not seen for the other waypoints, as course should be adjusted before transit. When changing course, position control is activated in surge and sway, which positions the ROV on or close to, waypoint $\mathbf{p}_k$. This also explain why the cross-track error makes sudden jumps in Figure 7.16.

When the ROV is within the circle of acceptance of waypoint $\mathbf{p}_{k+1}$, the index k is updated and the next waypoint, currently $\mathbf{p}_{k+2}$, is loaded to calculate a new course (Fig. 7.26). The cross-track error is large since the new waypoint is loaded before the ROV is fully positioned on the current waypoint $\mathbf{p}_k$. This can be seen as the jumps occur at the same moment as the desired yaw rate changes from zero in Figure 7.16. Also note that during the time when the ROV changes course, the cross-track error is reduced due to position control, as stated above. During transit, the cross-track error is small, hence the fairly straight trace-lines seen in Figure 7.15. Due to a technicality in the implementation, the cross-track error is constant toward the end of the simulation after reaching the final waypoint.

Adjusting the course before transit gives a predictable system as the position and orientation are separate control problems, although the motions of the ROV may not be perceived as dynamic.

Path following

The LOS guidance law for fully actuated vehicles are demonstrated in full by following a simple path based on the same waypoints (Fig. 7.18 and 7.27). Fig-

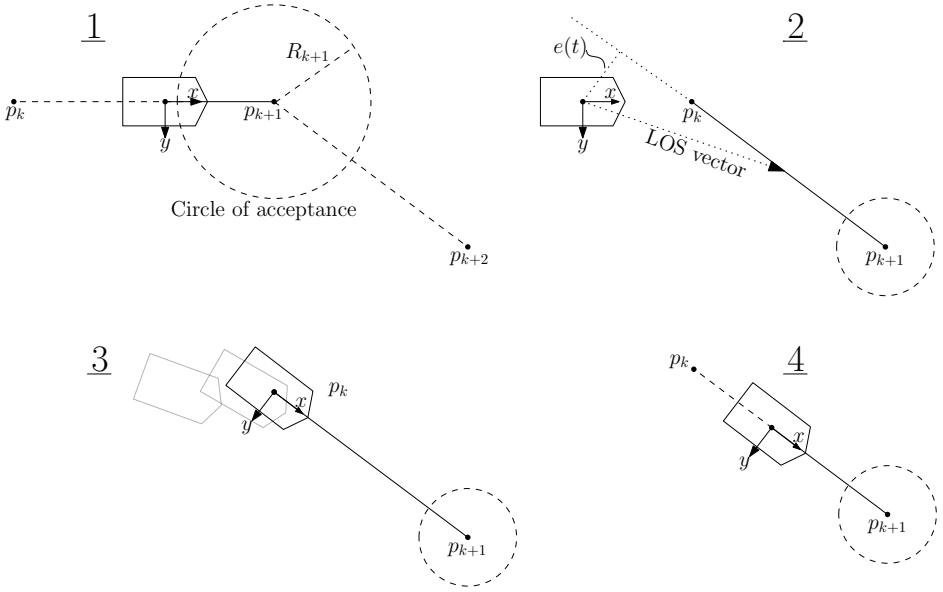

Figure 7.26: In the visiting waypoints scenario, the LOS guidance law is used in a traditional setting where the heading is directed toward the LOS-point. A cross track error is present when switching waypoint (2) as the ROV is not entirely positioned on the previous waypoint before making the switch (1). Position control is activated when adjusting course (3), such that the ROV positions itself on the previous waypoint p_k before moving toward the next waypoint (4).

ure 7.20 show smooth North and East position trajectories, while some spikes are seen in the desired velocity profiles (Fig. 7.21), which is most likely due to an implementation bug in the guidance system. Merlin WR200 follows the path by moving backwards and sideways, as if returning along an already driven path, while maintaining the heading angle (Fig. 7.19). This system could benefit from more tuning, and perhaps more waypoints, to be used in a proper reverse-path scenario as in Ohrem (2015).

Although the results presented for path following are not particularly impressive, one should rather focus on the bigger picture. Using a LOS guidance law that utilize full actuation of the vehicle, adds numerous possible operating modes. One could plot a route on a map for the ROV to follow, e.g. along a pipeline, and let the pilot control the velocity along the path as well as heading. The pilot may independently change heading to get a better view, all while the ROV is moving toward the next waypoint. If a point of interest occurs, one may pause

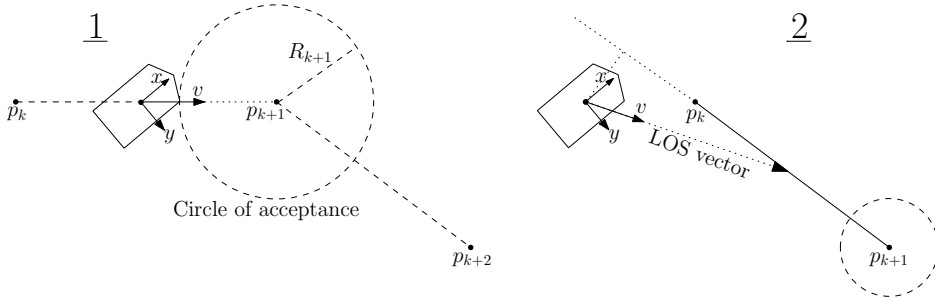

Figure 7.27: The ROV is moving between waypoints with a fixed heading, and aligning velocity and LOS-vector.

path following and use the semi-automatic mode to position the ROV properly for inspection. As such, the demonstration of the LOS guidance law show very promising results for future work.

7.7.8 Control action of NCS

It is clear from Figure 7.24a and 7.24b that the contribution from adaptation is small when used together with a disturbance observer. Only a minor difference can be seen in terms of keeping errors small and use of thrusters (Fig. 7.23). The most notable difference is seen in depth control, where the control system seem to be exciting the natural frequency in heave when adaptation is omitted. This may indicate that adaptation and the observer interact in a positive manner, at least in heave. In this case, the gains of the observer should be reduced to remove oscillations[1]. By studying the control action from path following in 7.5.2, it is seen that adaptation has a small influence as the observer is dominating the integral action (Fig 7.25b).

Furthermore, compensation of actuator dynamics seem to have a minimal effect on the control action (Fig. 7.25a), which may explain why PCABS-D was coming close to the performance of NCS (Section 7.2). A linear model was used to model the thruster dynamics in Equation (3.37) in Section 3.4.2, even though the delay is known to be caused by a ramp filter. The proposed linear model may not be

[1]This may be connected to the excessive depth oscillations seen during sea trials when adaptation was kept off. The problem was removed by reducing the observer gains, where it was reduced from 1000 to 100 for heave. It should be noted that the depth was oscillating with a period of about 35 seconds, suggesting heavier weight than anticipated or insufficient added mass in the model. The former is most likely the case as the pilot commented on the heavy weight of the ROV.

effective in describing this delay. One may thus simplify the controller by leaving out actuator compensation, such that the final control law can be given by the simpler expression of Equation (4.45) from Section 4.2.3, or pursue some other model.

Both the observer and adaptation scheme work toward the same goal of providing corrective inputs based on integrating position and velocity errors. The disturbance observer (Fig. 4.3) takes velocity signals and the control action as input $\boldsymbol{\tau} = \dot{\boldsymbol{\tau}}_v + \boldsymbol{\tau}_a - \boldsymbol{\tau}_d - \mathbf{K}_2 s$ (Fig. 7.28), which consist of position and velocity error signals, and the adaptive term. The observer is adjusting the estimated disturbance until it can balance the equations of motion. The signal $\mathbf{s}$ consist of both position and velocity errors, and is also integrated in the parameter estimate update law in the adaptation scheme (Fig. 4.3). Adaptation thus rely on pure feedback from the states of the ROV to produce a corrective action, whereas the observer seem to be able to correct its output more efficiently by using the control action as well.

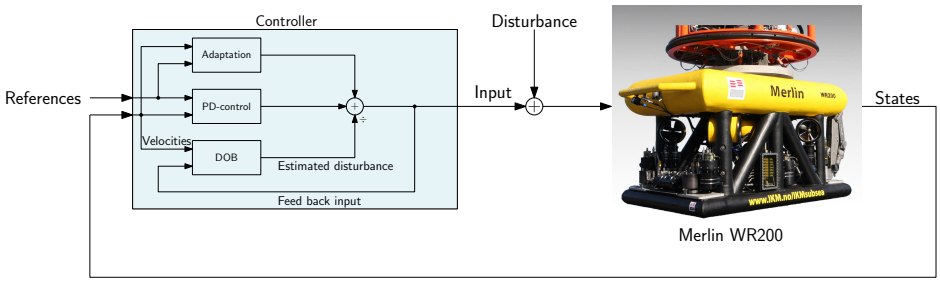

Figure 7.28: A simplified version of the control system

Chapter 8

Sea Trials

On December 7th 2015, the author, co-supervisor and a former ROV pilot mustered on KL Saltfjord in Bergen to test the proposed dynamic positioning system. Full-scale experiments were carried out in the Byfjord of Bergen and at Mongstad during a period of 3 days. A hydraulic hose in the crane system burst on the first day of testing, delaying the project for 1 day. Prior to these tests, the control system was implemented on an OMRON PLC and integrated with the navigation system developed in Knausgård (2013). The implementation of the control law was verified through Hardware-in-the-loop (HIL) tests using the simulator at IKM Subsea Solutions AS, Bryne, which showed excellent results. An overview of the main components for full-scale experiments is shown in Figure 8.1.

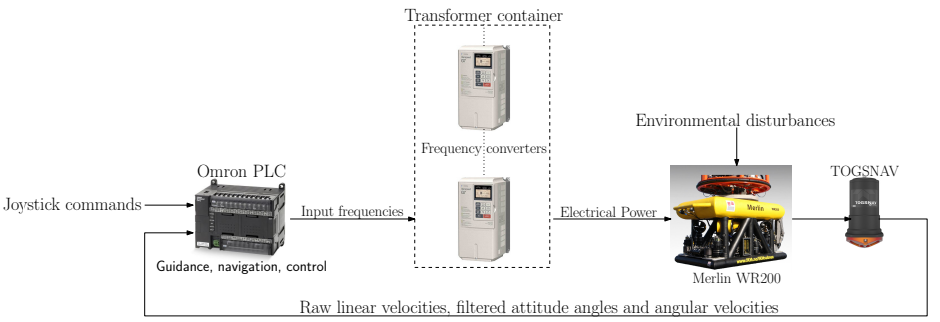

Figure 8.1: An overview of the components necessary for full-scale experiments.

The following tests were performed

- Submerge the ROV in water while still attached to the TMS and verify the position estimate of the EKF
- Fly the ROV away from the ship and activate station keeping
- Test robustness of disturbance observer by changing damping coefficients.
- Test station keeping without adaptation
- Low-speed maneuvering using joystick

A discussion of the results can be found at the end of this chapter.

Figure 8.2: Work place and control room onboard KL Saltfjord. The ROV is typically operated by two pilots. Video feeds from the ROV and other information are shown on the monitors.

8.1 Sensor setup

Dynamic positioning for Merlin depend on the TOGSNAV sensor unit, shown in Figure 8.3. It is a solid state gyrocompass based around a Fibre Optic Gyro (FOG), with an Inertial Measurement Unit (IMU), a DVL and a pressure gauge. The navigation system consist of one EKF filtering the linear velocities u, v and estimates a local North-East position, and an EKF for depth filtering and heave velocity estimation. Merlin WR200 is also equipped with an external altimeter and an external depth sensor, which was used instead of the pressure gauge in

the TOGSNAV which proved to be malfunctioning. The TOGSNAV sensor used in the full-scale experiments is the exact same unit that was used in the sea trials in Knausgård (2013).

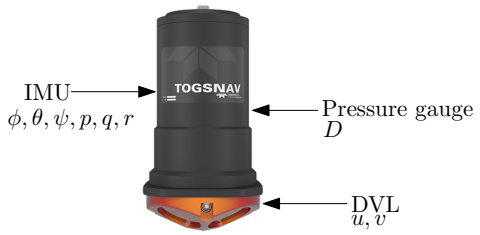

Figure 8.3: The TOGSNAV sensor unit.

8.2 A note about the navigation system

Knausgård (2013) concludes that the EKFs in the navigation system should be tuned with respect to the bias modeling. Furthermore, the commanded input had to be taken out of the filter equations to obtain better estimation. Using the new thruster model introduced in Section 3.5.3 is assumed to improve this matter. Furthermore, a potential issue was detected in the implementation of the EKF. Since Kalman filter implementation is not treated in this thesis, necessary actions to fix the problem can be found in Appendix D. However, Knausgård (2013) reports very good position and depth estimation, and hence the estimator was used as-is, leaving more time to verify the functionality of the new control system.

It should be noted that the navigation system provides a local position, as there are no position measurements. This means that the local NED origin is the point in space being occupied by the ROVs CO when the system is activated. This is seen in the resulting figures in this chapter as the North-East positions vary about zero meters. The absence of position measurements makes the system prone to drift, as there is no way to correct for a wrongly estimated position. As a benchmark, Dukan, Ludvigsen, and Asgeir J. Sørensen (2011) reports full-scale experiments on the small size Minerva ROV. Navigating using an EKF without measuring position while tracking a box-pattern, showed significant drift compared to when having these measurements. Thus, the DP system for Merlin is expected to perform well only within a small range.

8.3 Preparations

The first test was to verify the functionality of the position estimator by holding the ROV as still as possible and logging the estimated position. This was done in the Byfjord of Bergen at 70 meters depth with the ship positioned using DP. In the absence of any solid foundations to grip and hold on to, the best option was to keep the ROV attached to the TMS to minimize movements. A North-East plot of the logged data is shown in Figure 8.5. Data was logged in series for approximately 10 minutes at different depths giving consistent data. It was noticed that the position estimate would drift more when closer to the seafloor. Looking at the video stream from the cameras onboard the TMS and the ROV showed minor movements of the TMS/ROV assembly. These motions were most likely caused by raising and lowering the ROV. It was thus assumed that the position estimator was working properly and well suited for dynamic positioning.

Figure 8.4: ROV attached to TMS while being deployed from the starboard side of ship at the docks of Mongstad.

The direction of input was verified by sending commands to individual thrusters. A correct setup was confirmed by manual inspection of the propeller rotations with the ROV on deck, and also by monitoring the direction of applied thrust which is available to the pilot on a monitor. It was of special interest to confirm that the center of gravity lay below the center line of the horizontal thrusters, enabling us to know how roll and pitch motions are affected by surge and sway

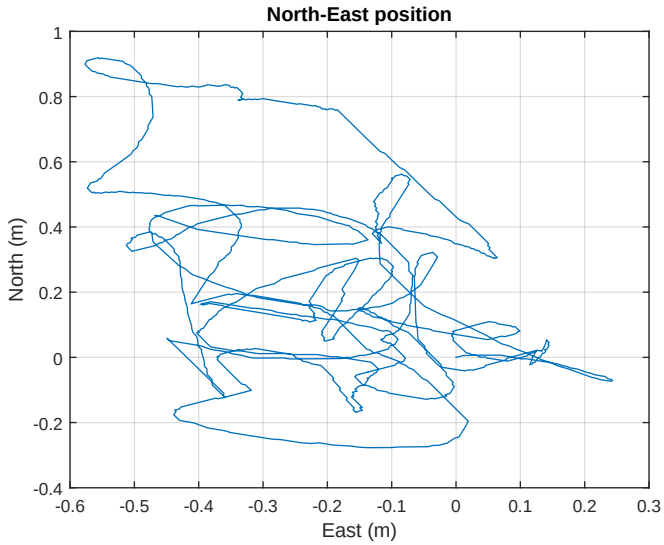

Figure 8.5: North-East plot with ROV attached to TMS at 70 meters depth. The ship was positioned using DP, but lay very still due to calm sea. (Bergen).

motions. Controlling roll and pitch was in issue in Knausgård (2013) and Ohrem (2015), leading to 4DOF control in both theses.

8.4 Day 2 - Bergen, Byfjorden

Station keeping was activated using the settings from HIL tests at IKM, Bryne. The ROV was stabilized, but most states were however oscillating, most notably depth (Fig. 8.7). Oscillations may indicate aggressive tuning and thus both adaptation and disturbance observer were turned off in order to verify the feedback gains in the controller, shown in Figure 8.6. Most states were still oscillating without integral action, but not as severe.

8.4.1 Station keeping

Having verified the feedback gains, integral action was gradually turned on. The disturbance observer gains had to be reduced to the values in Table 8.1.

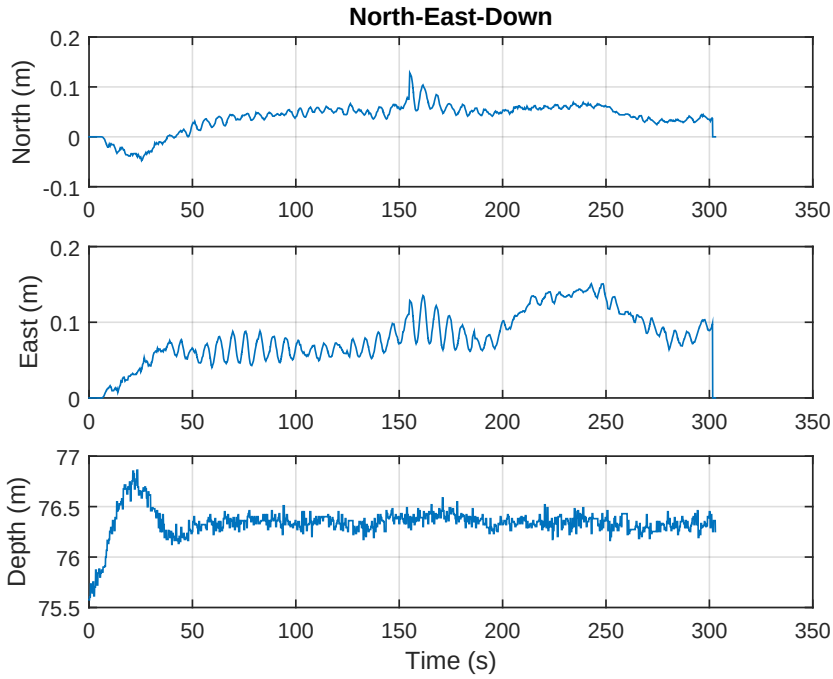

(a) Position.

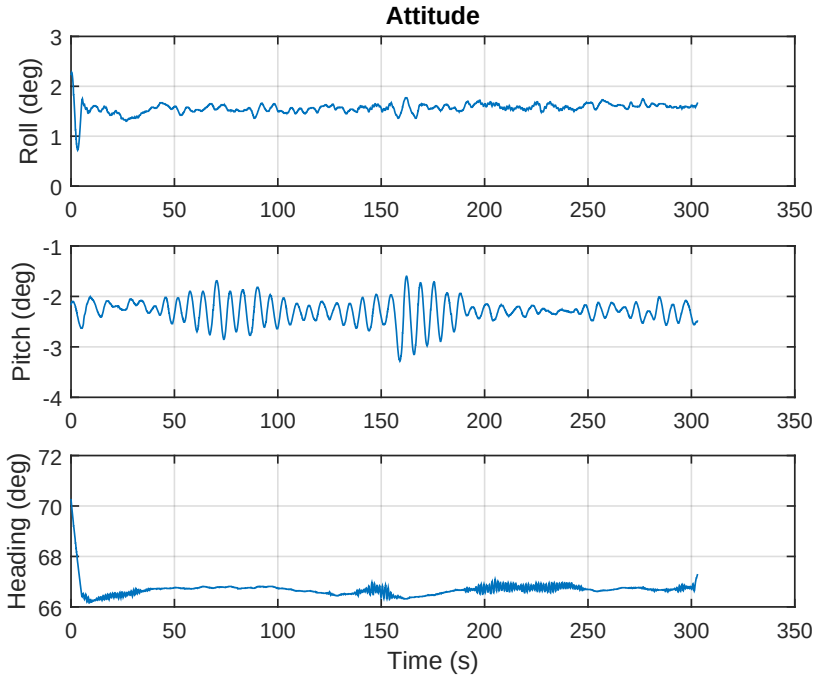

(b) Attitude.

Figure 8.6: Station keeping using PD control only to verify the feedback gains. (Bergen).

Table 8.1: The disturbance observer gains were reduced during full-scale experiments to avoid oscillatory behavior. (Bergen).

$\mathbf{K}_{dob}$	Value
From HIL tests	diag{1000, 1000, 1000, 1000, 1000, 1000}
Reduced	diag{400, 400, 100, 600, 600, 400}

The results of using the disturbance observer were so good that adaptation was kept off for most of the tests. A comparison can still be found in Section 8.5.4.

Depth control was still not satisfactory despite the new gains in the disturbance observer, and actually worked better without integral action. Depth control using the original and reduced gains can be found in Figure 8.7.

Figure 8.8a gives a North-East plot of the ROV during station keeping when using the disturbance observer. To put this result in perspective, the data is combined with the outline of the ROV at one instance in time in Figure 8.8b. The ROV successfully stabilized at the origin, keeping the North-East position within 10 square centimeters for several minutes. See also the video file `stationkeeping.mov` in the supplemented material for a recording from the onboard cameras, showing station keeping in action from this test.

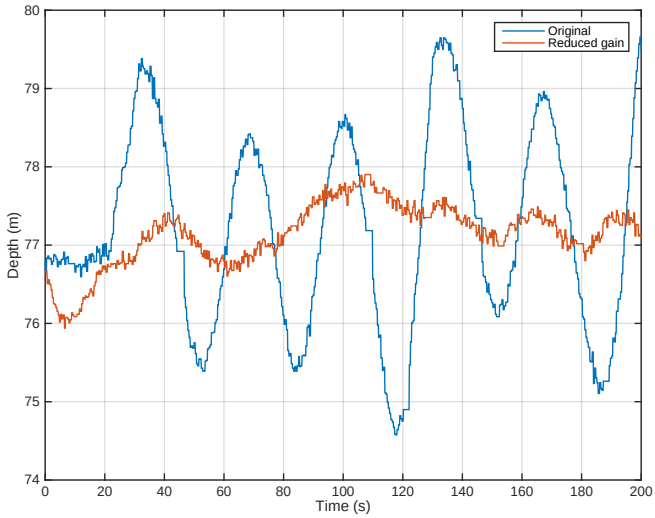

Figure 8.7: Depth control during first test of station keeping in Bergen. Severe oscillations when using gains from HIL tests. Cutting back on the gains reduced the amplitude, but the frequency of oscillation is almost the same.

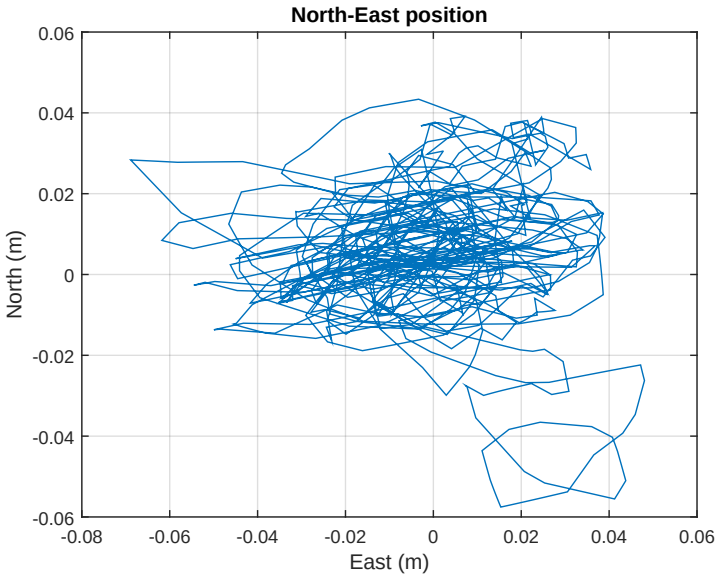

(a) North-East plot using station keeping.

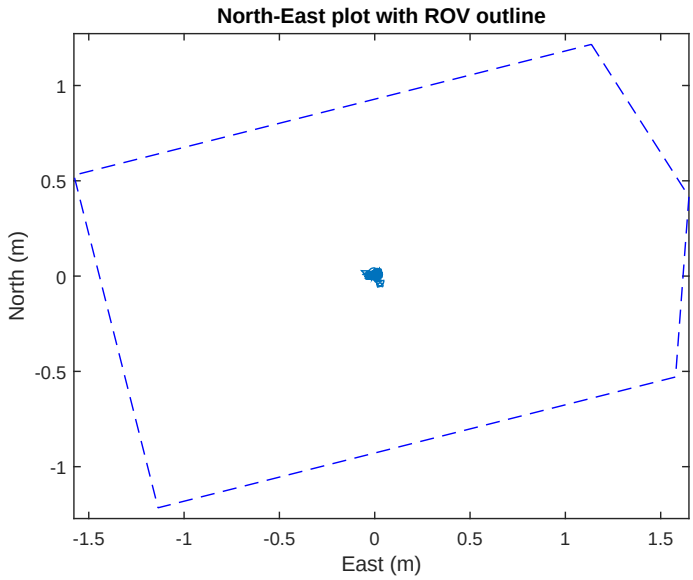

(b) ROV outline on top of North-East plot.

Figure 8.8: North and East positions with station keeping activated in Bergen.

8.5 Day 3 - Mongstad, docks

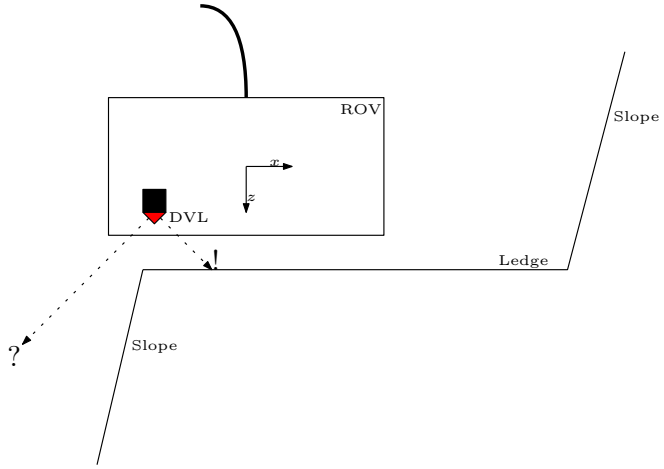

Figure 8.9: Loosing bottom lock on ledge in Mongstad.

On the third day, the ship sailed to Mongstad where the tests were continued with the ship docked at Mongstad base. As in Bergen, the position estimate was verified at different depths. The seabed at Mongstad turned out to be more challenging for station keeping. Steep drops, uneven ledges and surrounding slopes made it difficult for the DVL to bottom lock and provide sensible data. The DVL must have valid measrements from at 3 out of 4 beams in order to calculate a solution with maximum seabed slope of 20° (Teledyne RD Instruments 2009).

At times, only a slight change of position would cause the DVL to loose bottom lock. The estimator must then operate in dead reckoning, making it unusable for control in this setup. It was seen in some tests that the ROV would drift e.g. 1 meter without the EKF updating the position. Without an external positioning reference providing more information to navigation system, this is bound to happen from time to time. However, once the DVL was able to provide healthy measurements, the position estimates were in general good and the station keeping system was able to function for up to 15 minutes without problems.

8.5.1 Improving depth measurement

Depth control was not satisfactory on the first day of testing and spikes had been observed on the input to the vertical thrusters. This turned out to be caused by

the sensor setup which was among other relying on slightly unstable measurements from the altimeter. The EKF for depth estimation was set up to use the depth sensor in the TOGSNAV, which turned out to be malfunctioning. It was decided to continue tests using a low-pass filter on the raw depth measurements from an external depth sensor, and calculate the heave velocity by differentiating the filtered output (Fig. 8.10a). The result was considered good enough as the worst spikes had been removed. In retrospect, based on the good results found in Knausgård (2013), it is seen that the external depth sensor should be used together with the EKF for depth estimation. Improved depth control using the low-pass filter can be seen in Figure 8.10b.

8.5.2 Results for roll, pitch and yaw

The pilot commented on the first day of testing that the ROV was heavier than usual. About 10-15 kg was removed to make the vehicle more neutral in water, but the balance was shifted, causing it to pitch about -12 degrees when left uncontrolled. Figure 8.11 shows how the integral action of the disturbance observer levels out the ROV by regulating the roll and pitch angles to zero. Good control of heading is also seen, where the deviation from the setpoint is kept within $\pm$ 0.5 degrees for about 5 minutes.

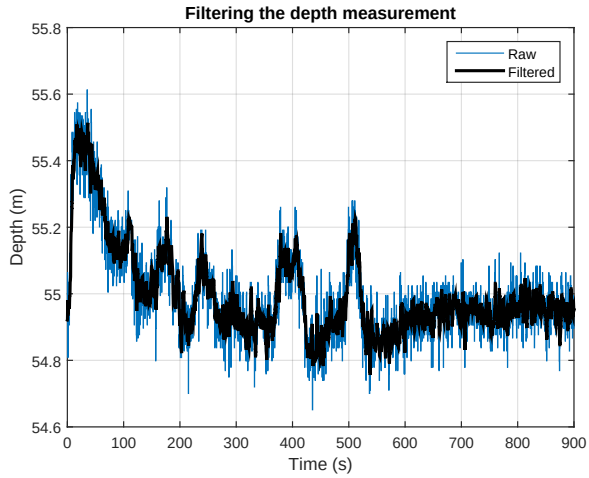

(a) Applying low-pass filter

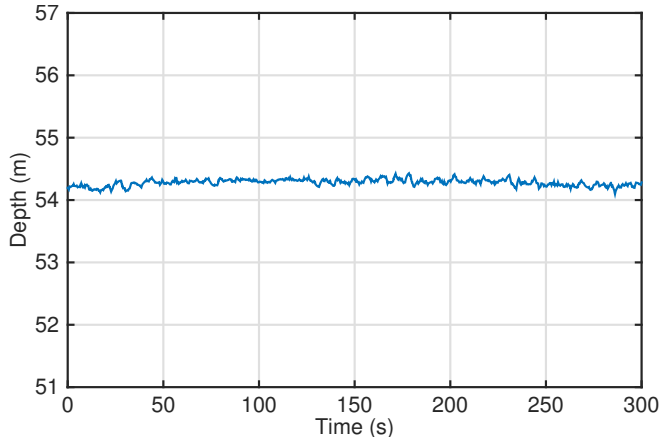

(b) Improved depth control

Figure 8.10: Raw and filtered depth measurement. Note that the filtered plot is drawn with a thicker line to enhance visibility. Depth control improved after changing the sensor setup. (Mongstad)

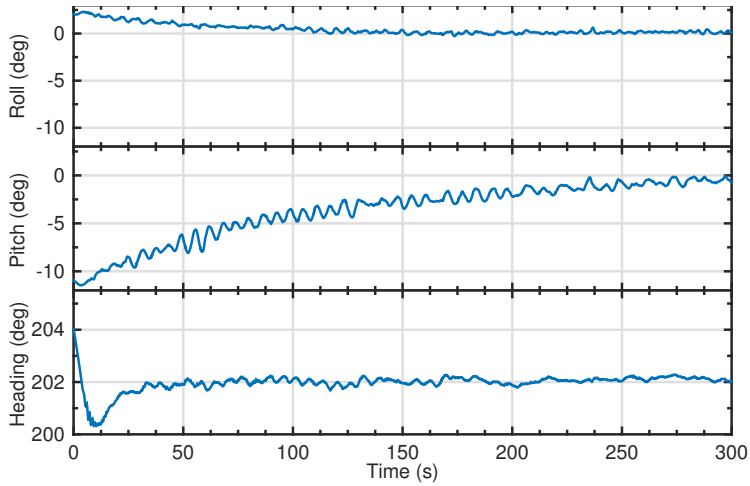

Figure 8.11: The ROV is leveled by the disturbance observer. (Mongstad).

8.5.3 Low speed maneuvering using joystick

With semi-automatic mode activated, the pilot could position the ROV with 4 degrees of freedom, namely North, East, Down and Yaw. Figure 8.12 shows the estimated and desired horizontal position when moving sideways.

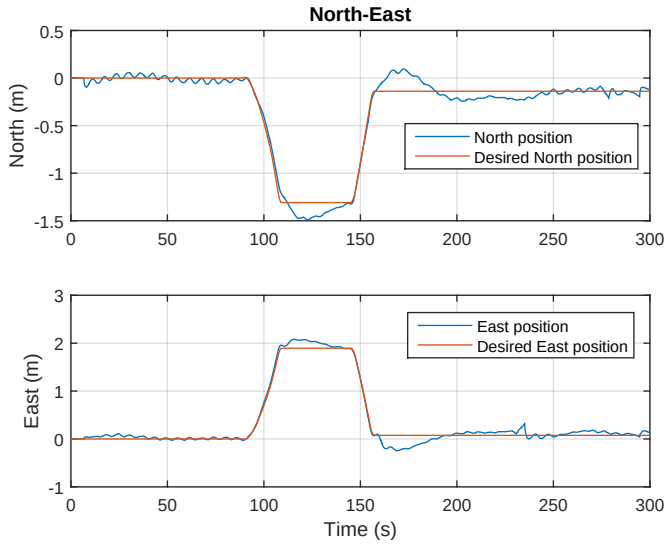

Figure 8.12: Using joystick to move the ROV sideways. (Mongstad).

Input from the users of the system is highly valuable. When using the DP system for the first time, pilot Erlend Apeland made the following comment:

> *"It does not at all feel like I'm the flying the ROV, but simply moving it. And it feels natural."*

During the pure sideways movement, heading was changing about 2 degrees, as can be seen in Figure 8.13 around 100 and 150 seconds. This suggests that the moment arms used in the thrust configuration matrix should be adjusted to correct for this unwanted yaw moment. Since the heading is increasing when moving in negative sway direction, it may seem as if the moment arm extending from CG to the aft horizontal thrusters, is larger than the arm extending forward. I.e., $l_6 > l_4$ in Figure 3.5a in Section 3.5 in Chapter 3.

Figure 8.14 shows the heading angle when the pilot rotates toward 360 degrees to verify if the discontinuity around 360 degrees is handled well by the controller.

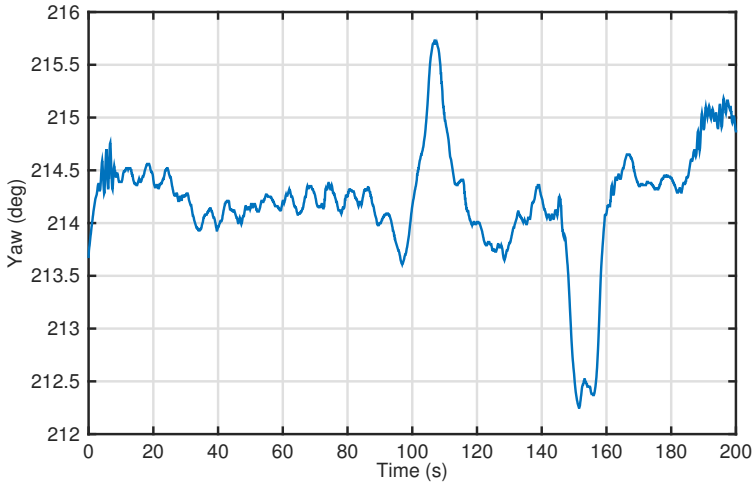

Figure 8.13: Heading is changing with about 2 degrees when moving sideways. This suggests to update the thrust configuration matrix to account for the unwanted yaw-moment. (Mongstad).

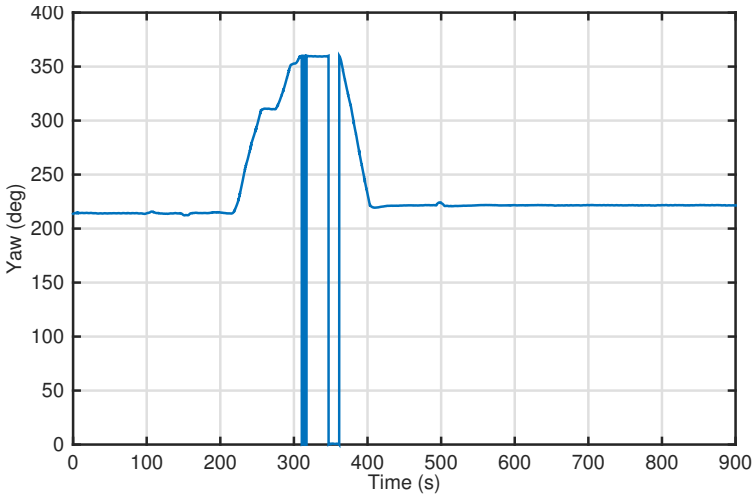

Figure 8.14: Using joystick to control the heading to 360 degrees. (Mongstad).

See also the video files `joystick.mov` and `joystick_animation.mp4` in the supplemented material for recordings from the onboard cameras and an animation based on experimental data from this tests.

8.5.4 Turning on adaptation

After several successful tests using only the disturbance observer for integral action, adaptation was turned on to see if the results could be improved. The results are compared in Figure 8.15.

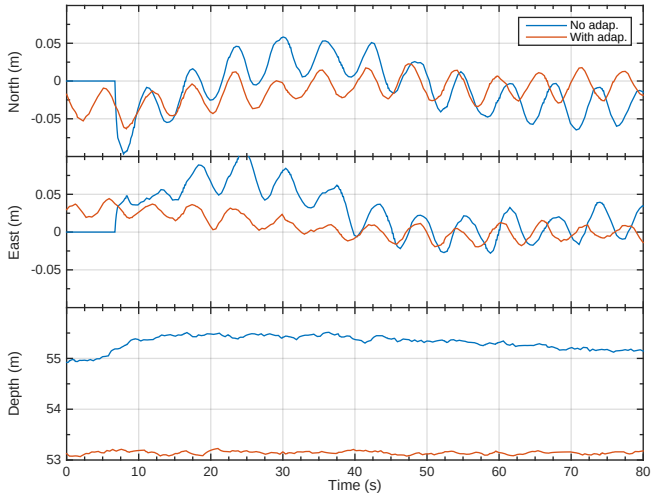

Figure 8.15: Comparing station keeping functionality when turning on adaptation. (Mongstad).

8.5.5 Changing damping characteristics in the DOB

The nonlinear damping characteristics modeled by $\mathbf{D}(\boldsymbol{\nu})$ stems from drag tests performed in Knausgård (2012), and is used in the disturbance observer. The idea is that the observer will be better at separating disturbances from dynamic motions by having an accurate model of the dynamics of Merlin WR200. This is seen from rearranging the equations of motion (3.36) from Chapter 3:

$$\hat{\boldsymbol{\tau}}_d = \mathbf{M}\dot{\boldsymbol{\nu}} + \mathbf{D}(\boldsymbol{\nu})\boldsymbol{\nu} - \boldsymbol{\tau} \tag{8.1}$$

If the coefficients of $\mathbf{D}(\boldsymbol{\nu})$ are changed, the estimated disturbance $\hat{\boldsymbol{\tau}}_d$ is expected to behave differently. Station keeping was performed when all coefficients were increased and decreased according to Table 8.2. Figure 8.16 compares East, depth and heading when using the new values.

Table 8.2: The original and altered damping coefficients used during station keeping in Mongstad. The new values were chosen arbitrarily.

Damping matrix	Value
Original	diag(1321, 2525, 2525, 192, 192, 192)
Increased	diag(2000, 3000, 3500, 1000, 1000, 1000)
Decreased	diag(300, 350, 400, 10, 10, 50)

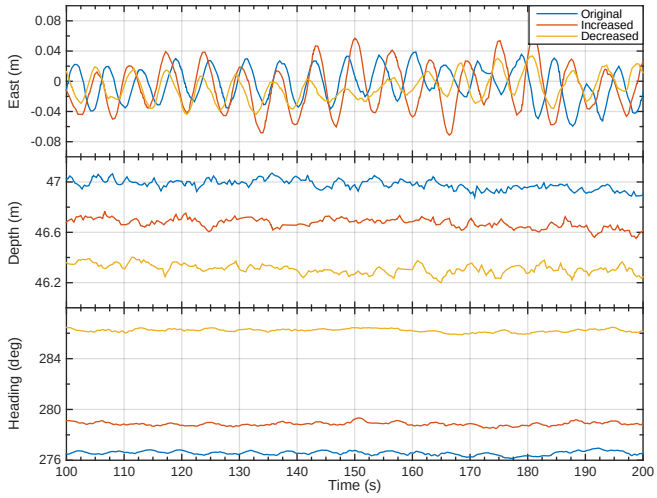

Figure 8.16: East, depth and heading from station keeping using the original, increased and decreased damping coefficients. (Mongstad).

8.6 Discussion

The results from full-scale experiments show very encouraging results. Making thorough preparations was the major key to success, hereunder the HIL tests. This meant there were no issues with implementation bugs during tests, and significantly reduced the time needed for tuning gains.

Station keeping

Despite the ROV being stable, one should tune the feedback gains $\mathbf{K}_1$ and $\mathbf{K}_2$ to improve the results. For instance, surge and sway positions in Figure 8.6 oscillate with periods of 6 seconds, which seem to excite the natural frequency of pitch (Section 3.4.1 in Chapter 3). Furthermore, Thor I. Fossen (2011, p.137) suggest to include linear damping in the model to avoid oscillations in station keeping applications. The model of Merlin includes only nonlinear damping (Section 3.4.1 in Chapter 3), which is used in the formulation of the disturbance observer. Adding a nonzero term may remove oscillations. In the future, the HMI should include a tuning option to scale $\mathbf{K}_1$ and $\mathbf{K}_2$ using two separate parameters λ_1, λ_2, assuming that the mutual ratio among the elements of the matrices are satisfactorily tuned. This may be necessary as Merlin WR200 is often equipped with tools that alter the dynamic behavior.

The proposed station keeping system successfully stabilized all 6 degrees of freedom for several minutes. The horizontal position of the ROVs center was kept within 10 cm $\times$ 10 cm (Fig. 8.8a), which is considered good taking into account the ROV footprint of 2.8 m $\times$ 1.8 m. Furthermore, roll and pitch was successfully regulated to zero degrees and satisfactory heading control was seen in all tests (Fig. 8.11, 8.13 and 8.16). Figure 8.6a show constant deviations from the North and East setpoints of 0 meters when there was no integral action, suggesting some ocean current disturbing the ROV. It was however not possible to test the DP system in rougher conditions.

Depth control

Depth control turned out to be more difficult compared to simulations. The ROV showed large oscillations with period 35 seconds when using the gains from HIL-tests. As previously mentioned, the ROV was heavier than usual, but the exact weight is not known. A heavier ROV should result in a lower natural frequency of the heave dynamics. Assuming a mass of 3250 kg gives an expected period of 24.5 seconds (Equation (3.30) in Chapter 3, Section 3.4.1), which is in range of the observed value. When using the gains from HIL tests, it seem as if the bandwidth of the control system was close to that of the ROV. The amplitude of oscillations was being damped out when decreasing the gains (Fig. 8.7), however still oscillating with almost the same frequency. Stable depth was first seen after modifying the sensor setup to obtain smooth and stable heave velocity measurements (Fig 8.10b). No data exist from the applied force in heave, but it is assumed to be smoother as it did not further cause oscillations in depth.

Velocity measurements

Due to limited logging capacity, no velocity measurements are available from these sea trials. However, since the exact same TOGSNAV sensor and navigation system was used in Knausgård (2013), velocity measurements from sea trials therein are shown in Figure 8.17. Thus, it is clear that the velocity measurements from the DVL are tenfolds better than measurements in HIL-tests, which was found by differentiating the position measurements. Despite this significant difference, only minor changes had to be made for the controller gains when applying the control law for a real Merlin WR200.

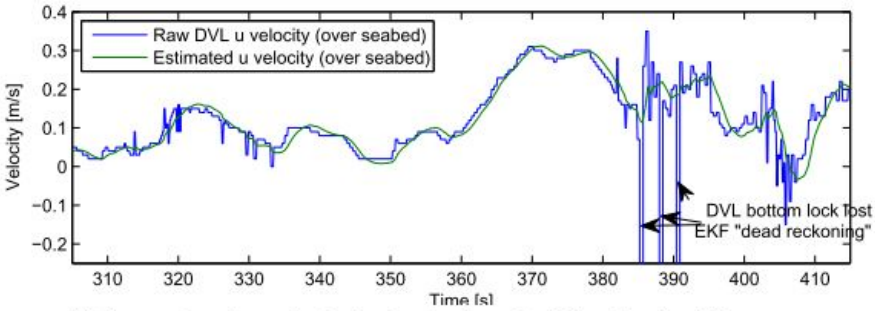

(a) Raw and estimated velocity in u body-seabed direction for drift test tour

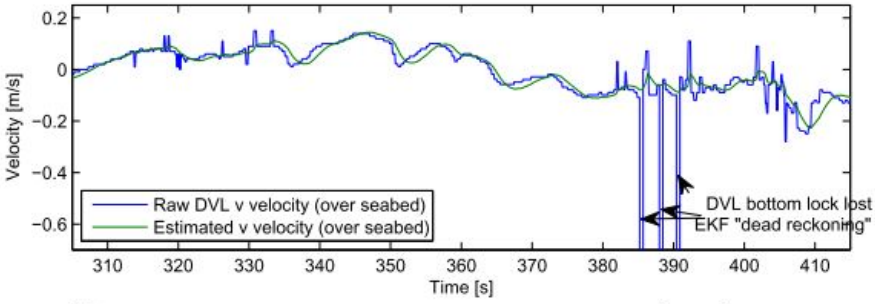

(b) Raw and estimated velocity in v body-seabed direction for drift test tour

Figure 8.17: Measured and estimated horizontal velocities from sea trials performed in Knausgård (2013, Figure 9.4, p.93)

Maneuvering

Low-speed maneuvering using the joystick worked well. One can see from Figure 8.12 that the ROV overshoots the desired postion with about 20 centimeters when releasing the stick, but the pilot commented that the stop feels instantaneous. The system aims at braking the ROV and enables position control once the velocity is below a certain threshold or if braking is taking too long (e.g. cannot break due to large current). To reduce overshoot, one could tune the velocity threshold in the reference model. It would be interesting to verify the functionality of the joystick reference model in waters with more current, which should be the aim of tests in the future. As mentioned in Section 5.1, pilots are not in need of such a system in calm waters.

Changing damping coefficients in the disturbance observer

Figure 8.16 show that increasing the coefficients gives a slightly larger amplitude in the estimated East position, whereas having virtually no effect in heave and yaw. The disturbance observer seem to be overcompensating in surge and sway when using the increased coefficients, and should be tuned through $\mathbf{K}_{dob}$. It does not appear to be necessary to apply accurate drag coefficients, but they should probably be chosen conservatively. Either way, one may tune the gain $\mathbf{K}_{dob}$ for better performance. One should not base conclusions on these tests alone, but conduct the same test in a more challenging environment to see the effect in full. It is however promising that the system at this stage seem to be robust with respect to these parametric uncertainties.

Using adaptation

Figure 8.15 suggest that using adaptation does not significantly improve the station keeping capabilities compared to when only using the disturbance observer. This can also be seen in the simulation study of Section 7.6 in Chapter 7, which was inspired by this observation. This may suggest that adaptation is superfluous in the implementation, and that the observer alone will suffice.

Chapter 9

Conclusion and Recommendations

This thesis has presented a dynamic positioning system able to successfully stabilize all 6 degrees of freedom of the Merlin WR200 work-class ROV. The proposed full-DOF control system exceeds the capabilities of the current system, which only feature automatic depth and heading control. Extensive tests were carried out using the high-fidelity Merlin WR200 simulator at IKM Subsea Solutions AS, Bryne. The control system was further implemented on existing hardware and verified in a full-scale experiment, showing successful station keeping with stabilization in 6 DOF. Furthermore, the proposed joystick velocity referece module for low-speed maneurvering in closed-loop control, was well received by a former industrial ROV pilot.

The main objective of this thesis has been to build upon existing work on DP for Merlin WR200. A navigation system was developed for Merlin in Knausgård (2013) which was applied in the full-scale experiment without need of tuning. Ohrem (2015) developed a robust, parameter independent control system which forms the basis of the control system presented in this thesis. The controller of Ohrem (2015) was extended to also control roll and pitch. Moreover, a disturbance observer was introduced to account for tether-induced motions, unmodelled dynamics and ocean current. In addition, the controller was designed to compensate for the slow response in the thrusters. Robust behavior was seen in simulations where station keeping was functional with current speeds up to 2.5 knots, at which point two horizontal thrusters were working at full speed.

The basic principle of the disturbance observer is to balance Newton's second law. The idea is that a motion that do not correspond to the control action or the system dynamics, is caused by a disturbing force. Thus, by balancing the equations of motion, robust integral action is obtained. This is in contrast to the parameter adaptation scheme, which solely rely on feedback from the states. The observer takes into account the current control action, and adjust its output to stop unwanted movements of the ROV. It is not necessary with an exact mathematical model for the observer to work (Mohammadi et al. 2013), which was briefly tested in sea trials where the quadratic damping coefficients were both increased and decreased without any significant effect. However, more tests should be done in this regard. Using both adaptation and disturbance observer at the same time is not a problem in theory, and worked well in both simulations and in field experiments. However, for the sake of robustness, it is viewed as a better option to use integral action from only one source. This will also simplify the implementation of the control system.

A ramp filter in the frequency converters introduce a delay in the control loop. To model this, a simple, linear differential equation was applied. Simulation results indicate that the proposed compensation is ineffective as the influence on the control action is minimal. One should thus consider using a more accurate model in the future, or neglect the delay in the control design. The latter option is suggested, which will simplify the controller and the implementation.

A low-order joystick velocity reference model was suggested to reduce phase lag when used in closed-loop control. The aim was to give the operator the perception of being more in control, compared to when using models of higher order (Knausgård 2013; Dukan 2014). Simulations were performed with 2 knots of current where the author positioned the ROV with ease. Using the joystick, it is possible to move the ROV in three dimensions and change heading. All DOFs are governed by automatic control, by taking desired trajectories from the joystick module. It is the belief of the author that the proposed system will be a useful tool in waters with significant current, where manual control is challenging. The proposed system was also appreciated by a former industrial pilot, who took it in use without further instructions during the field experiment.

Finally, LOS guidance for fully-actuated vehicles was demonstrated using the Merlin WR200 simulator by tracking waypoints. Using a guidance law that utilize full actuation of the vehicle, it is possible to avoid the modifications done in Ohrem (2015) in order to return along an already driven path. Although successfully applied, more work should be done on this topic.

Recommendations

It is highly recommended to continue this project centralized around the Merlin WR200 simulator. Having unlimited access throughout this project, was the major key to success.

Having a functional control system, it is suggested to shift focus in the continuation of this project. Guidance should be the main topic. One should continue working on reference models for A to B moves and incorporate the solutions in an intuitive way in the HMI in collaboration with the pilots. Using the LOS law for fully actuated vehicles, path following should be explored in more detail, and verified using the simulator. Guidance in the presence of currents should be emphasized. Moreover, the proposed joystick velocity reference model should be tested more extensively in the field. It should be improved based on feedback from the pilots, or replaced by a better system.

A new thruster model was presented in this thesis, showing a closer fit with experimental data. It is suggested to continue this work, by performing more extensive experiments as in Ludvigsen and Ødegaard (2005), to obtain a more versatile model. Focus should also be on improving the thrust allocation algorithm, by considering loss of thrust and thruster-thruster-interaction.

Although showing very good behavior, the navigation system should be improved according to the suggestions of Knausgård (2013) and per the advice given in Appendix D in this thesis.

Bibliography

Antonelli, G. et al. (2001). "A novel adaptive control law for autonomous underwater vehicles." In: *International Conference on Robotics & Automation*. Seoul: IEEE, pp. 448–452.

– (2003). "A novel adaptive control law for underwater vehicles." In: *IEEE Transactions on Control Systems Technology* 11.2, pp. 221–232.

Børhaug, Even, A. Pavlov, and Kristin Y. Pettersen (2008). "Integral LOS control for path following of underactuated marine surface vessels in the presence of constant ocean currents." In: *Proceedings of the IEEE Conference on Decision and Control*, pp. 4984–4991.

Breivik, Morten and Thor I. Fossen (2005). "Principles of guidance-based path following in 2D and 3D." In: *Proceedings of the 44th IEEE Conference on Decision and Control, and the European Control Conference, CDC-ECC '05* 2005, pp. 627–634.

Brown, Robert Grover and Patrick Y.C. Hwang (2012). *Introduction to Random Signals and Applied Kalman Filtering*. 4th. John Wiley & Sons, Inc., p.146 and 165.

Caharija, Walter et al. (2012). "Integral LOS Guidance for Horizontal Path Following of Underactuated Autonomous Underwater Vehicles in the Presence of Vertical Ocean Currents." In: *2012 American Control Conference*, pp. 5427–5434.

Candeloro, M et al. (2012). "Observers for dynamic positioning of ROVs with experimental results." In: *IFAC Proceedings Volumes (IFAC-PapersOnline)*. Vol. 9, pp. 85–90.

Carlton, J.S. (1994). *Marine Propellers and Prolusion*. Oxford: Butterworth-Heinemann.

Chen, W.-H. et al. (2000). "A nonlinear disturbance observer for robotic manipulators." In: *IEEE Transactions on Industrial Electronics* 47.4, pp. 932–938.

Christ, Robert D. and Robert L. Wernli (2014). *The ROV Manual*. 1st ed. Butterworth-Heinemann, pp. 327–368.

Dukan, Fredrik (2014). "ROV Motion Control Systems." PhD thesis. NTNU.

Dukan, Fredrik, Martin Ludvigsen, and Asgeir J. Sørensen (2011). "Dynamic positioning system for a small size ROV with experimental results." In: *OCEANS 2011 IEEE - Spain*.

Egeland, O and J T Gravdahl (2002). *Modeling and Simulation for Automatic Control*. Trondheim: Marine Cybernetics.

Fossen, Thor I. (2000). *Nonlinear passive control and observer design for ships*.

– (2011). *Handbook of Marine Craft Hydrodynamics and Motion Control*. Trondheim: John Wiley & Sons, Ltd.

Fossen, Thor Inge (1991). "Nonlinear Modeling and Control of Underwater Vehicles." PhD thesis. Norwegian University of Science and Technology, p. 39.

Fossen, T.I. and S.P. Berge (1997). "Nonlinear vectorial backstepping design for global exponential tracking of marine vessels in the presence of actuator dynamics." In: *Proceedings of the 36th IEEE Conference on Decision and Control* 5.December, pp. 4237–4242.

Fossen, T.I., M Breivik, and R Skjetne (2003). "Line-of-sight path following of underactuated marine craft." In: *Proceedings of the 6th IFAC MCMC* January 2016, pp. 1–6.

Hadden, Gerry (2012). *Palomares bombs: Spain waits for US to finish nuclear clean-up*. URL: `http://www.bbc.com/news/magazine-18689132` (visited on 12/29/2015).

IKM Subsea (2015). *Merlin Academy*. URL: `http://www.ikm.no/ikm-subsea-norge/merlin-academy` (visited on 12/16/2015).

Ioannou, Petros A. and Jing Sun (2012). *Robust Adaptive Control*. Mineola, New York: Dover Publications, Inc., p. 318.

Khalil, Hassan K. (2000). *Nonlinear Systems*. Third. Pearson Education.

Knausgård, Lasse Muri (2012). "Development of DP System for Merlin WR200 ROV." Master thesis pre-project. NTNU.

– (2013). "Development of DP System for Merlin WR200 ROV." Master thesis. NTNU.

Ludvigsen, Martin and Øyvind Tangen Ødegaard (2005). *Friprøveforsøk med ROV-thruster*. Tech. rep. Trondheim: MARINTEK.

Marine Technology Society (2015). *ROVs - a brief history*. URL: `http://www.rov.org/rov%7B%5C_%7Dhistory.cfm` (visited on 12/29/2015).

Mohammadi, a. et al. (2013). "Nonlinear disturbance observer design for robotic manipulators." In: *Control Engineering Practice* 21.3, pp. 253–267.

Mukherjee, Koena, I. N. Kar, and RKP Bhatt (2015). "Disturbance observer based tracking controller for an autonomous underwater vehicle." In: *2015 IEEE Underwater Technology (UT)*, pp. 1–6.

Ohrem, Sveinung Johan (2015). "Development of a Dynamic Positioning System for Merlin WR 200 ROV." Master thesis. NTNU.

Patompak, Pakpoom and Itthisek Nilkhamhang (2012). "Adaptive backstepping sliding-mode controller with bound estimation for underwater robotics vehicles." In: *Electrical Engineering/Electronics, Computer, Telecommunications and Information Technology (ECTI-CON), 2012 9th International Conference on*. Phetchaburi: IEEE, pp. 1–4.

Poissonnet, Cyril (2013). "Deep Water MiniROVs and Delivery Systems." In: *Oceans 2013 San Diego*.

Prabhakar, S. and B. Buckham (2005). "Dynamics modeling and control of a variable length remotely operated vehicle tether." In: *Proceedings of OCEANS 2005 MTS/IEEE*. Vol. 2. Washington, DC: IEEE, pp. 1255–1262.

Price, W. G. and R. E. D. Bishop (1974). *Probabilistic theory of ship dynamics*. London: Chapman and Hall.

Rebikoff, D (1985). "Large area low-cost programmed free unmanned vehicle design." In: *Unmanned Untethered Submersible Technology, Proceedings of the 1985 4th International Symposium on*, pp. 23–29.

Sariyildiz, Emre and Kouhei Ohnishi (2015). "Stability and Robustness of Disturbance-Observer-Based Motion Control Systems." In: *IEEE Transactions on Industrial Electronics* 62.1, pp. 414–422.

Selvakumar, J Manecius and T Asokan (2015). "Station keeping control of underwater robots using disturbance force measurements." In: *Journal of Marine Science and Technology*, pp. 1–16.

Sørensen, Asgeir J (2013). *Marine Control Systems Propulsion and Motion Control of Ships and Ocean Structures Lecture Notes*. Trondheim.

Srisamosorn, Veerachart, Pakpoom Patompak, and Itthisek Nilkhamhang (2013). "A Robust Adaptive Control Algorithm for Remotely Operated Underwater Vehicle." In: *SICE Annual Conference (SICE), 2013 Proceedings of*. Vol. 2. 2. Nagoya: IEEE, pp. 655–660.

Steinke, Dean M. and Bradley J. Buckham (2005). "A Kalman filter for the navigation of remotely operated vehicles." In: *Proceedings of MTS/IEEE OCEANS, 2005* 2005.1 250, pp. 1–8.

Svendby, Eirik (2007). "Robust control of ROV / AUVs." Master thesis.

Teledyne RD Instruments (2009). *Navigator Doppler Velocity Log Technical Manual*.

The Society of Naval Architects and Marine Engineers (1950). "Nomenclature for Treating the Motion of a Submerged Body Through a Fluid." In: *Technical and Research Bulletin* 1.

Wei, Yanhui et al. (2015). "Adaptive Integral Back-stepping Controller Design for ROV with Disturbance Observer." In: *Proceedings of 2015 IEEE International Conference on Mechatronics and Automation*, pp. 1106–1110.

Zhu, Kangwu and Linyi Gu (2011). "A MIMO nonlinear robust controller for work-class ROVs positioning and trajectory tracking control." In: *2011 Chinese Control and Decision Conference (CCDC)*, pp. 2565–2570.

Appendix A

Stability Analysis

A.1 Preliminaries

To prove stability for the system (3.35)-(3.37) with the controller (4.54), one may use a special case of Barbălat's lemma which is re-stated below (Ioannou and Sun 2012, Lemma 3.2.5):

Lemma A.1. *If $f, \dot{f} \in \mathcal{L}_\infty$ and $f \in \mathcal{L}_p$ for some $p \in [1, \infty]$, then $f(t) \to 0$ as $t \to 0$.*

where the $\mathcal{L}_p$ norm for the piecewise continuous, time-varying vector $\mathbf{x}(t)$ is defined as

$$\|\mathbf{x}(t)\|_{\mathcal{L}_p} = \left(\int_0^\infty \mathbf{x}(\tau)^\top \mathbf{x}(\tau) \right)^{1/p} \mathrm{d}\tau < \infty \tag{A.1}$$

If this Lemma can be applied to the reduced state space $\{\tilde{\boldsymbol{\eta}}_p, \mathbf{s}, \mathbf{z}\}$, then these states will be asymptotically stable. The proof will treat the various signals in the control loop and hence a short overview is convenient:

$$\tilde{\boldsymbol{\eta}}_p = \mathbf{P}(\psi)^\top \big(\boldsymbol{\eta} - \boldsymbol{\eta}_d\big) \tag{A.2}$$
$$\dot{\tilde{\boldsymbol{\eta}}}_p = \tilde{\boldsymbol{\nu}} + r\mathbf{S}\tilde{\boldsymbol{\eta}}_p \tag{A.3}$$
$$\tilde{\boldsymbol{\nu}} = \boldsymbol{\nu} - \boldsymbol{\nu}_d \tag{A.4}$$
$$\boldsymbol{\nu}_v = \boldsymbol{\nu}_d - \mathbf{K}_1\tilde{\boldsymbol{\eta}}_p \tag{A.5}$$
$$\dot{\boldsymbol{\nu}}_v = \dot{\boldsymbol{\nu}}_d - \mathbf{K}_1\tilde{\boldsymbol{\nu}} \tag{A.6}$$
$$\mathbf{s} = \boldsymbol{\nu} - \boldsymbol{\nu}_v \tag{A.7}$$
$$\mathbf{z} = \mathbf{B}\mathbf{u} - \mathbf{B}\mathbf{u}_v \tag{A.8}$$
$$\mathbf{B}\mathbf{u}_v = \boldsymbol{\phi}(\dot{\boldsymbol{\nu}}_v, \boldsymbol{\nu}_v)^\top \hat{\boldsymbol{\theta}} - \hat{\boldsymbol{\tau}}_d - \tilde{\boldsymbol{\eta}}_p - \mathbf{K}_2\mathbf{s} \tag{A.9}$$
$$\mathbf{u}_c = \mathbf{u} + \mathbf{T}\mathbf{B}^\dagger \big(\mathbf{B}\dot{\mathbf{u}}_v - \mathbf{s} - \mathbf{K}_3\mathbf{z}\big) \tag{A.10}$$
$$\dot{\hat{\boldsymbol{\tau}}}_d = -\mathbf{L}\mathbf{x}_{dob} + \mathbf{L}\big(\mathbf{D}(\boldsymbol{\nu})\boldsymbol{\nu} - \mathbf{B}\mathbf{u}_v - \mathbf{K}_{dob}\dot{\boldsymbol{\nu}}\big) \tag{A.11}$$
$$\dot{\hat{\boldsymbol{\theta}}} = -\boldsymbol{\Gamma}\boldsymbol{\phi}\mathbf{s} \tag{A.12}$$

A.2 Analysis

Since $\dot{V}_3 \leq 0$ in Equation (4.55), the Lyapunov function candidate is a non-increasing function of time and therefore $V_3 \in \mathcal{L}_\infty$. Since V_3 is also positive definite, the signals $\tilde{\boldsymbol{\eta}}(t)_p, \mathbf{s}(t), \mathbf{z}(t), \tilde{\boldsymbol{\theta}}(t) \in \mathcal{L}_\infty$ as well. These signals are *bounded*. Moreover, an upper limit V_∞ exists:

$$\lim_{t\to\infty} V_3(\tilde{\boldsymbol{\eta}}(t)_p, \mathbf{s}(t), \mathbf{z}(t), \tilde{\boldsymbol{\theta}}(t), t) = V_\infty \tag{A.13}$$

Similarly, the initial value is $V_0 = V_3\big(\tilde{\boldsymbol{\eta}}(0)_p, \mathbf{s}(0), \mathbf{z}(0), \tilde{\boldsymbol{\theta}}(0), 0)\big)$. From (4.55)

$$\int_0^\infty \Big(\tilde{\boldsymbol{\eta}}_p^T\mathbf{K}_1\tilde{\boldsymbol{\eta}}_p + \mathbf{s}^T\big(\mathbf{D}(\boldsymbol{\nu}) + \mathbf{K}_2\big)\mathbf{s} + \mathbf{z}^\top\mathbf{K}_3\mathbf{z}\Big)\mathrm{dt} = V_0 - V_\infty < \infty \tag{A.14}$$

which means that $\tilde{\boldsymbol{\eta}}(t)_p, \mathbf{s}(t), \mathbf{z}(t) \in \mathcal{L}_2$.

The reference signals $\boldsymbol{\eta}_d, \boldsymbol{\nu}_d$ are smooth and continuously differentiable and are therefore bounded by design.

The time derivative of the position error (A.3) is bounded since $\mathbf{s}$ is bounded (remember that $\mathbf{s}$ includes r in $\boldsymbol{\nu}$), $\mathbf{S}$ is a constant bounded matrix and the position error (A.2) is bounded. Thus, the position error $\tilde{\boldsymbol{\eta}}_p(t)$ is asymptotically stable.

Since $\tilde{\boldsymbol{\theta}} \in \mathcal{L}_\infty$, then $\dot{\tilde{\boldsymbol{\theta}}} \to \mathbf{0}$ as $t \to \infty$. This suggest that $\boldsymbol{\phi} \in \mathcal{L}_\infty$ since $\mathbf{s}, \boldsymbol{\Gamma} \in \mathcal{L}_\infty$. Then the arguments $\dot{\boldsymbol{\nu}}_v, \boldsymbol{\nu}_v$ of $\boldsymbol{\phi}$ are bounded signals.

The vehicle acceleration $\dot{\boldsymbol{\nu}}$ is bounded because the forces and moments acting on the craft are bounded and the input $\mathbf{Bu} \in \mathcal{L}_\infty$ because $\mathbf{z} \in \mathcal{L}_\infty$, which is obvious since the control law was designed to stabilize the system. Thus, $\dot{\mathbf{s}} = \dot{\boldsymbol{\nu}} - \dot{\boldsymbol{\nu}}_{\boldsymbol{v}} \in \mathcal{L}_\infty$ and the virtual velocity error $\mathbf{s}(t)$ is also asymptotically stable.

Finally, the time derivative of (A.8) is given by

$$\dot{\boldsymbol{z}} = \mathbf{B}\mathbf{T}^{-1}(\mathbf{u}_c - \mathbf{u}) - \mathbf{B}\big(\dot{\boldsymbol{\phi}}^\top \hat{\boldsymbol{\theta}} + \boldsymbol{\phi}^\top \dot{\hat{\boldsymbol{\theta}}} - \dot{\hat{\boldsymbol{\tau}}}_d - \tilde{\boldsymbol{\eta}}_p - \mathbf{K}_2\mathbf{s}\big) \tag{A.15}$$

The commanded input $\mathbf{u}_c$ is bounded since all signals in the control law (A.10) are bounded. The time derivative of the regressor $\boldsymbol{\phi}$ depends on $\ddot{\boldsymbol{\nu}}_v$ which is bounded since $\dot{\boldsymbol{\nu}}$ is bounded. The signal $\dot{\hat{\boldsymbol{\tau}}}_d$ is bounded since the input signals to the disturbance observer (A.11) are bounded, and since the state $\mathbf{x}_{dob}$ of the filter is initialized to a finite value. Thus all signals of (A.15) are bounded and hence $\mathbf{z}(t)$ is asymptotically stable.

Note that the last term in (A.3) is assumed zero when calculating (A.6) as the yaw rate r is small during station keeping and dynamic positioning, but for the sake of argument, it is seen to be bounded as (A.3) and $\dot{\boldsymbol{\nu}}$ are bounded.

To conclude, the signals $\tilde{\boldsymbol{\eta}}_p, \mathbf{s}, \mathbf{z}$ are asymptotically stable and the parameter estimate $\hat{\boldsymbol{\theta}}$ is bounded. It can not be proved that the estimated parameter vector $\hat{\boldsymbol{\theta}}$ converges to its true counterpart $\boldsymbol{\theta}$.

Appendix B

Simulation Results - Raw Data

This Appendix contains the raw data obtained when applying the IAE, RMS and MMADU performance measures.

B.1 Comparing the controllers

This section contains presents the obtained data from simulations performed in Section 7.2 in Chapter 7.

B.1.1 Scenario A

Table B.1: Calculated norms and normalized scores from Scenario A (station keeping).

(a) Normalized scores.

Measure	NCS	PCABS-D	PCABS
IAE	0.333	0.667	1.000
RMS	0.333	0.667	1.000
MMADU	1.000	0.810	0.807

(b) Calculated norm.

	IAE			RMS		
DOF	NCS	PCABS-D	PCABS	NCS	PCABS-D	PCABS
$\tilde{N}$	33.8370	68.8520	102.2170	0.1314	0.1910	0.2968
$\tilde{E}$	49.7440	97.4400	136.7310	0.1974	0.2938	0.4504
$\tilde{D}$	4.1760	4.5060	4.9370	0.0147	0.0159	0.0173
$\tilde{\phi}$	0.8259	1.1018	1.9835	0.0025	0.0031	0.0044
$\tilde{\theta}$	2.5036	3.1100	4.4186	0.0064	0.0075	0.0094
$\tilde{\psi}$	1.2372	3.7356	4.1006	0.0031	0.0091	0.0097

B.1.2 Scenario B

Table B.2: Calculated norms and normalized scores from Scenario B (horizontal motion).

(a) Normalized scores.

Measure	NCS	PCABS-D	PCABS
IAE	0.423	0.885	1.000
RMS	0.500	0.808	1.000
MMADU	1.000	0.830	0.959

(b) Calculated norms.

	IAE			RMS		
DOF	NCS	PCABS-D	PCABS	NCS	PCABS-D	PCABS
$\tilde{N}$	13.9126	29.5414	43.9638	0.0365	0.0559	0.0895
$\tilde{E}$	30.8639	34.9449	58.2101	0.0836	0.0798	0.1367
$\tilde{D}$	1.5660	5.8560	2.1010	0.0035	0.0115	0.0042
$\tilde{\phi}$	0.2770	0.9602	1.4057	0.0006	0.0017	0.0025
$\tilde{\theta}$	1.2500	0.9818	3.3448	0.0024	0.0019	0.0057
$\tilde{\psi}$	1.3035	5.2362	4.0812	0.0028	0.0099	0.0082

B.1.3 Scenario C

Table B.3: Calculated norms and normalized scores from Scenario C (rotational motion).

(a) Normalized scores.

Measure	NCS	PCABS-D	PCABS
IAE	0.367	0.633	1.000
RMS	0.464	0.679	1.000
MMADU	1.000	0.652	0.747

(b) Calculated norms.

	IAE			RMS		
DOF	NCS	PCABS-D	PCABS	NCS	PCABS-D	PCABS
$\tilde{N}$	118.5280	130.4560	604.6930	0.3122	0.3280	1.3024
$\tilde{E}$	59.1280	176.2370	177.0240	0.1266	0.3927	0.3569
$\tilde{D}$	5.3130	6.1860	8.0870	0.0104	0.0127	0.0174
$\tilde{\phi}$	0.9750	1.2576	2.5632	0.0021	0.0025	0.0045
$\tilde{\theta}$	2.8024	1.3072	3.7381	0.0051	0.0028	0.0065
$\tilde{\psi}$	8.1085	8.5412	10.7723	0.0188	0.0184	0.0214

B.2 New Control System without Adaptation

The control action of NCS was investigated by removing adaptation from the loop and performing the same simulation Scenarios A-C in Section 7.6 in Chapter 7. The result was compared with full NCS using both adaptation and disturbance observer.

B.2.1 Scenario A

Table B.4: Calculated norms and normalized scores from Scenario A (station keeping).

(a) Normalized scores.

Measure	Full	No adap.
IAE	0.667	1.000
RMS	0.667	1.000
MMADU	0.948	1.000

(b) Calculated norms.

	IAE		RMS	
DOF	Full	No adap.	Full	No adap.
$\tilde{N}$	33.4750	31.8000	0.1322	0.1249
$\tilde{E}$	48.9700	49.8380	0.1975	0.1995
$\tilde{D}$	3.1600	3.6960	0.0101	0.0136
$\tilde{\phi}$	0.8525	0.9102	0.0025	0.0026
$\tilde{\theta}$	2.5779	2.6507	0.0063	0.0065
$\tilde{\psi}$	0.9728	1.1695	0.0025	0.0029

B.2.2 Scenario B

Table B.5: Calculated norms and normalized scores from Scenario B (rotational motion).

(a) Normalized scores.

Measure	Full	No adap.
IAE	1.000	1.000
RMS	1.000	1.000
MMADU	0.900	1.000

(b) Calculated norms.

	IAE		RMS	
DOF	Full	No adap.	Full	No adap.
$\tilde{N}$	13.9126	12.4154	0.0365	0.0341
$\tilde{E}$	30.8639	30.6202	0.0836	0.0817
$\tilde{D}$	1.5660	2.4780	0.0035	0.0052
$\tilde{\phi}$	0.2770	0.2823	0.0006	0.0006
$\tilde{\theta}$	1.2500	1.0230	0.0024	0.0020
$\tilde{\psi}$	1.3035	1.4838	0.0028	0.0030

B.2.3 Scenario C

Table B.6: Calculated norms and normalized scores from Scenario C (rotational motion).

(a) Normalized scores.

Measure	Full	No adap.
IAE	0.765	1.000
RMS	0.875	1.000
MMADU	1.000	0.964

(b) Calculated norms.

	IAE		RMS	
DOF	Full	No adap.	Full	No adap.
$\tilde{N}$	118.5280	119.5930	0.3122	0.3154
$\tilde{E}$	59.1280	59.8840	0.1266	0.1269
$\tilde{D}$	5.3130	6.3760	0.0104	0.0125
$\tilde{\phi}$	0.9750	0.9773	0.0021	0.0021
$\tilde{\theta}$	2.8024	2.5089	0.0051	0.0049
$\tilde{\psi}$	8.1085	7.9116	0.0188	0.0185

Appendix C

Code

The Matlab implementation is distributed over the following files which can be found in the digital attachment.

`control.m` Implements the control algorithm

`guidance.m` Implements the guidance system

`pathgen.m` Implements the constant jerk reference model

`stick_fsm.m` Implements the joystick state machine

`stick_speed.m` Implements the joystick velocity reference model

`config.m` Contains parameters necessary to run the program

`merlin_dp.m` The main code using all or some of the modules above

`ikm_udp.m` Sets up a UDP connection to the simulator

`ikm_udp_get_data.m` Extracts data received from simulator

Appendix D

Kalman Filter Implementation

Kalman filters have not been treated in this thesis. However, the navigation system for which the dynamic positioning system currently relies on, contain what is assumed to be a potential issue in the implemented code. A fix was not undertaken in this thesis, as time should rather be spent on testing the newly developed control system. After all, Knausgård (2013) reports very good position and depth estimation. Readers are referred to Knausgård (2013) for details about the navigation system and the filter equations.

D.1 Potential issue

The navigation system is based on an Extended Kalman Filter, a recursive filter which must update an *error covariance matrix* $\boldsymbol{P}_k$ in every iteration (Fig. D.1). The update equation used in the navigation system is given in Equation (D.1)

$$\mathbf{P}_k = (\mathbf{I} - \mathbf{K}_k\mathbf{H}_k)\mathbf{P}_k^- \tag{D.1}$$

which assumes the optimal gain condition. However, it is known to be prone to numerical errors if the filter is running for a long time. Brown and Hwang (2012) suggest to always use the "longer" update equation

$$\mathbf{P}_k = (\mathbf{I} - \mathbf{K}_k\mathbf{H}_k)\mathbf{P}_k^-(\mathbf{I} - \mathbf{K}_k\mathbf{H}_k)^\top + \mathbf{K}_k\mathbf{R}_k\mathbf{K}_k^\top \tag{D.2}$$

which is always valid and with better numerical properties. It is, however, more computationally expensive.

The update equation is currently implemented with the lines of code given below, used in the Kalman filter for North and East position estimation. Similar code is used in the filter for depth and altitude estimation, although with other dimensions for the matrices.

```
(* temp1 = K * H *)
multiplication((4),(8),(8),(4),(0,0),temp1[0],K[0],H[0]);

(* temp2 = I - temp1 = I - K * H *)
substract((8),(8),temp2[0],eye[0],temp1[0]);

(* temp3 = temp2 * P = (I -KH)*P  *)
multiplication((8),(8),(8),(8),(0,0),temp3[0],temp2[0],P[0]);

(* P = temp3 = (I-KH)P *)
copy(P[0],temp3[0]);
```

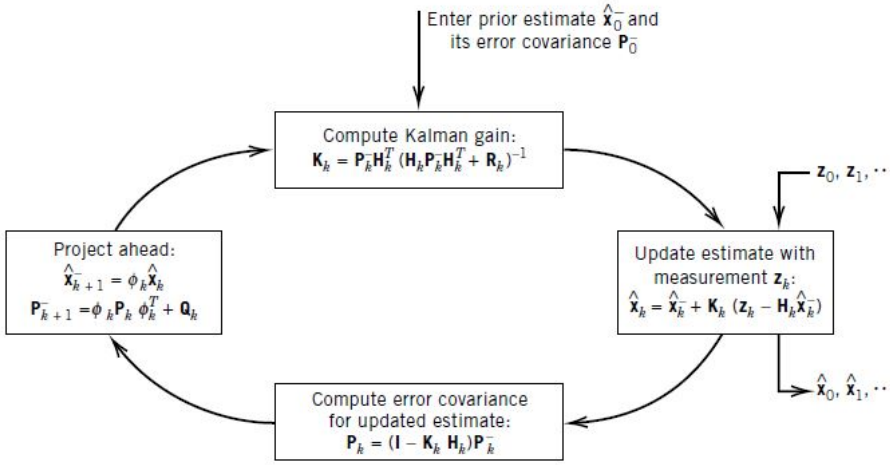

Figure D.1: Kalman filter loop. Image courtesy of Brown and Hwang (2012)

Appendix E

Merlin data

ROV Specifications:

Depth rating	3000 msw
Length	2.8 m
Width	1.8 m
Height	1.7 m
Weight	2800 kg
Manipulator	Schilling Titan 4 (or client spec.)
Manipulator	Schilling Rig master (or client spec.)
Thrusters	8 of Electrical 12" Dual Counter Rotating Propellers
Configuration	4 of Horizontal (vectored), 4 off Vertical
Pulling force	8 kN Forward / Aft. / Lateral 11 kN Vertical
Auxiliary Tool HPU	1 of 18-30 kW Electrical Hydraulic Power Pack 49-80 l/min adjustable up to 315 bar
Auxiliary ROV HPU	1 of 8-18 kW Electrical Hydraulic Power Pack 20-49 l/min adjustable up to 250 bar
Valve pack 1	8 of proportional NG 3 valves
Valve pack Tool	8 of proportional NG 3 valves & 1 off Ng 10
Subsea Electrical interface	Communication: RS 232, RS 422, RS 485, Ethernet, fiber (HD) Power: 24V, 110V, 3000V
Cameras	1 of Low Light Camera (pan & tilt) 1 of Color & Zoom Camera (pan & tilt) 2 fixed color cameras (on front bar). 2 of color camera (one rear, one center for TMS docking) Total number of camera slots: 8 (prepared for add. pan & tilt)
Lights	4 of Q-LED, 3 of MV-LED
Sensors:	
Depth	Digiquartz & altimeter
Heading	Gyro - as specified by client
Pitch & Roll	+/- 20 degrees
Sonar	MS-1000
Auto functions	Auto Heading / Auto Depth / Auto Altitude
Tooling	Wire cutter, ROV hook/shackle, rope cutter, grinder - optional tools according to client request
Power Requierments:	
ROV	250 kVA
Control - Container	30 kW, 440V/50-60Hz

This is standard equipment for the Merlin WR200. Different options for lighting, cameras, manipulator arms, tools etc. may be selected.

Merlin WR200 - complete (new)

Physical Properties for IKM-1013251_Ver2
General Properties:

	Material:	{}	
	Density:	1,039 g/cm^3	
	***Mass:**	3019,249 kg (Relative Error = 0,000245%)	
	Area:	186542278,399 mm^2 (Relative Error = 0,005466%)	
	Volume:	2,90582908672 6E+009 mm^3 (Relative Error = 0,000245%)	
****Center of Gravity:**			
	X:	-2,341 mm (Relative Error = 0,000245%)	
	Y:	3,014 mm (Relative Error = 0,000245%)	
	Z:	-21,193 mm (Relative Error = 0,000245%)	
****Mass Moments of Inertia with respect to Center of Gravity(Calculated using negative integral)**			
	Ixx	1819601608,273 kg mm^2 (Relative Error = 0,000245%)	
	Iyx Iyy	-2696884,126 kg mm^2 (Relative Error = 0,000245%)	3,064990196615E+009 kg mm^2 (Relative Error = 0,000245%)
	Izx Izy Izz	120369718,084 kg mm^2 (Relative Error = 0,000245%)	-7207982,764 kg mm^2 (Relative Error = 0,000245%) 2,887168166629E+009 kg mm^2 (Relative Error = 0,000245%)
****Mass Moments of Inertia with respect to Global(Calculated using negative integral)**			
	Ixx	1820985065,487 kg mm^2 (Relative Error = 0,000245%)	
	Iyx Iyy	-2675581,594 kg mm^2 (Relative Error = 0,000245%)	3,066362768103E+009 kg mm^2 (Relative Error = 0,000245%)
	Izx Izy Izz	120219937,803 kg mm^2 (Relative Error = 0,000245%)	-7015121,476 kg mm^2 (Relative Error = 0,000245%) 2,887212140375E+009 kg mm^2 (Relative Error = 0,000245%)
****Principal Moments of Inertia with respect to Center of Gravity**			
	I1:	180619521 3,215 kg mm^2 (Relative Error = 0,000245%)	
	I2:	3,065330983149E+009 kg mm^2 (Relative Error = 0,000245%)	
	I3:	2,900233775152E+009 kg mm^2 (Relative Error = 0,000245%)	
****Rotation from Global to Principal**			
	Rx:	2,61 deg (Relative Error = 0,000245%)	
	Ry:	-6,34 deg (Relative Error = 0,000245%)	
	Rz:	-0,37 deg (Relative Error = 0,000245%)	

*Calculations are based on user overwritten values
**Values do not reflect user-overridden mass or volume

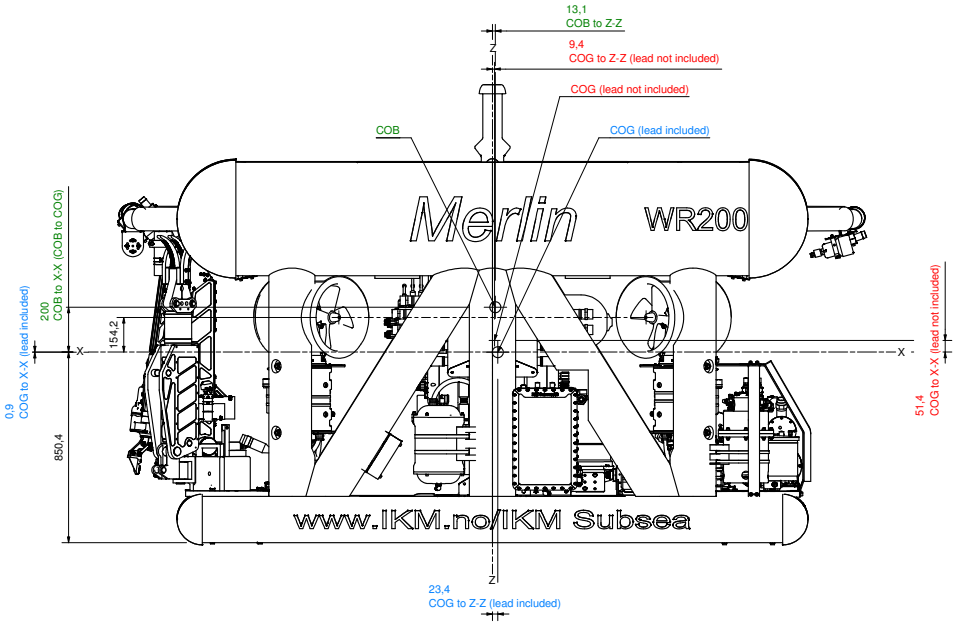

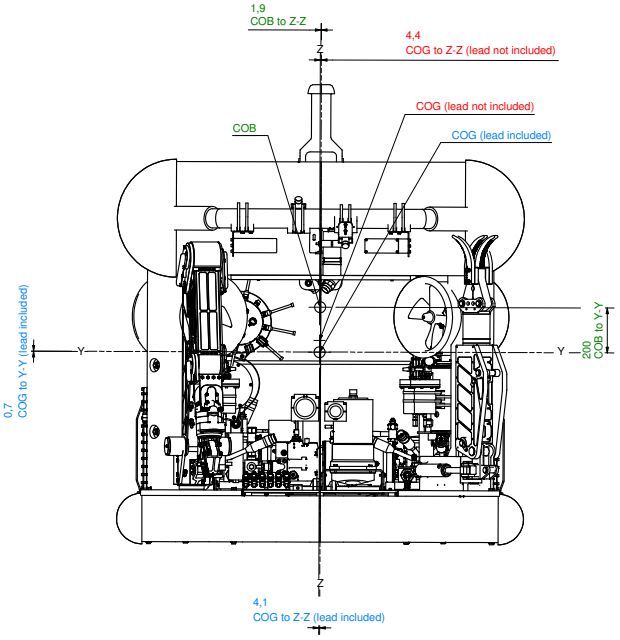

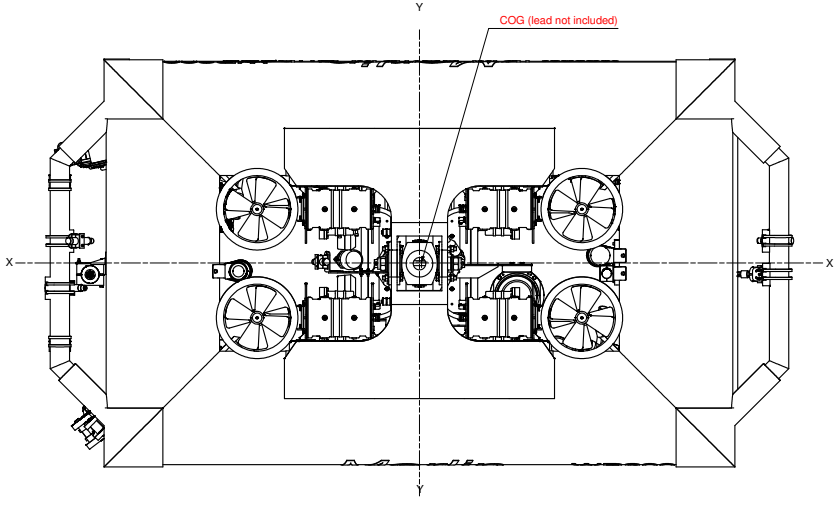

Total mass (without lead) = 2911 Kg

Total volume = 2,99 m^3

Payload = 157 Kg (cables and wires not taken into consideration)

IKM Subsea AS

www.ikm.no

ISO-SERTIFISERT: ISO 9001/2008

ACHILLES ID: 28919

TOTAL MASS: 2911,4294 kg

PROJECT: GA

TOLERANCE IF NOT SPECIFIED: NS ISO 2768-1 Medium.

PROJ. TYPE E

TITLE: ROV - COG & COB
MERLIN WR200 - PLAIN
ASSEMBLY

SIZE	SCALE	PROJECT No.	DOC. No.	REV.	SHEET. No.
A3		STD	IKM-1016093	Z1	2 OF 2